NTNU
Norwegian University of
Science and Technology

Path Following Control for Underwater Swimming Manipulators Moving in 3D

Using Geometric Attitude Control

Marianna Wrzos-Kaminska

Master of Science in Cybernetics and Robotics
Submission date: July 2018
Supervisor: Kristin Ytterstad Pettersen, ITK

Norwegian University of Science and Technology
Department of Engineering Cybernetics

Problem description

An Underwater Swimming Manipulator (USM) is an underwater snake robot (USR) equipped with thrusters. The main purpose of the thrusters are to provide forward thrust without requiring the snake robot to follow an undulating gait pattern, which is of particular importance in narrow, confined environments, and to provide sideways thrust for stationkeeping and trajectory tracking. The stationkeeping and trajectory tracking capabilities enable the USM to act like an underwater floating base manipulator. The slender, multi-articulated body provides the USM with outstanding accessibility and flexibility. As such, the USM is a crossover between a small autonomous underwater vehicle (AUV) and an underwater snake robot.

The task of this assignment is to develop a path following controller for USMs moving in 3D.

1. Develop a method for attitude control suitable for USMs moving in 3D.
2. Using that and the control approach presented for direction control of USMs in [1], i.e. using the joints for direction control, develop a path-following controller for motion in 3D.
3. Implement the controller in MATLAB/Simulink.
4. Through simulations, examine the performance of the controller when used with different body shapes and additional thrusters.

[1] A. Sans-Muntadas, E. Kelasidi, K. Y. Pettersen and E. Brekke, "Spiral path planning for docking of underactuated vehicles with limited FOV," in *Proc. 1st IEEE Conference on Control Technology and Applications*, Kohala Coast, Hawaii, 2017.

Supervisor: Kristin Y. Pettersen

Abstract

The underwater swimming manipulator (USM) is a snake robot equipped with thrusters for faster propulsion or hovering. The entire articulated body of the USM can be used as a floating manipulator arm, and its slender build allows it to access confined spaces in order to perform inspection and maintenance of underwater structures. In order to extend operation time and energy-efficient methods of transport between sites are needed.

In the work presented in this thesis, a path-following method for USMs moving in 3D using the joints of the USM for direction control by means of curving its body is developed. This aims to conserve energy by reducing the use of thrusters.

A control law for tracking a time-varying pointing direction using only two control inputs is developed as a first step. The control law is proven to give asymptotic tracking of the reference, and has no fixed singularities.

Based on this control law, a method for pointing the head of the USM in the desired direction of travel by using its joints is proposed. The method is combined with a guidance law to create a path-following controller for following straight paths.

Different body curves and the use of thrusters to aid the direction control have been investigated through simulations. The simulations show that the USM does not manage to follow the path when the joints are used as the sole means of controlling its direction. It does however remain sufficiently close to the path to make this a plausible method of travel in open areas. Shapes which keep the front portion of the USM straight while primarily using the back for direction control like the tail of a fish, generally stayed closer to the path.

Simulations also demonstrated that exploiting the presence of multiple longitudinal thrusters to stabilise the pointing direction of the USM removed the oscillations in the horizontal plane, without engaging more thrusters than already used for forward propulsion.

Sammendrag

Svømmende undervannsmanipulatorer (USMer) er slangeroboter utstyrt med thrustere for raskere fremdrift, eller for å kunne holde seg i ro. Med sine mange ledd kan hele kroppen til en USM brukes som en flytende manipulatorarm. Den slanke formen gjør også at den lett kommer seg til på trange steder, slik at den kan brukes til inspeksjon og vedlikehold av konstruksjoner under vann. For å forlenge driftstid og øke rekkevidden trengs det energieffektive transportmetoder.

Arbeidet presentert i denne avhandlingen har vært å utvikle en banefølgingsmetode for USMer i 3D, der kun leddene brukes til å styre retning ved å krumme kroppen til USMen. Formålet er å redusere energibruk ved å la være å bruke thrustere til å styre retningen.

Som et første steg er det utviklet en kontrollov for å styre pekeretningen til et system med kun to pådrag. Det bevises at kontrolloven gir asymptotisk følging av en tidsvarierende referanse, og kontrolloven har ingen fast plasserte singulariteter.

Basert på denne kontrolloven er det foreslått en metode for å peke hodet til USMen i den ønskede bevegelskesretningen. Dette kombineres med en guidancelovfor å styre USMen inn mot og langs en rett bane.

Gjennom simuleringer har bruken av ulik krumning av kroppen for styring av retning, samt bruk av thrustere for å ytterligere hjelpe styringen av retning blitt undersøkt. Simuleringene viser at USMen ikke er i stand til å følge banen nøyaktig når kun leddene brukes for å styre retning, men forblir tilstrekkelig nærme til at metoden er brukbar for transport over åpne områder. Kroppsfasonger der fremre del holdes rettere mens bakparten brukes til retningsstyring tilsvarende en hale, holdt seg hovedsakelig nærmere banen.

Simuleringene viste også at svigningene i det horisontale planet kunne elimineres ved å utnytte at USMen har flere langsgående thrustere. Ved å variere pådraget på disse kan pekeretningen stabiliseres uten å ta i bruk flere thrustere.

Preface

The work presented in this thesis has been carried out at the Department of Engineering Cybernetics at The Norwegian University of Science and Technology (NTNU), under the supervision of Professor Kristin Ytterstad Pettersen.

The contributions of this work are listed in Section 1.4.

I have independently developed and implemented all the control methods presented in this thesis.

The snake robot simulator used in this work was developed by PhD candidate Henrik Schmidt-Didlaukies. It has been adapted to Simulink by PhD candidate Ida-Louise G. Borlaug, who also combined the dynamics developed by Schmidt-Didlaukies with existing code for thruster allocation, developed by PhD candidate Jørgen Sverdrup-Thygeson.

Schmidt-Didlaukies and Sverdrup-Thygeson have also been of help by answering questions regarding their work on modelling and control of USMs which this thesis builds upon.

An overview of the implementation of the path-following method developed in this work is shown in Appendix D, Figure D.1. The "Snake model" and "Thruster allocation" blocks, containing the dynamics of the robot and the thrust allocation algorithm respectively, were received from PhD candidate Borlaug. The thrust allocation block has been adapted in this work to include two modes using only longitudinal thrusters. The rest of the guidance and control has been implemented entirely during this work.

Much of my time was spent on tuning control parameters, trying to achieve some decent behaviour of the model. I discovered only a week before the submission of this thesis that there was a mistake in the USM model parameters I had received. This caused the USM to be subject to the rigid body inertia and hydrostatic restoring forces of a robot with ten times the mass. The performance of the path-following method when varying the parameters of the guidance law has therefore not been investigated, due to lack of time, and neither has its performance on non-horizontal paths. I was however able to rerun the simulations of the path-following method with different body curves, as well as all the combinations of thruster use I have proposed in this thesis, with the correct model parameters.

Some simulation results of path-following with the incorrect model parameters are also shown in Appendix E.

Acknowledgements

I would like to thank my supervisor Professor Kristin Y. Pettersen for her guidance, enthusiasm, and valuable insights.

I would also like to thank Henrik Schmidt-Didlaukies for taking the time to answer my questions, and Jørgen Sverdrup-Thygeson for sharing some of his experiences working on the topic of USMs.

Thanks go out to my family for all their support and enthusiasm. To my parents, thank you for all your patience and advice. Most of all, thank you for raising us in a home where mathematics are cool.

Marianna Wrzos-Kaminska
Trondheim, July 5, 2018

Contents

List of Tables

List of Figures

List of Abbreviations

AUV	Autonomous Underwater Vehicle
CB	Center of Buoyancy
CM	Center of Mass
DOF	Degree Of Freedom
I-AUV	Intervention Autonomous Underwater Vehicle
ILOS	Integral Line-Of-Sight
LOS	Line Of Sight
ROV	Remotely Operated Vehicle
TCM	Thrust Configuration Matrix
USM	Underwater Swimming Manipulator
USR	Underwater Snake Robot

Chapter 1

Introduction

1.1 Motivation

The exploration and exploitation of our oceans is ever increasing in many fields, and with it the amount of tasks to be performed underwater. Such tasks include seafloor mapping, environmental monitoring, construction, inspection of underwater structures and pipelines, or maintenance thereof, within fields ranging from scientific to military or industrial applications, in particular the oil and gas industry [48].

Surveying, mapping and monitoring are to an increasing degree performed by autonomous underwater vehicles (AUVs), which reduce the need and consequently cost of human involvement. In contrast, tasks requiring intervention or interaction with the environment, such as retrieving objects, turning valves or performing repairs or other maintenance, are largely performed using remotely operated vehicles (ROVs), tethered to a surface vessel from which they are operated. ROVs require not only a human operator, but also a large mother vessel boasting both a crane to gently deploy the ROV, and the ability to keep its position steady during operation, so as to not snap or stretch the tether. For these reasons, ROVs are expensive in use, and there is an ongoing effort to develop of vehicles capable of performing intervention autonomously, intervention AUVs (I-AUVs) [38].

Many concepts and prototypes of I-AUVs developed so far share the build of their remotely operated counterparts, consisting of a larger, stable body or base, and an attached manipulator arm. An alternative to this is the underwater swimming manipulator (USM), which is a crossing between a traditional thruster-driven AUV and an underwater snake robot (USR) [43]. It possesses the slender, articulated body of the USR, but is in addition equipped with thrusters. The USMs relatively small size and articulated body gives it better access to narrow spaces than vehicles with a large floating base would have. The thrusters provide it with the ability to hover, as well as being a faster method of forward propulsion than the undulatory swimming gaits employed by USRs, mimicking the motions of their biological counterparts. The USM can therefore both serve as a floating-base manipulator arm and travel similarly to a typical slender-bodied survey AUV. These two modes of use or operation have been referred to as work mode and transport mode, respectively [42].

For tasks which require travelling a significant distance, such as pipeline inspections, seafloor mapping, or tasks at distant sites, energy-efficient long-range travel is crucial. Minimising energy consumption allows for longer operation between docking or retrieving the robot, which in turns extends its reach. A longer reach is especially valuable if the USM is operated from a stationary docking point.

So far, most work on the transport mode of the USM use tunnel thrusters to control or help stabilise its attitude or direction of travel [4, 43, 45]. However, drawing inspiration from biological and robotic swimmers from which the USM has inherited its slender, articulated body, its direction of travel can also be controlled simply by curving the body, replacing only the method of forward propulsion with thrusters. This approach has been used to demonstrate docking using a USM in [39], where the USM followed a planar, spiral path using only its joints to turn, and tail thrusters to propel itself forward.

In this thesis, a path-following method for USMs moving in 3D is developed, inspired by the method used in [39], i.e using the joints as the main means of direction control. To the author's best knowledge, path-following in 3D has not been considered for USMs before. Performance with and without additional thrusters to stabilise its attitude, and performance of different body curvatures are investigated through simulations.

As USM bodies are designed for the double purpose of being both an arm and a vehicle, they can be more agile than typical AUVs, but will not necessarily be as steady when travelling like a vehicle. Thus especially in 3D, manoeuvring methods developed for AUVs may not be suitable for USMs. An attitude control law better suited to accommodate the possibility of an increased range of motion is therefore developed as a first step.

1.2 Problem description

The aim of the work presented in this thesis is to develop a path-following method suitable for the control of USMs moving in 3D, and investigate its performance when using different combinations of body shapes and use of available thrusters.

As in [39], the direction of the USM is controlled by curving its body, similarly to how biological swimmers curve their bodies to change the direction they swim in. That way, the entire length of the body can be viewed as an alternative to the control surfaces, such as rudders, of typical marine vehicles. The USMs considered in this thesis have joints iwth two degrees of freedom. Curving the body using these joints allows for control of the direction in which the head of the USM is pointing, but not its rotation about this pointing direction. This is similar to the case of many AUVs, equipped with control surfaces for changing their pitch and yaw only, while the roll remains unactuated.

However, such AUVs are also typically passively stabilised in roll, either by ballast or fins. Path-following methods in 3D developed for such vehicles can therefore disregard the roll of the vehicle entirely, which simplifies the control problem, as was done in e.g. [9, 10]. Other methods do not disregard roll, but make use of the knowledge that it is passively stabilised to formulate a reference for the full attitude where the vehicle always has zero roll [47].

While each individual link of a USM can be passively stabilised, the USM as a whole is not necessarily stabilised in roll when its body is bent into the many possible configurations. In addition, heavy stabilisation of the links would undermine its abilities and dexterity as a manipulator. To be suitable for USMs, path-following methods in 3D should therefore take into account the possibility of non-zero roll while controlling the pointing direction towards the path.

In order to accommodate the increased range of motion that may be possible for a USM compared to a stabilised AUV, and provide attitude control which works regardless of the roll angle without disregarding it, in this thesis the pointing direction will be controlled using its unit vector representation directly. Unlike the commonly used Euler angles, this representation has no singularities, while still having an intuitive geometrical interpretation. For typical stabilised AUVs, as well as other systems such as many types of aircraft, these singularities can be placed at points which will not or should not be reached by the system. When controlling a USM, there may not necessarily be any such point. It is for example not unreasonable to desire a USM to move vertically, either to quickly change depth, or to inspect the outside of a wall or column of an underwater structure.

1.3 Literature review

1.3.1 Path-following control for marine vehicles

Marine vehicles, both surface and underwater vehicles, are often underactuated, possessing only a propeller to give forward thrust and one or more rudders to control their attitude. Path-following is therefore achieved by pointing the vehicle towards the path. A commonly used method of guidance is the line-of-sight (LOS) method, where the vehicle is pointed towards a point a certain distance ahead of the vehicle along the path, in order to approach the path smoothly [13]. Although initially developed for straight paths, is has also been used to achieve path-following of curved paths, by formulating the guidance law in a reference frame moving along the path [5,9]. The vehicle follows the path by chasing a virtual target, being the origin of this moving frame. In order to still give a smooth aprpoach to the path, the vehicle is aimed at a point ahead of the origin, along the direction tangential to the path.

LOS guidance has also been extended to work in the presence of ocean currents pushing the vehicle off its path. In order to stay on the path, the vehicle must follow the path not pointing along it, but at an angle, called the sideslip angle in the case of surface craft. For the task of following straight paths in the presence of constant ocean currents, the heading of the vehicle required to follow the path can be found by using an integral line-of-sight (ILOS) guidance law, which has been done for both surface vessels [8] and underwater vehicles moving in 3D [10]. In the case of curved paths, the disturbance from a constant ocean current has instead been compensated for by using an observer to estimate the magnitude and direction of the current and direct the vehicle accordingly [32,34].

The aforementioned works [9,10,32] on 3D motion consider AUVs with passively stabilised roll, reducing the dynamics to 5 degrees of freedom (DOF), and causing the pitch and yaw angles given by the guidance laws to coincide with the rotation caused by the vehicle actuators, which simplifies the control problem. In addition, the control laws are formulated using the Euler angle representation, which is subject to singularities. The desired orientation as given by applying LOS guidance in 3D has been translated to a quaternion representation in [29].

The principle of guiding the vehicle towards a point ahead along the path is also used in [47] for solving the task of following a straight path, but formulated as a vector sum. The travelling direction of a slender-body AUV is then stabilised about the resulting reference using an artificial potential energy function. Rather than disregarding roll entirely, its passive stabilisation is taken into account, and a reference for the full attitude is specified as a rotation matrix. In order for it to be unambiguously defined, the desired direction of travel cannot be parallel to the direction of gravity.

A similar vector guidance law is used in [33], where a surface vessel is made to follow a straight path in the presence of a constant ocean current, at a fixed speed over ground. An observer is used to estimate the ocean current magnitude and direction, which is then used to define a complete reference direction rather than a sideslip angle and heading separately. The attitude is controlled using the rotation matrix representation of attitude. This method is intended to be a first step towards a singularity-free control method for underactuated marine vehicles moving in 3D.

1.3.2 Control of USRs and USMs

Much of the work done on the topic of control of USMs has focused on their capabilities as floating-base manipulators [1, 42, 44, 46]. In [1], methods originating from the field of space-engineering are applied to compensate for reaction forces disturbing the position of the base due to movement of the rest of the body. These reaction forces are a much more significant influence on a manipulator whose base is relatively small. In the case of a USM, it is of a similar size as each of the links of the manipulator arm.

Among the existing approaches to the transport mode of a USM, to be used for travelling from point to point, most use tunnel thrusters for control of direction. In [43], a LOS guidance law is used to guide the USM towards a straight path in a horizontal plane. Two cases are considered; one where the body of the USM is kept straight, and one where all joints are bent proportionally to the desired heading angle. The latetr results in curving the body towards the path. Simulations show that the second method, where the USM was curved to point towards the path, gives faster convergence towards the path and reduces the thruster effort required to turn the USM towards it. The idea of curving the body for direction control is inspired by control strategies for USRs, however, the tunnel thrusters are still used for additionally stabilising the attitude. The curved configuration is revisited in [45], where comparisons are made between the cases of controlling the surge velocity of the base, or tail, versus controlling the surge velocity of the end-effector, or head. The results presented suggest that controlling the surge velocity of the base leads to less pendulum-like motion of the back end of the USM.

Controlling the direction of travel using thrusters was also done in [4], where sliding mode control was used among other to solve the task of having the USM's center of mass (CM) follow a given trajectory, while its head moves as if to perform an inspection.

In contrast to these works, path-following using only the articulated body of a USM for direction control, and thrusters only for forward propulsion was achieved experimentally in [39], for the purpose of docking at a docking station. Instead of curving the body using equal joint angles for all joints as in [43, 45], the joint angle is scaled with the same scaling function used to generate an eel-like gait for USRs in among other [15]. This results in a shape that curves more towards the tail of the robot.

While a USM possesses the ability to propel itself forward using both thrusters or undulatory motion, or even a combination of the two, using thrusters only was found to be the most efficient method in an experimental study performed in [18]. The results also showed that combining thrusters with body undulations reduced the speed achieved while using the same forward thrust.

The method of controlling the direction of the USM by curving its body is inspired by work done on USRs, which in turn is inspired by the motion of boilogical swimmers. USRs can be made to move forward by propagating a wave along their body, and turning is achieved by adding an offset to the oscillating joint references. This way, the wave formed by the body oscillates about a curve rather than a straight line from head to tail. In [15], a LOS guidance law is used to determine this offset, in order to make the robot turn towards and onto a straight path. Path-following is demonstrated using two different swimming patterns, one similar to that of biological eels, and one like the motion of biological snakes. The strategy is extended to handle the presence of an ocean current using integral action in the guidance law in [16].

A similar strategy for direction control was used in [14] for waypoint tracking using a fish-like AUV. Unlike a USR, which has joints along the entire length of its body, this fish-like AUV has only two joints, allowing it to move only a tail segment and a fin at its end, attached to a larger body.

A strategy for path following of general paths parametrised as curves was proposed for a swimming eel-like robot in [24], using the method of propagating a moving frame along the path.

Path-following of curved paths has also been achieved for USRs in the presence of ocean currents in [22]. An observer is used to estimate the magnitude and direction of the current, so that it can be taken into account in a guidance law formulated as a vector sum, similar to that in [33]. Unlike the strategy used for the eel-like robot in [24], a different mathematical description of the curve is chosen, and the resulting guidance law does not rely on propagating a frame along the path.

Notably, all of the aforementioned works on underwater travel using robots with articulated bodies consider only the case of moving in a horizontal plane.

A model for the full 3D motion of an eel-like robot was developed in [21], and among the simulation results shown was swimming along a circular path in a vertical plane. The model considers a robot not subject to any hydrostatic forces at all. In [17], a USR swimming in a vertical plane is modelled and simulated. This model takes into account the possibility of non-neutral buoyancy, which results in the robot sinking or drifting upwards.

1.3.3 Geometric attitude control

In order to avoid the problems of singularities when using the Euler angle representation of attitude, or unwinding due to the quaternion representation, attitude control can be performed directly on the rotation matrix representation of attitude, which is both valid globally and unique [11]. However, no continuous feedback law is able to globally stabilise an attitude setpoint [3]. This is due to the fact that the direction towards the desired attitude setpoint along the shortest path is not continuous at points differing by a rotation of 180°. Continuous geometric control laws will therefore lead to these points being unstable equilibrium points to which the system can converge from a small number of states, but from which it is easily dislodged by disturbances [11]. The stable manifolds of such equilibria are analysed in [27] for the case of pendulums, both spherical whose attitude evolve on the unit sphere $\mathbb{S}^2$, and 3D pendulums whose attitude evolve on the space $SO(3)$.

Attitude control using the full rotation matrix representation has been applied to among other quadrotor unmanned aerial vehicles [26, 28, 31], where tracking a reference attitude is used to control the direction of thrust and in turn track a position trajectory. This includes difficult manoeuvres such as recovering from being almost upside-down [26].

It has also been applied to AUVs in [40], where geometric attitude control is used for tracking both a desired attitude and position, using a fully actuated, spherical AUV.

In [25], a new error function on the space of rotation matrices is developed. Unlike previous error functions, this one does not result in diminishing control effort when the angle between the current attitude and the reference attitude is large.

For some applications, it is not necessary to control the full attitude, but merely a pointing direction, or reduced attitude. The reduced attitude can be the body-frame representation of a fixed direction in the world frame [11], or the world-frame representation of a fixed direction in the body frame, such as a principal axis [6].

Stabilisation of reduced attitude was considered in [11], using three control torques. In [36, 37], tracking control laws for reduced attitude are developed for spacecraft which are fully actuated in attitude. The third control input is utilised to perform additional tasks, such as rotating about the reduced attitude, in order to evenly distribute heat from the sun.

In [30], a stabilising law for the full attitude is formulated such that the direction of the reduced attitude is prioritised. The reduced attitude is controlled to its desired setpoint along the shortest path on the sphere, while the full attitude is stabilised about it.

The reduced attitude evolves on the sphere $\mathbb{S}^2$, which is a two-dimensional space, and consequently only two control torques are really necessary to control it. In [6], both stabilisation and tracking laws for reduced attitude using only two control inputs are developed. While the stabilisation control problem is solved on the practical example of spacecraft dynamics, the tracking law is formulated only in a coordinate-free fashion, for a very simple system on the surface of $\mathbb{S}^2$.

1.4 Contributions

The two main contributions of the work presented in this thesis are as follows:

- The development of a control law for tracking of a pointing direction for systems with three rotational degrees of freedom, but only two control torques. A condition on the inertia of the system is found under which the system is proved to give asymptotic tracking of a time-varying reference. The control law has no fixed singularities, and rotates the system in the direction of the shortest distance along the surface of the unit sphere.The control law is based on existing methods for control of pointing direction of systems which are fully actuated in attitude, or which evolve on the surface of the two-dimensional unit sphere.

- The development of a path-following controller for USMs moving in 3D. A control method for pointing the direction of the USM in 3D using its joints is proposed based on the attitude control law described above. This method is combined with a guidance law to solve the task of following straight paths. To the author's best knowledge, there are no existing methods of path-following control for USMs moving in 3D space, only for planar motion.

The path-following control method for USMs has been implemented in MATLAB/Simulink. The performance of the path-following method has been evaluated through simulations of numerous cases:

- The performance of different body curvatures for turning have been compared.
- The influence of joint torque limits and compensation for hydrostatic forces acting on the joints is examined. The previous work [1] on the topic of hydrostatic forces acting on a USM used a simulation model which did not include joint dynamics.
- The performance of the path-following method using all available thrusters is compared to the case of reducing the use of thrusters by using only longitudinal thrusters. Two methods of control using longitudinal thrusters are examined: one considering only forward propulsion, and one exploiting the possibility of having multiple longitudinal thrusters to aid the turning motion.

In order to compare the performance of using thrust allocation to generate forces and moments with respect to either the base or the end-effector, the mass matrix and thrust configuration matrix with respect to the end-effector (at the opposite end of the kinematic chain which constitutes the robot) is derived.

1.5 Outline

The rest of this thesis is organised as follows: Chapter 2 presents relevant background on the topics of attitude control, path-following for marine vehicles and control of swimming snake robots. In Chapter 3, the control law for the pointing direction of systems with two torques is presented. The proof of its stability is given in Appendix B.

Chapter 4 presents a model of the USM dynamics and kinematics. In Chapter 5, the proposed path-following method for USMs is presented, including guidance, control of pointing direction using the joints of the USM, and use of thrusters. Simulations of this method are presented in Chapter 6, and the results are discussed in Chapter 7. Finally, Chapter 8 gives the conclusion and suggestions for further work.

Relevant mathematical definitions and theorems are listed in Appendix A. Simulation model parameters and an overview of the implementation of the complete path-following method from Chapter 5 are shown in Appendix C and Appendix D, respectively. Appendix E contains simulation results using a USM model subject to disproportionately large hydrostatic forces.

Chapter 2

Background Theory

In this chapter, background material on three topics relevant to this thesis will be presented. The first section introduces two existing geometric control methods for tracking a reduced attitude. These are the methods upon which the one developed in this work, presented in Chapter 3, is based.

Next, guidance methods for the purpose of achieving the task of path-following for marine vehicles are introduced.

The last section of this chapter covers modelling of the swimming gaits used by USRs and biological swimmers. The motion of such swimmers serves as inspiration for the approach to controlling the pointing direction of USMs used in this thesis, and as inspiration for body shapes to consider.

2.1 Geometric attitude control

2.1.1 Reduced attitude tracking using three control torques

The full control law developed in [36] makes it possible not only to track a time-varying reduced attitude, but also to align the reduced attitude of a spacecraft with the surface of a cone around this time-varying reference, move along the conical surface, and rotate the spacecraft about the reduced attitude. Here, the simplest form of the tracking law developed in [36] is presented here, which is the form required to track a time-varying reduced attitude.

The control law is resolved in the body-fixed frame of the spacecraft, so that the body-frame representation of the reduced attitude $\mathbf{a}$ of the spacecraft is constant, i.e. $\dot{\mathbf{a}} = 0$. The objective is to track a reference attitude with body-frame representation $\mathbf{b}$. The vectors $\mathbf{a}$ and $\mathbf{b}$ are both unit vectors, and their cross-product can be expressed as

$$\mathbf{b} \times \mathbf{a} = \sin\theta\mathbf{n} \tag{2.1}$$

where $\theta \in [0, \pi]$ is the angle between $\mathbf{a}$ and $\mathbf{b}$, and $\mathbf{n}$ is the vector perpendicular to both $\mathbf{a}$ and $\mathbf{b}$.

The reference $\mathbf{b}$ changes according to

$$\dot{\mathbf{b}} = -\boldsymbol{\omega} \times \mathbf{b} + \mathbf{R}\dot{\mathbf{b}}_I \tag{2.2}$$

where $\boldsymbol{\omega}$ is the angular velocity of the spacecraft relative to an inertial frame, $\mathbf{R}$ is the rotation matrix which transforms a vector given in the inertial frame to its body-frame representation, and $\mathbf{b}_I$ is the inertial-frame representation of the reference.

The spacecraft considered has the following dynamics:

$$\dot{\boldsymbol{\omega}} = \mathbf{J}^{-1}\left(-\boldsymbol{\omega} \times (\mathbf{J}\boldsymbol{\omega} + \mathbf{h}) + \boldsymbol{\tau}\right) \tag{2.3}$$

with $\mathbf{J} = \mathbf{J}^\top > 0$ being the inertia matrix of the spacecraft, $\boldsymbol{\tau}$ being the control torque, and $\mathbf{h}$ any additional angular momentum to which the system is subject.

The control law which tracks the reference $\mathbf{b}$ is then given as

$$\boldsymbol{\tau} = \boldsymbol{\omega} \times (\mathbf{J}\boldsymbol{\omega} + \mathbf{h}) + \mathbf{J}\dot{\boldsymbol{\omega}}_r - \mathbf{P}\mathbf{n}\sin\theta + \mathbf{D}\boldsymbol{\omega}_e \tag{2.4}$$

The matrices $\mathbf{P}$, $\mathbf{D}$ are gain matrices chosen such that $\mathbf{P}^{-1}\mathbf{J}$ and $\mathbf{P}^{-1}\mathbf{D}$ are positive definite matrices. The term $\boldsymbol{\omega}_r$ is a reference angular velocity, and $\boldsymbol{\omega}_e = \boldsymbol{\omega}_r - \boldsymbol{\omega}$ is the velocity tracking error. The reference velocity for the case of just tracking the reference $\mathbf{b}$ is given as

$$\boldsymbol{\omega}_r = \mathbf{R}\mathbf{b}_I \times \dot{\mathbf{b}}_I = \mathbf{b} \times \mathbf{R}\dot{\mathbf{b}}_I \tag{2.5}$$

which is the angular velocity of $\mathbf{b}_I$, transformed into the body frame.

The first two terms of the control law (2.4) ensure cancellation of system dynamics and feedforward from the reference, respectively. The next two are a proportional and a derivative term. The expression $\sin\theta\mathbf{n}$ in the proportional term is equivalent to the more easily available expression $\mathbf{b} \times \mathbf{a}$. However, the expression $\mathbf{n}\sin\theta$ highlights the fact that the control effort will start to diminish when the angle between $\mathbf{a}$ and $\mathbf{b}$ grows larger than $\frac{\pi}{2}$.

The control law (2.4) gives two equilibria: the desired case when $\theta = 0$ and $\boldsymbol{\omega}_e = \mathbf{0}$, and the state $\theta = \pi$, $\boldsymbol{\omega}_e = \mathbf{0}$. The latter is an unstable equilibrium, and the desired equilibrium $\theta = 0$, $\boldsymbol{\omega}_e = \mathbf{0}$ is stated to be almost-globally asymptotically stable.

2.1.2 Two-dimensional reduced attitude tracking on $\mathbb{S}^2$

As reduced attitude is an element on the two-dimensional unit sphere $\mathbb{S}^2$, it is possible to control it using only two control torques. This is done in [6], for systems defined on the sphere $\mathbb{S}^2$. Details of the paper [6], including proofs, can be found in the technical report [7]. Throughout this thesis, the technical report [7] will only be cited for content exclusive to the report. Otherwise, the paper [6] will be cited.

A point $p \in \mathbb{S}^2 \subset \mathbb{R}^3$ has a corresponding tangent space denoted $T_p\mathbb{S}^2$, being the space of all vectors in $\mathbb{R}^3$ perpendicular to p. The velocity of a point on the sphere lies in its tangent plane.

The distance between two points p and q on the sphere is taken to be

$$d(p, q) = \arccos\left(p^\top q\right) \tag{2.6}$$

This is in fact the angle between the vectors from the origin to the points p and q, and the shortest distance between the two points along the surface of the unit sphere. The vector Y_p^q in the tangent space of p and pointing in the direction of the shortest distance to q is called the geodesic versor, and defined as

$$Y_p^q = \left(\frac{p \times q}{\|p \times q\|}\right) \times p \tag{2.7}$$

If p and q are parallel, that is either equal or exactly opposite, the versor (2.7) is not defined. In the case where the points are opposite each other, it is because the distance between the two points along any direction is equal.

A tracking law is developed for the system

$$\begin{aligned} \dot{p} &= X_p^1 v_1 + X_p^2 v_2 \\ \dot{v} &= u \end{aligned} \tag{2.8}$$

where X_p^1, X_p^2 for a basis for $T_p\mathbb{S}^2$, so that v_1, v_2 are the elements of v when decomposed with respect to X_p^1, X_p^2. Rather than an angular velocity about an axis, v is the velocity along the surface of the sphere, and the input u is the acceleration along the surface of the sphere.

The velocities of p and the time-varying reference q lie in different tangent planes, at different points on the sphere. In order to be compared, the elements of the tangent space $T_q\mathbb{S}^2$ of q must be rotated into the tangent space of p. This is accomplished using the matrix $\mathcal{R}$ defined in [6] as the matrix which rotates q into p such that

$$\mathcal{R}q = p, \quad \mathcal{R}(p \times q) = p \times q \tag{2.9}$$

In addition to making it possible to compare the velocities of p and q, rotation by $\mathcal{R}$ also rotates the acceleration of the reference into the tangent space $T_p\mathbb{S}^2$, which is the space in which the input u acts. The rotated version of $\ddot{q}$ can therefore be fully realised by the input u.

Using this, a tracking law for the system (2.8) is formulated as

$$u = \mathcal{R}\ddot{q} + k_p d(p,q) Y_p^q - K_d(\dot{p} - \mathcal{R}\dot{q}) + \omega_p(\dot{p} \times p) \tag{2.10}$$

where k_p is a positive scalar gain and K_d a positive definite matrix. The first three terms of the control law (2.10) are a feedforward term, proportional action, and derivative action, respectively.

The last term of (2.10), $\omega_p(\dot{p} \times p)$, is a term compensating for the curvature of the sphere, more closely explained in the extended report [7]. Defining ω as the angular velocity such that $\dot{\mathcal{R}} = \mathcal{R}\mathbf{S}(\omega)$, ω_p is the component of ω parallel to p, and thus outside the space in which the input u acts. Rather than finding ω in order to express ω_p as $\omega_p = \omega^\top p$, a different expression for ω_p directly is given in [6].

The control law (2.10) gives exponential tracking of the reference q, provided the initial conditions satisfy

$$p(0) \neq -q(0), \quad k_p > \frac{\|\dot{p}(0) - \mathcal{R}(0)\dot{q}(0)\|^2}{\pi^2 - d(p(0), q(0))^2} \tag{2.11}$$

meaning that p cannot start directly opposite the reference. The closer to opposite it starts, the smaller the initial velocity error can be for a given gain k_p to still be sufficient to bring the system to its reference.

2.2 Vehicle guidance for path following

2.2.1 Line-of-sight guidance

A frequently used method for guiding marine vehicles onto and along paths, particularly straight paths, is the method of line-of-sight guidance. The vehicle is aimed at a point a distance Δ ahead along the path, called the lookahead distance. In 3D, the resulting desired direction is parametrised by the angles θ_{LOS} and ψ_{LOS} about the y- and z-axes of the path frame, respectively. The path frame is aligned such that its x-axis points along the path. The LOS angles are given in [10] as

$$\theta_{\mathrm{LOS}} = \arctan\left(\frac{z}{\Delta_z}\right) \tag{2.12a}$$

$$\psi_{\mathrm{LOS}} = -\arctan\left(\frac{y}{\Delta_y}\right) \tag{2.12b}$$

where y, z denote the position of the vehicle along the respective axes. Since the x-axis is aligned with the path, the y and z positions are also the cross-track errors perpendicular to the path. By varying the lookahead distances Δ_z, $\Delta_y > 0$, the vehicle can be made to approach the path more slowly and smoothly if they are increased, or more steeply if they are decreased.

The LOS principle of guidance relies on the vehicle travelling in the direction described by the LOS angles. For the case of straight paths and no disturbances by ocean current, the vehicle will eventually have no sway or heave velocities once it has converged to and travels along the straight path. Convergence to the path can therefore be achieved by aligning the attitude of the vehicle directly with the direction described by the LOS angles. This requires the lookahead distance to be chosen large enough for the sway and heave velocities to be small while approaching the path [10]. To take into consideration sway and heave velocities, e.g. because they are necessary when turning to follow a curved path, a frame fixed to the vehicle but aligned with its velocity can be introduced. Path-following can then be achieved by pointing this frame towards the path, rather than the vehicle directly [9].

2.2.2 Geometric guidance laws

Instead of parametrising the desired direction of travel using angles, its vector representation can also be used directly. In [47], the LOS vector pointing from the origin of the body frame of the vehicle towards a point further along the point, denoted $\boldsymbol{\mu}_1$ is expressed as

$$\boldsymbol{\mu}_1 = (k_x L)\mathbf{e}_1 - \begin{bmatrix} 0 \\ y \\ z \end{bmatrix} \tag{2.13}$$

where $k_x L$ is the lookahead distance. $\boldsymbol{\mu}_1$ can then be normalised and used as the first column of the rotation matrix describing the full desired attitude of the vehicle. In the case of passively stabilised vehicles, as considered in [47], the second body axis will always remain in the horizontal plane, and must therefore be perpendicular to both the z-axis of the world frame and $\boldsymbol{\mu}_1$.

Current compensation using geometric guidance

In [33], a guidance law formulated as a vector sum is used to take into consideration the ocean current. By choosing the desired surge such that the total speed over ground, and hence along the path, is fixed, the pointing direction of the vehicle required to stay on the path can be found. This direction is denoted $\mathbf{b}_{1d}$, being the direction of the first axis of the body frame, and is defined as

$$\mathbf{b}_{1d} = \begin{bmatrix} u_x \\ 0 \end{bmatrix} - k \begin{bmatrix} 0 \\ e \end{bmatrix} - \hat{\mathbf{V}} \tag{2.14}$$

where u_x is the desired along-path velocity, $\hat{\mathbf{V}}$ is an estimate of the current, e is the cross-track error and k is a positive scaling parameter.

The term $k[0, e]^\top$ ensures convergence towards the path. The remaining two terms ensure following of the path at the correct angle required to compensate for the ocean current. This is illustrated in Figure 2.1. The desired surge of the vehicle is chosen to be $u_{r_d} = \sqrt{(u_x - \hat{V}_x)^2 + (-\hat{V}_y)^2}$, which will make the vehicle travel with total speed u_x when the observer converges and the vehicle has no sway velocity.

Since the along-path term of the guidance law (2.14) must have magnitude u_x for the orientation to be correct once on the path, how steeply the vehicle approaches the path is instead adjusted by scaling the cross-track error by the parameter k. The greater the values of k, the steeper the approach.

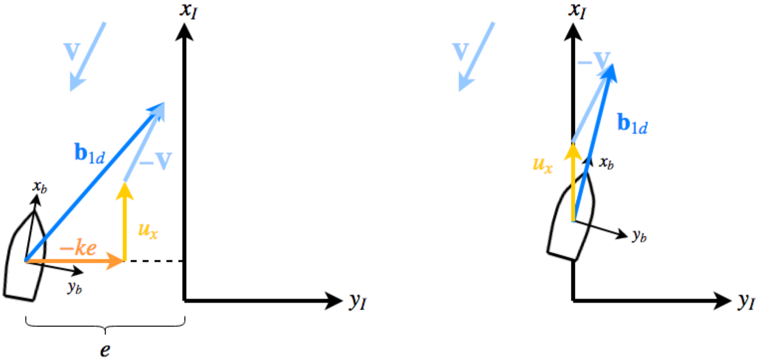

(a) Approaching the path (b) On the path

Figure 2.1: Illustration of the guidance law (2.14) for surface vessels. x_I, y_I denote the axes of the inertia frame, and x_b, y_b the axes of the body-fixed frame.

2.3 Swimming gait patterns

Underwater snake robots propel themselves forward by imitating the swimming motion of their biological inspirations. Two swimming patterns, or gaits, are often used for USRs: a gait similar to that of snakes, and also used for land-based snake robots, and a gait similar to the swimming motion of eels. They are both achieved by propagating a wave along the body of the swimmer. The motion pattern of snakes, also called lateral undulation or serpentine locomotion, is characterised by the wave propagated having constant amplitude. The motion of eels is called anguilliform swimming, and the wave propagated has a greater amplitude towards the tail [19].

When formulated as references for the joint angles, the two gaits share the generalised form

$$\phi_{i,\text{ref}}(t) = Ag(i)\sin(\omega t + (i-1)\delta) + \phi_0(t) \tag{2.15}$$

Here, $\phi_{i,\text{ref}}$ denotes the reference angle of joint i, counting from the tail of the snake, and A and ω denote amplitude and frequency of the oscillation, respectively. The phase shift δ between adjacent joints is what makes the wave travel down the body. The parameter $\phi_0(t)$ is an offset through which the robot can be made to turn [23].

A gait resembling lateral undulation is achieved by choosing $g(i) = 1$, that is equal maximum amplitude for all joints. An eel-like motion is achieved in among other [19, 23] using

$$g(i) = \frac{n-i}{n+1} \tag{2.16}$$

where n is the number of links which the robot consists of. This is also the scaling function which was used to form a gentle curve for the purpose of turning a USM in [39].

The scaling function (2.16) gives a linear increase in maximum amplitude from head to tail. However, in the motion of real eels, the increase in amplitude can be modelled as exponential [35]. For the case of continuous bodies, the scaling function $g(s)$ is expressed in the length along the body $0 < s < L$, from head to tail, and given as

$$g(s) = Ae^{\alpha(s-1)} \tag{2.17}$$

where α is a the head to tail amplitude ratio, indicating the increase in amplitude towards the tail. As α increases, the undulations in the front of the body decrease, and the swimming motion is moved towards the back part of the body only, resembling the motion of fish which swim only using their tail fin.

Chapter 3

Attitude Control

In this chapter, a tracking control law is developed for tracking the reduced attitude of a rigid body using only two control torques.

The idea of resolving the control in body coordinates, as in [36], is fused with the idea of rotating vectors into the tangent plane of the unactuated axis used in [6]. Unlike in [6], this is done for a system controlled by torques about the body axes, rather than accelerations along the surface of a sphere, and which has three rotational degrees of freedom. While the control objective is to track a reference using only the two actuated degrees of freedom, rotation about the unactuated axis will change the direction of the reference relative to the actuated axes. This is accounted for by formulating the control problem in the body frame.

An assumption is placed on the inertia of the system in order for the control law to give asymptotic tracking of the reference. The proof is given in Appendix B. Due to the resolution in body frame, the rate of change of the rotation matrix from the tangent plane of the reference to the tangent plane of the unactuated axis can be found explicitly. This is used to show that the resulting control law needs a feedforward term consisting only of parts of the acceleration of the reference in order to provide asymptotic tracking.

The realisation in coordinates, and for a system actuated by torques, also makes the control law presented in this chapter easier to implement in practical applications than the coordinate-free law of [6].

3.1 System properties

3.1.1 Dynamics and kinematics

Consider a frame b fixed to a rigid body moving in an inertial reference frame I. The attitude of the body is unactuated about the first axis of its body frame. The attitude dynamics can be written in the general, simplified form

$$\mathbf{J}\dot{\boldsymbol{\omega}}^b = \mathbf{f} + \mathbf{H}\mathbf{u} \tag{3.1}$$

where $\boldsymbol{\omega}^b \in \mathbb{R}^3$ is the angular velocity of the rigid body given in its body-fixed frame, and $\mathbf{J} = \mathbf{J}^\top > 0$ is the inertia matrix.

The term $\mathbf{u} \in \mathbb{R}^2$ in (3.1) contains the input torques, and $\mathbf{H}$ is a 3×2 matrix with the actuated axes as columns, $\mathbf{H} = [\mathbf{e}_2 \quad \mathbf{e}_3]$, where $\mathbf{e}_1$, $\mathbf{e}_2$, $\mathbf{e}_3 \in \mathbb{R}^3$ are the unit vectors. The term $\mathbf{f}$ represents all the remaining dynamics of the system. The second and third element of these dynamics are assumed to be known exactly through measurements or prior knowledge of parameters.

The inertia matrix $\mathbf{J}$ is subject to the following assumption:

Assumption 1. The inertia matrix $\mathbf{J}$ has the structure

$$\mathbf{J} = \begin{bmatrix} J_{11} & \mathbf{0} \\ \mathbf{0} & \mathbf{J}_{22} \end{bmatrix}$$

where J_{11} is a scalar and $\mathbf{J}_{22}$ is a 2×2 matrix.

Remark 1. One way to fulfil Assumption 1 is by a diagonal inertia matrix, which for rigid bodies can be obtained by aligning the body-frame axes with the principal axes of inertia [13]. This is of course only possible if two of the principal axes coincide with the actuated axes. However, it is sufficient that the rigid body has either rotational symmetry about the unactuated axis, or reflectional symmetry about the plane perpendicular to the unactuated axis and through the origin of the body frame. For marine craft, this corresponds to either bottom/top and port/starboard symmetry, or fore/aft symmetry, respectively [13]. In these cases, Assumption 1 holds also when the craft is subject to added mass effects.

The full attitude of the system is represented by the rotation matrix $\mathbf{R}_b^I$, which transforms a vector from the body-fixed frame to the inertial frame. Its derivative is given in [13] as

$$\dot{\mathbf{R}}_b^I = \mathbf{R}_b^I \mathbf{S}(\boldsymbol{\omega}^b) \tag{3.2}$$

Let the inertial frame representation of the unactuated body axis be denoted $\mathbf{x}^I$, i.e. $\mathbf{x}^I = \mathbf{R}_b^I \mathbf{e}_1$. The vector $\mathbf{x}^I$ will from now on be referred to as the reduced attitude of the body. From (3.2), it follows that its derivative is

$$\begin{aligned} \dot{\mathbf{x}}^I &= \dot{\mathbf{R}}_b^I \mathbf{e}_1 = \mathbf{R}_b^I \left(\boldsymbol{\omega}^b \times \mathbf{e}_1\right) = \mathbf{R}_b^I \left(-\mathbf{S}(\mathbf{e}_1)\boldsymbol{\omega}^b\right) \\ &= -\mathbf{R}_b^I \left(\begin{bmatrix} 0 & 0 & 0 \\ 0 & 0 & -1 \\ 0 & 1 & 0 \end{bmatrix} \boldsymbol{\omega}^b \right) \end{aligned} \tag{3.3}$$

In other words, the motion of the unactuated body axis is independent of its velocity about that axis.

3.1.2 Reference and error measures

The reference pointing direction is given in the inertial frame as a function $\mathbf{x}_{\text{ref}}^I(t)$ such that $\|\mathbf{x}_{\text{ref}}^I(t)\| = 1 \,\forall\, t$. As in [36], its angular velocity expressed in the body frame is

$$\boldsymbol{\omega}_{\text{ref}}^b = \mathbf{R}_I^b \left(\mathbf{x}_{\text{ref}}^I \times \dot{\mathbf{x}}_{\text{ref}}^I\right) = \mathbf{x}_{\text{ref}}^b \times \left(\mathbf{R}_I^b \dot{\mathbf{x}}_{\text{ref}}^I\right) \tag{3.4}$$

Note that this is not the angular velocity of the reference direction *relative* to the body frame, but relative to the inertial frame, expressed *in* the body frame. Furthermore, its derivative is

$$\begin{aligned} \dot{\boldsymbol{\omega}}_{\text{ref}}^b &= \dot{\mathbf{R}}_I^b \left(\mathbf{x}_{\text{ref}}^I \times \dot{\mathbf{x}}_{\text{ref}}^I\right) + \mathbf{R}_I^b \left(\dot{\mathbf{x}}_{\text{ref}}^I \times \dot{\mathbf{x}}_{\text{ref}}^I + \mathbf{x}_{\text{ref}}^I \times \ddot{\mathbf{x}}_{\text{ref}}^I\right) \\ &= -\boldsymbol{\omega}^b \times \mathbf{R}_I^b \left(\mathbf{x}_{\text{ref}}^I \times \dot{\mathbf{x}}_{\text{ref}}^I\right) + \mathbf{R}_I^b \left(\mathbf{x}_{\text{ref}}^I \times \ddot{\mathbf{x}}_{\text{ref}}^I\right) \\ &= -\boldsymbol{\omega}^b \times \left(\left(\mathbf{R}_I^b \mathbf{x}_{\text{ref}}^I\right) \times \left(\mathbf{R}_I^b \dot{\mathbf{x}}_{\text{ref}}^I\right)\right) + \mathbf{R}_I^b \left(\mathbf{x}_{\text{ref}}^I \times \ddot{\mathbf{x}}_{\text{ref}}^I\right) \\ &= -\boldsymbol{\omega}^b \times \boldsymbol{\omega}_{\text{ref}}^b + \mathbf{R}_I^b \left(\mathbf{x}_{\text{ref}}^I \times \ddot{\mathbf{x}}_{\text{ref}}^I\right) \end{aligned} \tag{3.5}$$

The first part is due to the movement of the frame in which $\boldsymbol{\omega}_{\text{ref}}^b$ is represented, while the second term is the acceleration of the reference in the inertial frame, transformed into the body frame.

The attitude error is the angle $\tilde{\phi} \in [0,\, \pi]$ between the reference and the body x-axis.

Using their representations in the body frame, $\tilde{\phi}$ is given as

$$\tilde{\phi} = \arccos(\mathbf{e}_1^\top \mathbf{x}_{\text{ref}}^b) \tag{3.6}$$

Then let $\tilde{\mathbf{R}}$ be defined by $\tilde{\mathbf{R}}\mathbf{x}_{\text{ref}}^b = \mathbf{e}_1$, meaning that it is the rotation matrix which rotates $\mathbf{x}_{\text{ref}}^b$ to $\mathbf{e}_1$. This corresponds to rotating an angle $\tilde{\phi}$ about the axis parallel to $\mathbf{x}_{\text{ref}}^b \times \mathbf{e}_1$. This angle-axis representation can used to find $\tilde{\mathbf{R}}$, given in [12] as

$$\tilde{\mathbf{R}} = \mathbf{I} + \sin\tilde{\phi}\mathbf{S}\left(\frac{\mathbf{x}_{\text{ref}}^b \times \mathbf{e}_1}{\|\mathbf{x}_{\text{ref}}^b \times \mathbf{e}_1\|}\right) + \left(1 - \cos\tilde{\phi}\right)\mathbf{S}\left(\frac{\mathbf{x}_{\text{ref}}^b \times \mathbf{e}_1}{\|\mathbf{x}_{\text{ref}}^b \times \mathbf{e}_1\|}\right)^2 \tag{3.7}$$

Since $\mathbf{e}_1$ and $\mathbf{x}_{\text{ref}}^b$ are unit vectors, $\|\mathbf{x}_{\text{ref}}^b \times \mathbf{e}_1\| = \sin\tilde{\phi}$, resulting in

$$\tilde{\mathbf{R}} = \mathbf{I} + \mathbf{S}\left(\mathbf{x}_{\text{ref}}^b \times \mathbf{e}_1\right) + \left(\frac{1 - \cos\tilde{\phi}}{\sin^2\tilde{\phi}}\right)\mathbf{S}\left(\mathbf{x}_{\text{ref}}^b \times \mathbf{e}_1\right)^2 \tag{3.8}$$

which is the expression used in [6].

Remark 2. $\tilde{\mathbf{R}}$ as given by (3.8) is not defined at $\tilde{\phi} = 0 \;\vee\; \pi$. The limit of $\frac{1-\cos\tilde{\phi}}{\sin^2\tilde{\phi}}$ as $\tilde{\phi}$ approaches 0 or π is $\pm\frac{1}{2}$, respectively, while $\mathbf{x}_{\text{ref}}^b \times \mathbf{e}_1$ will approach $\mathbf{0}$. $\tilde{\mathbf{R}}$ is therefore taken to be $\mathbf{I}$ at $\tilde{\phi} = 0 \vee \pi$. As a consequence of this, $\tilde{\mathbf{R}}$ is discontinuous at $\tilde{\phi} = \pi$.

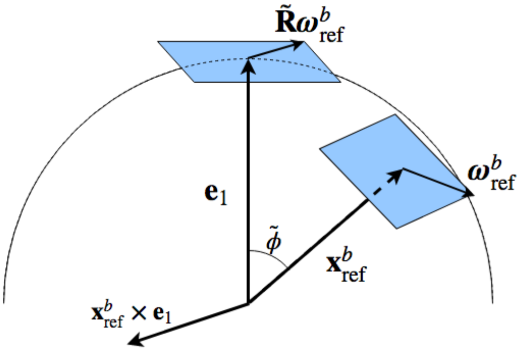

Figure 3.1: Illustration of the reference velocity $\boldsymbol{\omega}_{\text{ref}}^b$ being rotated by $\tilde{\mathbf{R}}$, and into the plane normal to the unactuated axis $\mathbf{e}_1$.

Since the angular velocity $\boldsymbol{\omega}_{\text{ref}}^b$ lies in the plane normal to $\mathbf{x}_{\text{ref}}^b$, rotating it by $\tilde{\mathbf{R}}$ rotates it into the plane normal to the body x-axis, in other words, the plane spanned by the actuated axes. This is illustrated in Figure 3.1. The rotated $\tilde{\mathbf{R}}\boldsymbol{\omega}^b_{\text{ref}}$ is therefore the current desired velocity for the body; the same angular velocity as that of the reference, but at a different point on the sphere.

3.2 Control law

Theorem 1. *The control input*

$$\begin{aligned}\mathbf{u} = \mathbf{H}^\top \Bigg(& -k_P \frac{\tilde{\phi}}{\sin\tilde{\phi}} \left(\mathbf{x}^b_{\text{ref}} \times \mathbf{e}_1\right) - k_D \left(\boldsymbol{\omega}^b - \tilde{\mathbf{R}}\boldsymbol{\omega}^b_{\text{ref}}\right) \\ & + \mathbf{J}\tilde{\mathbf{R}}\mathbf{R}^b_I \left(\mathbf{x}^I_{\text{ref}} \times \ddot{\mathbf{x}}^I_{\text{ref}}\right) - \mathbf{f} \Bigg)\end{aligned} \tag{3.9}$$

gives asymptotic tracking of the reference direction $\mathbf{x}^I_{ref}$ *by the system consisting of the reduced attitude kinematics* (3.3) *and the dynamics* (3.1)*, subject to Assumption 1, given initial conditions*

$$k_P\pi^2 > k_P\tilde{\phi}(0)^2 + \tilde{\boldsymbol{\omega}}^b(0)^\top \mathbf{J}_{22}\tilde{\boldsymbol{\omega}}^b(0) \tag{3.10}$$

where $\mathbf{J}_{22}$ *denotes the lower-right* 2×2*-block of* $\mathbf{J}$*, and* $\tilde{\boldsymbol{\omega}}^b = \mathbf{H}^\top\left(\boldsymbol{\omega}^b - \tilde{\mathbf{R}}\boldsymbol{\omega}^b_{ref}\right)$ *is the velocity tracking error.*

The proof is given in Appendix B. There it is also shown that the region of the state space specified by (3.10) is positively invariant. Consequently, $\tilde{\phi}(0) < \pi \Rightarrow \tilde{\phi} < \pi \quad \forall t \geq 0$.

Remark 3. The term $\frac{\tilde{\phi}}{\sin\tilde{\phi}}\left(\mathbf{x}^b_{\text{ref}} \times \mathbf{e}_1\right)$ is not defined at $\tilde{\phi} = 0 \ \vee \ \pi$, similarly to the case of $\tilde{\mathbf{R}}$. At these points, it is set to be 0. Due to this and the use of $\tilde{\mathbf{R}}$, the control law (3.9) is discontinuous at $\tilde{\phi} = \pi$. However, given initial conditions within the positively invariant region as specified by (3.10), $\tilde{\phi} = \pi$ will never be reached.

The term $\frac{\tilde{\phi}}{\sin\tilde{\phi}}\left(\mathbf{x}^b_{\text{ref}} \times \mathbf{e}_1\right)$ in the control law (3.9) is the axis about which the body needs to rotate in order to rotate its reduced attitude to the reference, normalised and scaled by the error angle $\tilde{\phi}$. This choice avoids the problem of diminishing control effort when the error angle $\tilde{\phi}$ grows larger than $\frac{\pi}{2}$, and consequently the norm of the vector $\mathbf{x}^b_{\text{ref}} \times \mathbf{e}_1$ decreases [6].

A less efficient, but continuous feedback law could be formulated by taking only the cross-product $\mathbf{x}^b_{\text{ref}} \times \mathbf{e}_1$ as the proportional action, and eliminating the use of $\tilde{\mathbf{R}}$.

However, if the use of $\tilde{\mathbf{R}}$ is eliminated, feedforward from the full acceleration $\dot{\boldsymbol{\omega}}^b_{\text{ref}}$ (3.5) would be required to compensate for the relative movement of the reference and the body frame.

The control law (3.9) provides feedforward only of the acceleration of the reference relative to the inertial frame, not relative to the body frame. The relative movement of the reference to the body frame is instead accounted for by rotating the reference velocity into the tangent plane of the body x-axis. The reference acceleration is also rotated into this tangent plane, in order to lie in the space spanned by the available inputs.

It is also worth noting that unlike the tracking law of [6], the control law (3.9) has no term compensating for the curvature of the sphere. This is because the inputs are torques acting about the axes of the body frame, rather than acting along the surface of the sphere.

The proposed control law (3.9) provides only local stability of $(\tilde{\phi}, \tilde{\boldsymbol{\omega}}^b) = (0, \mathbf{0})$. However, unlike control laws formulated on Euler angles, restrictions are placed only on the initial error away from the reference, and the region of attraction is stated in the body frame. This means that there is no specific forbidden reference nor state; all reference directions in the inertial frame are permitted, provided the system is not initiated facing exactly opposite the reference direction and with a too large initial velocity error.

Furthermore, by increasing k_P, the region of attraction (3.10) can be extended to encompass any initial velocity error $\tilde{\boldsymbol{\omega}}^b$.

Chapter 4

USM Model

In this chapter, the USM model developed in [41] is presented. This model is similar to the model presented and used in [45].

In Section 4.3, the kinematics of the USM from the viewpoint of the end opposite end are derived. These were not given in [41], but will be needed in order to investigate control iwth respect to either the front or the back end of the USM.

4.1 Kinematics

Following the convention used in [1,42,45,46], let the links of the robot be numbered from tail to head, meaning that the base frame in which the dynamics are given is the frame attached to the tail link. Each link has a corresponding frame with origin at the center of its cross-section at the back end of the link. This is illustrated in Figure 4.1.

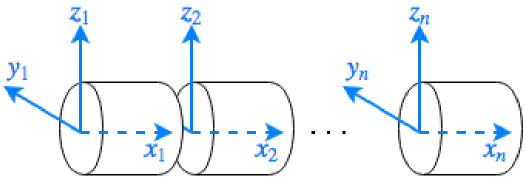

Figure 4.1: Placement of the link frames of the USM.

The USM is modelled as a chain of n cylindrical links connected by $n-1$ joints, with link 1 being the tail, or base link, and link n being the head. The joints are single-DOF joints, and the robot is assumed to have revolute joints only. Joints with multiple degrees of freedom are therefore modelled as two consecutive joints with a short additional link between them. Each link has a corresponding reference frame with origin at the center of its back. The position and orientation of the frame attached to link i in an inertial reference frame I is given by the transformation

$$\mathbf{H}_i = \begin{bmatrix} \mathbf{R}_i^I & \mathbf{p}_i \\ \mathbf{0} & 1 \end{bmatrix} \tag{4.1}$$

where $\mathbf{R}_i^I$ is the rotation matrix transforming a vector from link frame i to the inertial frame, and $\mathbf{p}_i$ is the position of the origin of link frame i given in the inertial frame. The transformation $\mathbf{A}_i(\theta_i)$ is defined as the transformation mapping from the frame of link $i+1$ to the frame of link i, and is a function of the angle θ_i of joint i. Given the transformation $\mathbf{H}_1$ describing the position and orientation of the base link frame in the inertial frame, the consecutive link frames can then be found recursively as

$$\mathbf{H}_{i+1} = \mathbf{H}_i \mathbf{A}_i(\theta_i) \tag{4.2}$$

The transformations $\mathbf{A}_i(\theta_i)$ can be written as

$$\begin{aligned} \mathbf{A}_i(\theta_i) &= \mathbf{A}_i(0) \begin{bmatrix} \mathbf{R}(\boldsymbol{\lambda}_i, \theta_i) & \mathbf{0} \\ \mathbf{0} & 1 \end{bmatrix}, \\ \mathbf{A}_i(0) &= \begin{bmatrix} \mathbf{I}_3 & l_i \mathbf{e}_1 \\ \mathbf{0} & 1 \end{bmatrix} \end{aligned} \tag{4.3}$$

where $\mathbf{R}(\boldsymbol{\lambda}_i, \theta_i)$ is the rotation matrix describing the rotation about the joint axis $\boldsymbol{\lambda}_i$ of joint i by an angle θ_i, and l_i is the length of joint i. In other words, the transformation consists of a rotation due to the joint position, and a translation to the start of the next link.

The velocities of the links given in their individual frames are found be means of the adjoint operator of the transformations. The adjoint operator is given as

$$\mathrm{Ad}(\mathbf{H}_i) = \begin{bmatrix} \mathbf{R}_i^I & \mathbf{S}(\mathbf{p}_i)\mathbf{R}_i^I \\ \mathbf{0} & \mathbf{R}_i^I \end{bmatrix} \tag{4.4}$$

and its inverse as

$$\mathrm{Ad}^{-1}(\mathbf{H}_i) = \begin{bmatrix} {\mathbf{R}_i^I}^\top & -{\mathbf{R}_i^I}^\top \mathbf{S}(\mathbf{p}_i) \\ \mathbf{0} & {\mathbf{R}_i^I}^\top \end{bmatrix} = \mathrm{Ad}(\mathbf{H}_i^{-1}) \tag{4.5}$$

Given the generalised velocity $\boldsymbol{\nu}_1 = [\mathbf{v}_1^\top \quad \boldsymbol{\omega}_1^\top]^\top$ of the base frame, from now on referred to as just the velocity, the velocities $\boldsymbol{\nu}_i$ of the links in their own respective frames can then be found recursively as

$$\boldsymbol{\nu}_{i+1} = \mathrm{Ad}^{-1}(\mathbf{A}_i(\theta_i))\boldsymbol{\nu}_i + \boldsymbol{\xi}_i\dot{\theta}_i \tag{4.6}$$

where $\boldsymbol{\xi}_i$ is the joint twist of joint i, which for revolute joints is $\boldsymbol{\xi}_i = [\mathbf{0} \quad \boldsymbol{\lambda}_i^\top]^\top$.

Instead of finding the joint velocities recursively, they can be found from the vector $\boldsymbol{\zeta} = [\boldsymbol{\nu}_1^\top \quad \dot{\boldsymbol{\theta}}^\top]^\top$ containing the velocity of the base link and the joint velocities $\dot{\theta}_i$ gathered in the vector $\dot{\boldsymbol{\theta}}$. The velocities $\boldsymbol{\nu}_i$ are then given as

$$\boldsymbol{\nu}_i = \mathbf{J}_i\boldsymbol{\zeta} \tag{4.7}$$

where $\mathbf{J}_i$ are Jacobian matrices given as

$$\mathbf{J}_1 = [\mathbf{I}_6 \quad \mathbf{0} \quad \dots \quad \mathbf{0}] \tag{4.8a}$$

$$\mathbf{J}_{i+1} = \mathrm{Ad}^{-1}(\mathbf{A}_i(\theta_i))\mathbf{J}_i + [\mathbf{0}_{6\times 6} \quad \mathbf{0} \quad \dots \quad \boldsymbol{\xi}_i \quad \mathbf{0} \quad \dots \quad \mathbf{0}] \tag{4.8b}$$

Their time derivatives are given as

$$\dot{\mathbf{J}}_1 = [\mathbf{0}_{6\times 6} \quad \mathbf{0} \quad \dots \quad \mathbf{0}] \tag{4.9a}$$

$$\dot{\mathbf{J}}_{i+1} = -\mathrm{ad}(\boldsymbol{\xi}_i)\mathbf{J}_{i+1}\dot{\theta}_i + \mathrm{Ad}^{-1}(\mathbf{A}_i(\theta_i))\dot{\mathbf{J}}_i \tag{4.9b}$$

where the ad-operator is defined for a vector $\boldsymbol{\nu} = [\mathbf{v}^\top \quad \boldsymbol{\omega}^\top]^\top$ as

$$\mathrm{ad}(\boldsymbol{\nu}) = \begin{bmatrix} \mathbf{S}(\boldsymbol{\omega}) & \mathbf{S}(\mathbf{v}) \\ \mathbf{0} & \mathbf{S}(\boldsymbol{\omega}) \end{bmatrix} \tag{4.10}$$

For simulation purposes, the orientation of the base frame is parametrised using a unit quaternion $\mathbf{q}$ rather than the full rotation matrix $\mathbf{R}_1^I$. Given $\mathbf{q} = [\eta \quad \boldsymbol{\epsilon}^\top]^\top \in \mathbb{R}^4$, $|\mathbf{q}| = 1$, the rotation matrix $\mathbf{R}_1^I$ is then given as

$$\mathbf{R}_1^I(\mathbf{q}) = \mathbf{I}_3 + 2\eta\mathbf{S}(\boldsymbol{\epsilon}) + 2\mathbf{S}(\boldsymbol{\epsilon})^2 \tag{4.11}$$

The time evolution of $\mathbf{q}$ can be found as

$$\dot{\mathbf{q}} = \mathbf{T}_q(\mathbf{q})\boldsymbol{\omega}_1, \quad \mathbf{T}_q(\mathbf{q}) = \frac{1}{2}\begin{bmatrix} -\boldsymbol{\epsilon}^\top \\ \eta\mathbf{I}_3 + \mathbf{S}(\boldsymbol{\epsilon}) \end{bmatrix} \tag{4.12}$$

where $\boldsymbol{\omega}_1$ is the angular velocity of the base frame. The kinematics of the base frame are then given in [13] as

$$\dot{\boldsymbol{\eta}} = \begin{bmatrix} \mathbf{R}_1^I(\mathbf{q}) & \mathbf{0}_{3\times3} \\ \mathbf{0}_{4\times3} & \mathbf{T}_q(\mathbf{q}) \end{bmatrix} \boldsymbol{\nu} = \mathbf{T}(\boldsymbol{\eta})\boldsymbol{\nu}_1 \tag{4.13}$$

where $\boldsymbol{\eta} = \begin{bmatrix} \mathbf{p}_1^\top & \mathbf{q}^\top \end{bmatrix}^\top$ contains the position and orientation of the base frame.

4.2 Dynamics

The dynamics and kinematics together are given in [41] as

$$\dot{\boldsymbol{\eta}} = \mathbf{T}(\boldsymbol{\eta})\boldsymbol{\nu}_1 \tag{4.14a}$$

$$\mathbf{M}(\boldsymbol{\theta})\dot{\boldsymbol{\zeta}} + \mathbf{C}(\boldsymbol{\theta}, \boldsymbol{\zeta})\boldsymbol{\zeta} + \mathbf{D}(\boldsymbol{\theta}, \boldsymbol{\zeta})\boldsymbol{\zeta} + \mathbf{g}(\boldsymbol{\eta}, \boldsymbol{\theta}) = \mathbf{B}(\boldsymbol{\theta})\mathbf{u} + \begin{bmatrix} \mathbf{0}_6 \\ \boldsymbol{\tau} \end{bmatrix} \tag{4.14b}$$

where $\mathbf{u}$ and $\boldsymbol{\tau}$ are inputs, respectively thruster forces and joint torques. The matrix $\mathbf{M}(\boldsymbol{\theta})$ has the form

$$\mathbf{M}(\boldsymbol{\theta}) = \sum_{i=1}^{n} \mathbf{J}_i(\boldsymbol{\theta})^\top \mathbf{M}_i(\boldsymbol{\theta}) \mathbf{J}_i(\boldsymbol{\theta}) \tag{4.15}$$

The matrices $\mathbf{M}_i$ consists of the rigid body mass and inertia matrix of link i plus the added mass effects acting on the respective link:

$$\begin{aligned} \mathbf{M}_i &= \mathbf{M}_{R,i} + \mathbf{M}_{A,i}, \\ \mathbf{M}_{R,i} &= \begin{bmatrix} m_i\mathbf{I}_3 & m_i\mathbf{S}(\mathbf{r}_{g,i})^\top \\ m_i\mathbf{S}(\mathbf{r}_{g,i}) & \mathbf{I}_{R,i} \end{bmatrix} \end{aligned} \tag{4.16}$$

where $\mathbf{I}_{R,i}$ is the rigid body inertia matrix of link i. The added mass matrix $\mathbf{M}_{A,i}$, for cylindrical links with common radius r and individual lengths l_i is given as

$$\mathbf{M}_{A,i} = \rho\pi r^2 l_i C_a \begin{bmatrix} \alpha_i & 0 & 0 & 0 & 0 & 0 \\ 0 & 1 & 0 & 0 & 0 & \frac{1}{2}l_i \\ 0 & 0 & 1 & 0 & -\frac{1}{2}l_i & 0 \\ 0 & 0 & 0 & 0 & 0 & 0 \\ 0 & 0 & -\frac{1}{2}l_i & 0 & -\frac{1}{3}l_i^2 & 0 \\ 0 & \frac{1}{2}l_i & 0 & 0 & 0 & \frac{1}{3}l_i^2 \end{bmatrix} \tag{4.17}$$

with ρ being the density of water, C_a the added mass coefficient, and α_i a parameter allowing to include added mass effects in surge.

The matrix $\mathbf{C}(\boldsymbol{\theta}, \boldsymbol{\zeta})$ in (4.14b) has the expression

$$\mathbf{C}(\boldsymbol{\theta}, \boldsymbol{\zeta}) = \sum_{i=1}^{n} \left(\mathbf{J}_i(\boldsymbol{\theta})^\top \mathbf{M}_i(\boldsymbol{\theta}) \dot{\mathbf{J}}_i(\boldsymbol{\theta}, \dot{\boldsymbol{\theta}}) - \mathbf{J}_i(\boldsymbol{\theta})^\top \mathbf{W}_i(\boldsymbol{\theta}, \boldsymbol{\zeta}) \mathbf{J}_i(\boldsymbol{\theta}) \right), \tag{4.18}$$

$$\mathbf{W}_i(\boldsymbol{\theta}, \boldsymbol{\zeta}) = \begin{bmatrix} 0 & \mathbf{S}(\{\mathbf{M}_i\boldsymbol{\nu}_i\}_v) \\ \mathbf{S}(\{\mathbf{M}_i\boldsymbol{\nu}_i\}_v) & \mathbf{S}(\{\mathbf{M}_i\boldsymbol{\nu}_i\}_\omega) \end{bmatrix} \tag{4.19}$$

where $\{\mathbf{M}_i\boldsymbol{\nu}_i\}_v$, $\{\mathbf{M}_i\boldsymbol{\nu}_i\}_\omega \in \mathbb{R}^3$ denote the first and last three entries respectively of $\mathbf{M}_i\boldsymbol{\nu}_i$.

The influence of hydrodynamic damping is modelled by the matrix $\mathbf{D}(\boldsymbol{\theta}, \boldsymbol{\zeta})$ in (4.14b), which is given as

$$\mathbf{D}(\boldsymbol{\theta}, \boldsymbol{\zeta}) = \sum_{i=1}^{n} \mathbf{J}_i(\boldsymbol{\theta})^\top \mathbf{D}_i(\boldsymbol{\theta}) \mathbf{J}_i(\boldsymbol{\theta}) \tag{4.20}$$

The matrices $\mathbf{D}_i$ are the hydrodynamic damping matrices of each respective link, such that $\mathbf{D}_i(\boldsymbol{\nu}_i)\boldsymbol{\nu}_i$ gives the hydrodynamic forces and moments on link i. The full expressions of these matrices are given in [41].

The generalised hydrostatic force $\mathbf{g}(\boldsymbol{\eta}, \boldsymbol{\theta})$ consists of the forces and moments on the base link, as well as the moments acting on the joints due to the hydrostatic forces on the individual links of the robot. The generalised hydrostatic force is given as

$$\mathbf{g}(\boldsymbol{\eta}, \boldsymbol{\theta}) = \sum_{i=1}^{n} \mathbf{J}_i(\boldsymbol{\theta})^\top \mathbf{g}_i(\boldsymbol{\eta}, \boldsymbol{\theta}) \tag{4.21}$$

with $\mathbf{g}_i(\boldsymbol{\eta}, \boldsymbol{\theta})$ being the hydrostatic forces and moments on link i, which are

$$\mathbf{g}_i(\boldsymbol{\eta}, \boldsymbol{\theta}) = \mathbf{G}_i {\mathbf{R}_i^I}^\top \boldsymbol{\gamma}_0 \tag{4.22}$$

where $\boldsymbol{\gamma}_0$ is the direction of gravity in the inertial frame, taken to be constant. The matrices $\mathbf{G}_i \in \mathbb{R}^{6\times 3}$ are also constant, and given as

$$\mathbf{G}_i = \begin{bmatrix} (\rho v_i g - m_i g)\mathbf{I}_3 \\ \rho v_i g \mathbf{S}(\mathbf{r}_{b,i}) - m_i g \mathbf{S}(\mathbf{r}_{g,i}) \end{bmatrix} \tag{4.23}$$

where ρ is the density of water, g the gravitational constant, and m_i, v_i the mass and volume of link i, respectively. The vectors $\mathbf{r}_{g,i}$, $\mathbf{r}_{b,i}$ are the locations of the center of gravity, or center of mass, and center of buoyancy (CB) of link i in its respective frame.

The matrix $\mathbf{B}(\boldsymbol{\theta})$ is the thrust configuration matrix (TCM), and depends on the configuration of the joints, as the position of thrusters and their direction of thrust relative to the base link will depend on the configuration on the robot. It is expressed as

$$\mathbf{B}(\boldsymbol{\theta}) = \begin{bmatrix} \mathbf{J}_1(\boldsymbol{\theta})^\top \mathbf{B}_1 & \mathbf{J}_2(\boldsymbol{\theta})^\top \mathbf{B}_2 & \dots & \mathbf{J}_n(\boldsymbol{\theta})^\top \mathbf{B}_n \end{bmatrix} \tag{4.24}$$

The matrices $\mathbf{B}_i$ are the thrust configuration matrices for the thrusters mounted on each individual link. They are constant and expressed as

$$\mathbf{B}_i = \begin{bmatrix} \boldsymbol{\beta}_{t,i,1} & \boldsymbol{\beta}_{t,i,2} & \dots & \boldsymbol{\beta}_{t,i,m} \\ \mathbf{r}_{t,i,1} \times \boldsymbol{\beta}_{t,i,1} & \mathbf{r}_{t,i,2} \times \boldsymbol{\beta}_{t,i,2} & \dots & \mathbf{r}_{t,i,m} \times \boldsymbol{\beta}_{t,i,m} \end{bmatrix} \tag{4.25}$$

where $\boldsymbol{\beta}_{t,i,j}$ is the thrust direction of thruster j of the m thrusters mounted on link i, and $\mathbf{r}_{t,i,j}$ is its point of attack given in the frame of link i.

4.3 End-effector kinematics

For many tasks, it is relevant to control not only the base of the USM, but also the front end of its head where an end-effector is located, which might be a tool or camera.

The transformation $\mathbf{A}_e$ from the frame of the head link, with origin at its back, to the end-effector frame located at its front is simply a translation

$$\mathbf{A}_e = \begin{bmatrix} \mathbf{I}_3 & l_n\mathbf{e}_1 \\ \mathbf{0} & 1 \end{bmatrix} \tag{4.26}$$

The position $\mathbf{p}_e$ and orientation $\mathbf{R}_e$ of the end-effector relative to the inertial frame is the found by means of the transformation

$$\mathbf{H}_e = \begin{bmatrix} \mathbf{R}_e^I & \mathbf{p}_e \\ \mathbf{0} & 1 \end{bmatrix} = \mathbf{H}_n\mathbf{A}_e \tag{4.27}$$

Similarly to the relationship between the velocity of consecutive link frames (4.6), the velocity of the end-effector can be found as

$$\boldsymbol{\nu}_e = \mathrm{Ad}^{-1}(\mathbf{A}_e)\boldsymbol{\nu}_n = \mathrm{Ad}^{-1}(\mathbf{A}_e)\mathbf{J}_n\boldsymbol{\nu}_1 \tag{4.28}$$

Jacobian matrices with respect to the end-effector

In order to control the end-effector directly, matrices giving the forces due to thrusters and inertia with respect to the end-effector must be found. The required matrices are the equivalents of $\mathbf{M}(\boldsymbol{\theta})$ and $\mathbf{B}(\boldsymbol{\theta})$, and can be found by replacing the Jacobian matrices $\mathbf{J}_i$ used in (4.15), (4.24) with new Jacobian matrices $\mathbf{J}_{\mathrm{end},i}$ defined implicitly as

$$\boldsymbol{\nu}_i = \mathbf{J}_{e,i} \begin{bmatrix} \boldsymbol{\nu}_{\mathrm{end}} \\ \dot{\boldsymbol{\theta}} \end{bmatrix} \tag{4.29}$$

The matrices $\mathbf{J}_{\mathrm{end},i}$ can be used to find the velocities of the link frames given the velocity of the end-effector, rather than the base link.

The recursive relationship between the velocities of consecutive frames (4.6) reversed gives

$$\boldsymbol{\nu}_i = \mathrm{Ad}(\mathbf{A}_i(\theta_i))\boldsymbol{\nu}_{i+1} - \mathrm{Ad}(\mathbf{A}_i(\theta_i))\boldsymbol{\xi}_i\dot{\theta}_i \tag{4.30}$$

Following the same pattern as (4.8), the Jacobian matrices $\mathbf{J}_{\mathrm{end},i}$ can then be found as

$$\mathbf{J}_{\mathrm{end},n} = [\mathrm{Ad}(\mathbf{A}_e) \quad \mathbf{0} \quad \dots \quad \mathbf{0}] \tag{4.31a}$$

$$\mathbf{J}_{\mathrm{end},i} = \mathrm{Ad}(\mathbf{A}_i(\theta_i))\mathbf{J}_{\mathrm{end},i+1} - [\mathbf{0}_{6\times 6} \quad \mathbf{0} \quad \dots \quad \mathrm{Ad}(\mathbf{A}_i(\theta_i))\boldsymbol{\xi}_i \quad \mathbf{0} \quad \dots \quad \mathbf{0}] \tag{4.31b}$$

Chapter 5

Guidance and Control of USMs

In this chapter, a path following method for USMs moving in 3D is presented. The paths considered are straight lines, and the guidance law is an extension of the guidance law from [33] for surface vessels. Environmental disturbances, such as ocean currents, are not considered in this thesis.

Based on the control law presented in Chapter 3, a method for controlling the direction of travel using the joints of the USM is proposed. The concept of controlling the direction using just the joints of the USM comes from the approach used in [39] for following a planar spiral path.

The primary objective of using the joints for direction control is to reduce the usage of thrusters, and using longitudinal thrusters for forward propulsion. If a USM possesses multiple longitudinal thrusters, typically mounted on either side of the same link, those can be exploited to use them for additional help in turning the robot.

First, the control objective is formalised in Section 5.1, then the guidance law used to guide the USM towards the path is presented in Section 5.2. The method of direction control is described in Section 5.3, including the different shapes which will be considered in later simulations. Finally, Section 5.4 presents the ways in which thrusters will be used, both a simple surge controller, and a thrust allocation algorithm used to distribute control effort between available thrusters.

5.1 Control objective

The task to be solved is for the end-effector of a USM to converge towards and follow a straight path in 3D space. Without loss of generality, the path is the x-axis of an inertial reference frame, denoted I. For the purpose of navigation within a local area, the North-East-Down (NED) reference frame, where the x- and y-axes span a plane tangent to the surface of the earth, can be considered inertial [13]. Non-horizontal paths can be represented by choosing an inertial frame in which the direction of gravity is different.

The control objective of following the path is then equivalent to driving the y- and z-positions p_y, p_z of the end-effector in the inertial frame to 0, while maintaining a desired forward velocity u_d. In this thesis, u_d is chosen to be constant.

5.2 Guidance

The guidance law from [33] can easily be extended to the 3D case. Without considering ocean currents, the desired direction of travel $\boldsymbol{\mu}^I_{\text{ref}}$ is given as

$$\boldsymbol{\mu}^I_{\text{ref}} = u_d\mathbf{e}_1 - k_e \begin{bmatrix} 0 \\ p_y \\ p_z \end{bmatrix} \tag{5.1}$$

where u_d is the desired forward velocity, and k_e a design parameter. Figure 5.1 illustrates the resulting desired direction of travel. Increasing the parameter k_e leads to a greater weighting of the cross-track error in the guidance law (5.1), and consequently to a steeper approach towards the path.

By weighting the cross-track error by a design parameter while keeping the length of the component along the x-axis fixed, the guidance law (5.1) is ready for a future addition of an observer to compensate for an ocean current as in [33].

The relation to LOS guidance can be seen by letting $k_e = \frac{u_d}{\Delta}$. Comparing this to the LOS guidance laws (2.12) for pitch and yaw angles, this corresponds to an equal look-ahead distance Δ in both pitch and yaw. The effect of different look-ahead distances in the horizontal and vertical planes can be achieved by replacing the scalar gain k_e with a diagonal gain matrix.

The guidance law (5.1) does not take into consideration sway or heave velocities, as they will eventually converge to zero when the USM follows the straight path. If the USM, and specifically its end-effector, has non-zero sway and heave, its direction

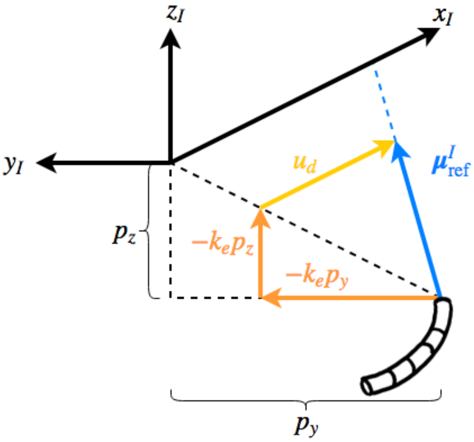

Figure 5.1: Illustration of the guidance law (5.1). The axes of the inertial frame are denoted x_I, y_I, z_I.

of motion will not be the same as the pointing direction of the end-effector. If aligning the pointing direction of the end-effector frame with the desired direction (5.1) is to result in truly travelling in that direction, the approach towards the path must be gentle enough for the sway and heave velocities to remain small.

5.2.1 Reference reduced attitude, angular velocity and acceleration

The reference for the reduced attitude of the end-effector is the unit vector parallel to the desired direction of travel (5.1), which is simply

$$\mathbf{x}^I_{\text{ref}} = \frac{\boldsymbol{\mu}^I_{\text{ref}}}{\|\boldsymbol{\mu}^I_{\text{ref}}\|} \tag{5.2}$$

where $\|\boldsymbol{\mu}^I_{\text{ref}}\| = \sqrt{u_d^2 + (k_e p_y)^2 + (k_e p_z)^2}$. The derivative of (5.2), required to compute the reference angular velocity, can be written as

$$\dot{\mathbf{x}}^I_{\text{ref}} = \frac{\mathrm{d}}{\mathrm{d}t}\left(\frac{1}{\|\boldsymbol{\mu}^I_{\text{ref}}\|}\right)\boldsymbol{\mu}^I_{\text{ref}} + \frac{1}{\|\boldsymbol{\mu}^I_{\text{ref}}\|}\dot{\boldsymbol{\mu}}^I_{ref} \tag{5.3}$$

The term parallel to $\boldsymbol{\mu}^I_{\text{ref}}$ and therefore also to $\mathbf{x}^I_{\text{ref}}$ will have no contribution to the angular velocity $\boldsymbol{\omega}^b_{\text{ref}}$. The first term of (5.3) is due to the change of the length of $\boldsymbol{\mu}^I_{\text{ref}}$, in other words movement along the direction $\boldsymbol{\mu}^I_{\text{ref}}$, which does not contribute to the angular velocity of the tip of this vector.

With some abuse of notation, let $\dot{\mathbf{x}}^I_{\text{ref},\nparallel}$ denote the part of $\dot{\mathbf{x}}^I_{\text{ref}}$ which is not necessarily parallel to $\boldsymbol{\mu}^I_{\text{ref}}$, such that $\mathbf{x}^I_{\text{ref}} \times \dot{\mathbf{x}}^I_{\text{ref}} = \mathbf{x}^I_{\text{ref}} \times \dot{\mathbf{x}}^I_{\text{ref},\nparallel}$. Then $\dot{\mathbf{x}}^I_{\text{ref},\nparallel}$ is found as

$$\begin{aligned}\dot{\mathbf{x}}^I_{\text{ref},\nparallel} &= \frac{1}{\|\boldsymbol{\mu}^I_{\text{ref}}\|}\dot{\boldsymbol{\mu}}^I_{\text{ref}} \\ &= \frac{-k_e}{\|\boldsymbol{\mu}^I_{\text{ref}}\|}\begin{bmatrix}0\\ \dot{p}_y\\ \dot{p}_z\end{bmatrix} = \frac{-k_e}{\|\boldsymbol{\mu}^I_{\text{ref}}\|}\begin{bmatrix}0&0&0\\0&1&0\\0&0&1\end{bmatrix}\mathbf{R}^I_e\mathbf{v}^e\end{aligned} \tag{5.4}$$

where $\mathbf{R}^I_e$ is the rotation matrix rotating a vector from the end-effector frame e to the inertial frame, and $\mathbf{v}^e$ is the velocity of the end-effector, given in the end-effector frame.

The reference angular velocity, given in end-effector frame, is therefore found by replacing $\dot{\mathbf{x}}^I_{\text{ref}}$ in (3.4), which gives

$$\boldsymbol{\omega}^e_{\text{ref}} = \mathbf{x}^e_{\text{ref}} \times \left(\mathbf{R}^e_I\dot{\mathbf{x}}^I_{\text{ref},\nparallel}\right) \tag{5.5}$$

Similarly, $\ddot{\mathbf{x}}^I_{\text{ref}}$ will have components not contributing to the angular acceleration of the reference. Differentiation of (5.3) gives

$$\ddot{\mathbf{x}}^I_{\text{ref}} = \frac{\mathrm{d}^2}{\mathrm{d}t^2}\left(\frac{1}{\|\boldsymbol{\mu}^I_{\text{ref}}\|}\right)\boldsymbol{\mu}^I_{\text{ref}} + 2\frac{\mathrm{d}}{\mathrm{d}t}\left(\frac{1}{\|\boldsymbol{\mu}^I_{\text{ref}}\|}\right)\dot{\boldsymbol{\mu}}^I_{ref} + \frac{1}{\|\boldsymbol{\mu}^I_{\text{ref}}\|}\ddot{\boldsymbol{\mu}}^I_{\text{ref}} \tag{5.6}$$

Denoting by $\ddot{\mathbf{x}}^I_{\text{ref},\nparallel}$ the parts of $\ddot{\mathbf{x}}^I_{\text{ref}}$ that do contribute to the acceleration, this gives

$$\begin{aligned}\ddot{\mathbf{x}}^I_{\text{ref},\nparallel} &= 2\frac{\mathrm{d}}{\mathrm{d}t}\left(\frac{1}{\|\boldsymbol{\mu}^I_{\text{ref}}\|}\right)\dot{\boldsymbol{\mu}}^I_{ref} + \frac{1}{\|\boldsymbol{\mu}^I_{\text{ref}}\|}\ddot{\boldsymbol{\mu}}^I_{ref} \\ &= 2\frac{\mathrm{d}}{\mathrm{d}t}\left(\frac{1}{\|\boldsymbol{\mu}^I_{\text{ref}}\|}\right)\cdot\left(-k_e\begin{bmatrix}0&0&0\\0&1&0\\0&0&1\end{bmatrix}\mathbf{R}^I_e\mathbf{v}^e\right) \\ &\quad - k_e\begin{bmatrix}0&0&0\\0&1&0\\0&0&1\end{bmatrix}\left(-\mathbf{R}^I_e\boldsymbol{\omega}^e \times \mathbf{v}^e + \mathbf{R}^I_e\dot{\mathbf{v}}^e\right)\end{aligned} \tag{5.7}$$

where

$$\begin{aligned}\frac{\mathrm{d}}{\mathrm{d}t}\left(\frac{1}{\|\boldsymbol{\mu}^I_{\text{ref}}\|}\right) &= -\frac{\frac{1}{2\|\boldsymbol{\mu}^I_{\text{ref}}\|}}{\|\boldsymbol{\mu}^I_{\text{ref}}\|^2}\left(2k_ep_y\dot{p}_y + 2k_ep_z\dot{p}_z\right) \\ &= -\frac{k_e}{\|\boldsymbol{\mu}^I_{\text{ref}}\|^3}\begin{bmatrix}0 & p_y & p_z\end{bmatrix}\mathbf{R}^I_e\mathbf{v}^e\end{aligned} \tag{5.8}$$

The acceleration $\dot{\mathbf{v}}^e$ of the end-effector appearing in (5.7) will be implemented simply as the numerical derivative of $\mathbf{v}^e$. If all parameters of the dynamics are known, it can also be found by reformulating the full dynamics (4.14b) for the state of the end-effector rather than the base link.

5.3 Direction control

The direction in which the USM travels will be controlled using its joints to curve the body of the USM, as was done in the planar case in [39].

The USMs considered in this thesis have joints with 2 DOF, which can be rotated about their y- and z-axes. As stated in Chapter 4, each such joint is modelled as two consecutive single-DOF joints, with a short link between them. Since the frames of all links have the same orientation when the robot is straightened, rotating all joints about the z-axis forms a curve in the horizontal plane, while rotating all joints about the y-axis forms a curve in the vertical plane.

The curves, or body shapes which will be used in this thesis are described by a base angle, and a scaling function for scaling the joint angle along the length of the body. The base angles for the joints actuated about y- and z-axes will therefore serve as two control inputs for the pointing direction of the head of the USM.

The roll of the end-effector becomes unactuated under this control scheme. The roll does not influence the pointing direction of end-effector, however, it does influence the orientation of the joints in the inertial frame, and consequently the direction of the curve. The control laws for the base angles must therefore give correct distribution of the control effort between the two sets of joints forming the body curve.

By using a geometric law formulated in the end-effector frame, there is no need for additional decomposition of the reference direction into rotations about the actuated body axes, as the geometric error lies in the space spanned by the actuated axes directly.

5.3.1 Base joint angle

Let $\theta_{y,0}$ and $\theta_{z,0}$ denote the base reference angle of joints actuated about their y- and z-axes respectively. Similarly to the control law (3.9), these are chosen to be

$$\begin{bmatrix}\theta_{y,0}\\ \theta_{z,0}\end{bmatrix} = \mathbf{H}^\top \left(-k_P \frac{\tilde{\phi}}{\sin\tilde{\phi}} \left(\mathbf{x}^e_{\text{ref}} \times \mathbf{e}_1\right) - k_D \left(\boldsymbol{\omega}^e - \tilde{\mathbf{R}}\boldsymbol{\omega}^e_{\text{ref}}\right) + \tilde{\mathbf{R}}\mathbf{R}^e_I \left(\mathbf{x}^I_{\text{ref}} \times \ddot{\mathbf{x}}^I_{\text{ref},\nparallel}\right)\right) \tag{5.9}$$

where $\boldsymbol{\omega}^e$ is the angular velocity of the end-effector, given in the end-effector frame, and $\tilde{\phi}$, $\tilde{\mathbf{R}}$ are, as in Chapter 3, the angle between current and desired pointing direction, and the rotation matrix rotating the desired pointing direction to the current pointing direction. The reference direction $\mathbf{x}^I_{\text{ref}}$, reference angular velocity $\boldsymbol{\omega}^e_{\text{ref}}$, and acceleration term $\ddot{\mathbf{x}}^I_{\text{ref},\nparallel}$ are given by (5.2), (5.5) and (5.7), respectively.

The base angles (5.9) do not influence the pointing direction directly as input torques do. Rather, the curve of the body combined with forward velocity will cause the USM to turn. The last term of (5.9) will therefore not necessarily lead to perfect tracking of the reference once aligned, but is used to incorporate some information about the future motion of the reference.

As in Chapter 3, the term $\frac{\tilde{\phi}}{\sin\tilde{\phi}}\left(\mathbf{x}^e_{\text{ref}} \times \mathbf{e}_1\right)$ is set to zero when the vectors $\mathbf{x}^e_{\text{ref}}$ and $\mathbf{e}_1$ are parallel. This means that if the USM is pointing opposite to the reference direction $\mathbf{x}^I_{\text{ref}}$, the angular velocity error $\boldsymbol{\omega}^e - \tilde{\mathbf{R}}\boldsymbol{\omega}^e_{\text{ref}}$ is zero and the reference has no angular acceleration, the choice (5.9) of base angles will give zero. However, the only situation in which the USM can remain in such a state is if it travels along the path in the opposite direction, with already straightened joints.

5.3.2 Body curves

The idea of curving the body to control direction of travel is inspired by the motion of biological swimmers. In addition, if trying to follow an oscillating course in this manner, swimming-like motions could arise. The shape of the curve is therefore likewise inspired by the behaviour of biological swimmers.

The shape defining functions in this section are formulated for USMs possessing an equal number of joints actuated about the y- and z-axes. The number of links must therefore be odd, $n = 2m + 1$, where m is the number of joints of each kind.

Let $\theta_{y,j}$ denote the joints actuated about the y-axis of the frame of the link to which they are attached, and $\theta_{z,k}$ the joints actated about the z-axis. The indices $j, k = 1, \quad ..., \quad m$ denote the number of the joint among the joints of the same kind, numbered from tail to head.

The references for each joint are chosen as

$$\theta^*_{a,i} = g(i)\,\mathrm{sat}(\theta_{a,0}) \tag{5.10}$$

where a is either y or z. The function $g(i)$ is a scaling function depending on the index of a joint, and $\mathrm{sat}(x)$ is a saturating function

$$\mathrm{sat}(x) = \begin{cases} x, & |x| \leq \theta_{0,\max} \\ \theta_{0,\max}, & |x| > \theta_{0,\max} \end{cases} \tag{5.11}$$

Scaling functions

Three different scaling functions will be examined in this thesis:

$$g_1(i) = 1 \tag{5.12a}$$

$$g_2(i) = \frac{m+1-i}{m} \tag{5.12b}$$

$$g_3(i) = e^{-\alpha(i-1)} \tag{5.12c}$$

The first scaling function (5.12a) simply sets all angle references to the base angle (5.9), resulting in a uniform curve such as previously used in [43, 45].

The second scaling function (5.12b) is similar to the scaling function (2.16) used to generate eel-like motions for USRs, and which was applied to USMs in [39] in order to form a curve with increasing curvature towards the back. The function (5.12b) has a greater slope and is shifted compared to (2.16). The choice (5.12b) of linear scaling function gives

$$g_k(1) = 1, \quad k = 1,\, 2,\, 3.$$

In other words, the scaling functions equations (5.12a)-(5.12c) all set the reference for the backmost joint to the base angle.

The third, exponential scaling function (5.12c) is proposed in this thesis, and inspired by the head-to-tail amplitude ratio of biological eels [35]. This gives a curve with increasing curvature towards the back of the body of the USM, i.e. the increment in joint angle increases towards the back. In addition, this growth rate can be adjusted by varying the parameter α. By increasing α, the angle of the front joints is reduced, moving the joint motion towards the back of the body, similarly to the motion of fish using their tail. If α is increased so much that motion is restricted almost solely to the backmost joint, it will act more similarly to the rudder of a traditional marine vehicle.

By keeping a greater portion of the body entirely or nearly straight, the orientation of the head will change less due to joint motion, and will instead be kept more steady throughout the manoeuvring. In addition, the thruster configuration of the USM will change less, at least that of the thrusters placed on the front links in this case. Depending on the placement and direction of thrusters, this could help avoid singular thrust configurations.

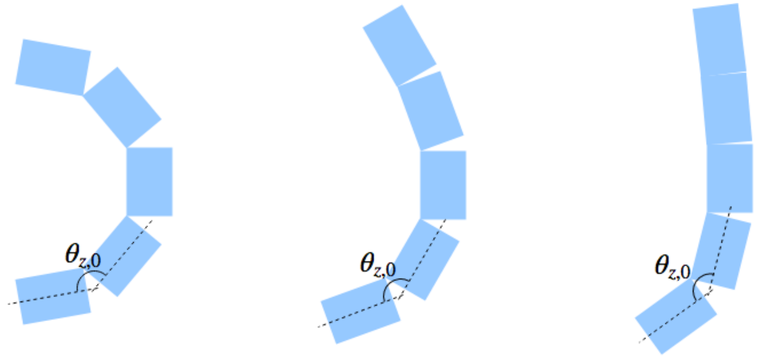

(a) Uniform curvature, g_1 (b) Linear curvature, g_2 (c) Exponential curvature, g_3 with $\alpha = 1$

Figure 5.2: Body shapes formed by the scaling functions (5.12), seen from above. All shapes have the same base angle $\theta_{z,0}$.

Base angle saturation

Since the control law (5.9) uses an angle-axis parametrisation of the error from desired attitude, it will always result in turning the USM along the shortest path, i.e. the USM will never be required to turn more than 180°. It is therefore not necessary for it to curve any more than into a U-shape, where the x-axes of the base link frame and end-effector frame point in opposite directions.

The base angle $\theta_{0,180}$ which leads to the head and tail pointing opposite for a shape given by a scaling function $g(i)$ can be found as

$$\theta_{0,180} = \frac{\pi}{\sum_{i=1}^{m} g(i)} \tag{5.13}$$

In the case of shapes where the front joints are used sparingly, like the exponential curve with high values of α, the angle given by (5.13) can be larger than what is physically possible to achieve for the joints of a given USM. If some of the joints reach their limits, the shapes with increasing joint angle towards the tail end will become deformed.

The maximum allowable base angle $\theta_{0,\max}$ is therefore set to

$$\theta_{0,\max} = \min\left(\theta_{0,180}, \theta_{\max}\right) \tag{5.14}$$

where $\theta_{\max}$ is the maximum achievable joint angle. For the USM used in later simulations, this angle is $\pm 90°$ [45].

5.3.3 Joint control

The joints will be controlled using the control input

$$\boldsymbol{\tau} = -k_{\theta,P}(\boldsymbol{\theta} - \boldsymbol{\theta}^*) - k_{\theta,D}\dot{\boldsymbol{\theta}} + \mathbf{g}_\theta \tag{5.15}$$

where the elements of $\boldsymbol{\theta}^*$ are the references (5.10) placed at their appropriate positions. The first two terms of the input torque (5.15) constitute a PD-controller. The last term $\mathbf{g}_\theta$ denotes the part of the generalised hydrostatic force $\mathbf{g}(\boldsymbol{\eta}, \boldsymbol{\theta})$ given in (4.21) which influences the joints. The term is added for the purpose of compensating for the moments acting on the joints due to hydrostatic restoring forces acting on the links which the joints connect.

If the CM of each individual link is located below the CB, the forces of gravity and buoyancy will create a restoring moment which will always turn the link back into its hydrostatic equilibrium [13]. When the links are connected to each other by joints, the restoring moments on a link will also cause a moment acting on the adjacent joints.

Joint motion which would bring links out of their hydrostatic equilibrium is therefore counteracted. If the joints are controlled using PD-control alone, joint angles in the vertical plane will stabilise at an offset from a desired constant setpoint, in the position where the proportional action of the controller is equal to the hydrostatic moment.

The PD-controller part of (5.15) does not take into consideration the derivative of the reference signal, treating the reference as a simple setpoint, rather than a time-varying reference. This is motivated by the aim to avoid differentiation of the reference $\boldsymbol{\theta}^*$ as given by (5.10), which is saturated in order to preserve the body shape. In the instants when the base angle reaches its saturation, its derivative will be discontinuous.

5.4 Velocity control and thrust allocation

The forward velocity of the USM will be controlled using its thrusters. The simplest way of achieving this is to apply the same forward thrust to all available longitudinal thrusters to achieve the desired forward velocity.

If the USM possesses multiple longitudinal thrusters, rather than applying the same thrust to all, their locations can be exploited to help turn the USM, or reduce the sway and heave velocities of the end-effector. In particular, if two longitudinal thrusters are placed on each side of the same link, by applying different thrust to each of them, the USM can be turned, at least in the plane in which the two thrusters are mounted. In order to distribute control effort among multiple thrusters, a thrust allocation algorithm is needed.

Section 5.4.1 first presents the simple controller for control of surge by applying the same thrust to all longitudinal thrusters. Then, Section 5.4.2 presents the thrust allocation algorithm used in [45]. This algorithm will be used to distribute the control effort between the available longitudinal thrusters, or all the thrusters the USM possesses, in order to later compare the performance of the path-following method both with and without additional support from lateral thrusters.

All the methods presented in this section can be used for controlling either the forward velocity of the end-effector, or the base link, reminiscent of pulling or pushing the USM at the desired speed. In addition, when thrust allocation is used to exert a certain desired force on the USM, this force can also be found either with respect to the base or the end-effector. In total, this gives four different control modes for the thrust allocation methods.

5.4.1 Simple control of surge

For the case of controlling just the forward velocity, the input from longitudinal thrusters will be calculated using a simple PI-controller for the surge velocity, and the input from all transverse thrusters i set to zero.

The elements u_i of the thrust input $\mathbf{u}$ in (4.14b) are set to be

$$u_i = \begin{cases} -k_{1,P}(u - u_d) - k_{1,I} \displaystyle\int_0^t u(\tau) - u_d \, \mathrm{d}\tau, & \text{if } \boldsymbol{\beta}_{t,i} = \mathbf{e}_1 \\ 0, & \text{otherwise.} \end{cases} \tag{5.16}$$

where $\boldsymbol{\beta}_{t,i}$ is the direction of thrust of thruster number i. The velocity u can denote the surge velocity of either base link or end-effector, depending on which is to be controlled.

5.4.2 Thrust allocation

The thruster configuration of a USM will vary depending on its current shape. In some joint configurations it may become singular, meaning that the thrusters are aligned in such a way that it is not possible to control some DOFs of the USM. When close to such configurations, thruster commands would be very high to compensate for the fact the thrusters have nearly no influence on one or more of the DOFs. To counteract this, a thrust allocation algorithm is used in [45] which solves the optimisation problem

$$\min_{\mathbf{u}} \left(\lambda^2 \|\mathbf{u}\|^2 + \|\mathbf{B}_\nu(\boldsymbol{\theta})\mathbf{u} - \boldsymbol{\tau}_c\| \right) \tag{5.17}$$

where λ is a damping factor which adjusts the weighting and therefore priority of keeping the thruster forces small, compared to trying to produce the desired forces and moments $\boldsymbol{\tau}_c$. The matrix $\mathbf{B}_\nu(\boldsymbol{\theta})$ consists of the first six rows of the full thruster configuration matrix $\mathbf{B}(\boldsymbol{\theta})$ as given by (4.24), i.e. the part which describes the forces and moments from the thrusters on the base link.

By letting the thrust be determined by the minimisation problem (5.17), meeting the exact command $\boldsymbol{\tau}_c$ is weighted against keeping the thruster forces low. By choosing the damping factor λ small, the minimisation of thruster effort is given lower priority. The explicit solution to (5.17) is given in [45] as

$$\mathbf{u} = \mathbf{B}_\nu^\dagger(\boldsymbol{\theta})\boldsymbol{\tau}_c, \quad \mathbf{B}_\nu^\dagger(\boldsymbol{\theta}) = \mathbf{B}_\nu(\boldsymbol{\theta})^\top \left(\mathbf{B}_\nu(\boldsymbol{\theta})\mathbf{B}_\nu(\boldsymbol{\theta})^\top + \lambda^2 \mathbf{I}_6 \right)^{-1} \tag{5.18}$$

The matrix $\mathbf{B}_\nu^\dagger(\boldsymbol{\theta})$ is called the damped pseudoinverse of $\mathbf{B}_\nu(\boldsymbol{\theta})$.

The desired forces and moments will be found using a simplified version of the controller in [45], which gives

$$\boldsymbol{\tau}_c = \mathbf{M}_{11}(\boldsymbol{\theta})\mathbf{a}_c \tag{5.19}$$

where $\mathbf{M}_{11}(\boldsymbol{\theta})$ is the upper-left 6×6 block of the mass matrix $\mathbf{M}(\boldsymbol{\theta})$, (4.15), and $\mathbf{a}_c$ is the desired acceleration of the base link, given in the base frame. The acceleration $\mathbf{a}_c$ can be written as $\mathbf{a}_c = [\mathbf{a}_{c,\text{lin}}^\top \quad \mathbf{a}_{c,\text{ang}}^\top]^\top$, where $\mathbf{a}_{c,\text{lin}}, \mathbf{a}_{c,\text{ang}} \in \mathbb{R}^3$ are the desired linear and angular accelerations, respectively.

The desired linear acceleration is chosen such that it controls surge to its desired value u_d and helps reduce sway and heave velocities, by choosing it to be

$$\mathbf{a}_{c,\text{lin}} = -\mathbf{K}_{\text{lin},P}\left(\mathbf{v} - \begin{bmatrix} u_d \\ 0 \\ 0 \end{bmatrix}\right) - \left(k_{1,I}\int_0^t u(\tau) - u_d \,\mathrm{d}\tau\right)\mathbf{e}_1 \tag{5.20}$$

where $\mathbf{K}_{\text{lin},P}$ is a diagonal matrix consisting of positive gain parameters, and $\mathbf{v} = [u,\ v,\ w]^\top$ can be the velocity of either the base or the end-effector, given in the corresponding frame.

The desired angular acceleration is chosen to help with turning the USM. Unlike the linear velocity, the orientation and angular velocity of the end-effector is always used, as the orientation and angular velocity of the base link can be very different due to the joint angles and motion. The desired angular acceleration $\mathbf{a}_c$ consists of the same terms as the base angles (5.9), but not necessarily with the same choice of control parameters. This results in

$$\begin{aligned}\mathbf{a}_{c,\text{ang}} = \begin{bmatrix} 0 & 0 & 0 \\ 0 & 1 & 0 \\ 0 & 0 & 1 \end{bmatrix}\Bigg(& -k_{\text{ang},P}\frac{\tilde{\theta}}{\sin\tilde{\theta}}\left(\mathbf{x}_{\text{ref}}^b \times \mathbf{e}_1\right) \\ & - k_{\text{ang},D}\left(\boldsymbol{\omega}^b - \tilde{\mathbf{R}}\boldsymbol{\omega}_{\text{ref}}^b\right) + \tilde{\mathbf{R}}\mathbf{R}_i^b\left(\mathbf{x}_{\text{ref}}^i \times \ddot{\mathbf{x}}_{\text{ref}}^i\right)\Bigg)\end{aligned} \tag{5.21}$$

Thrust allocation among longitudinal thrusters

In order to exploit the presence of multiple longitudinal thrusters, the thrust allocation method (5.18) must be used with a thrust configuration matrix which only takes into account contribution from the longitudinal thrusters. This matrix can be found as

$$\mathbf{B}_{\mathrm{lon}}(\boldsymbol{\theta}) = \mathbf{B}(\boldsymbol{\theta})\mathbf{T} \tag{5.22}$$

where $\mathbf{T}$ is a diagonal matrix with elements $T_{ii} = 1$ if $\boldsymbol{\beta}_{t,i} = \mathbf{e}_1$, and 0 otherwise. Replacing $\mathbf{B}(\boldsymbol{\theta})$ with $\mathbf{B}_{\mathrm{lon}}(\boldsymbol{\theta})$ in the expression (5.18) gives the thrust input resulting as closely as possible in the force $\boldsymbol{\tau}_c$, but using only the longitudinal thrusters.

Control with respect to the end-effector

The thrust allocation (5.18) relies on the thrust allocation matrix $\mathbf{B}(\boldsymbol{\theta})$, and the mass matrix $\mathbf{M}(\boldsymbol{\theta})$ for finding the desired force. These matrices give forces and moments on the base frame for which the dynamics (4.14b) are formulated.

In order to find the desired forces and thrust configuration matrix with respect to the end-effector instead, the matrices $\mathbf{M}(\boldsymbol{\theta})$ (4.15) and $\mathbf{B}(\theta)$ must be recomputed with the Jacobian matrices found in Section 4.3.

Chapter 6

Simulations

In this chapter, simulation results of the guidance and control developed in Chapter 5 are presented. Characteristics of the USM model used, as well as choice of control parameters are given in Section 6.1. Section 6.2 presents simulations comparing the performance of the different shapes proposed in Section 5.3.2 for direction control. Simulation results with larger initial attitude errors are shown in Section 6.3, including the case of pointing exactly opposite to the reference. Section 6.4 shows simulation results when the joints are controlled using limited input torques, or without compensating for the hydrostatic moments acting upon them. Finally, Section 6.5 shows simulation results where thrusters are contributing to the control of direction, both the case of using all available thrusters, and the case of thrust allocation among only the longitudinal thrusters.

Additional simulation results, of a USM subject to disproportionately large rigid body inertia and hydrostatic forces, are shown in Appendix E.

6.1 Model and control parameters

6.1.1 USM model

The USM model used in the simulations presented in this chapter is based on a USM with 5 links and 4 cardan joints between them, i.e. joints which can be rotated about both the y- and z-axis of the frame of the link to which they are attached. These joints are modeled as consecutive 1 DOF-joints, and consequently the simulation model consists of 9 links, where every even-numbered link is a short link separating two joints actuated about different axes. Odd-numbered joints rotate about the z-axis, and even-numbered about the y-axis. All links are neutrally buoyant, and passively stabilised with CM located below CB.

The physical parameters of the USM, including link mass, size, and thruster positions, are given in Appendix C. The USM possesses 7 thrusters in total, positioned as shown in Figure 6.1.

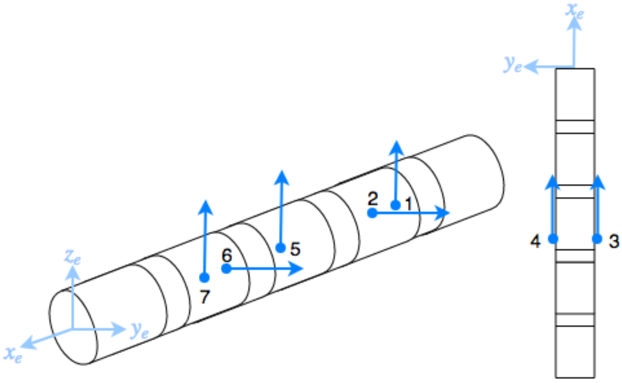

Figure 6.1: Thrust direction and placement of the thrusters of the USM model used in the simulations. Placements are not exact. The end-effector frame is shown for reference, its axes denoted x_e, y_e, z_e.

6.1.2 Control parameters

All simulations are performed with the same parameters for the guidance law, direction control and joint controller, given in Table 6.1. The control parameters for thruster control, both the PI-controller and the thrust allocation methods, are given in Table 6.2.

The gains k_P and k_D were found by trial and error, and the choice in Table 6.1 was found to give an acceptable performance for a wider range of combinations of body curvature and initial conditions.

Table 6.1: Parameters for guidance, direction control and joint control.

u_d	k_e	k_P	k_D	$k_{\theta,P}$	$k_{\theta,D}$
0.5	$\frac{u_d}{15}$	2	3	30	50

Table 6.2: Control parameters of the thruster controllers; the PI-controller for surge, and thrust allocation using all thrusters, or longitudinal only.

	PI-control of surge	Thrust allocation
$\mathbf{K}_{\text{lin},P}/k_{u,P}$	100	diag(0.2, 0.1, 0.1)
$k_{u,I}$	5	0.01
$k_{\text{ang},P}$	-	0.2
$k_{\text{ang},D}$	-	1
λ	-	0.02 height

6.2 Different body shapes for direction control

Simulation results of path-following using the three proposed shapes are shown in Figures 6.2-6.9. The shapes considered are the uniform, linear and exponential body curvatures presented in Section 5.3.2, and with several different values of the parameter α for the exponential curvature (5.12c). The surge of the end-effector is controlled using the basic PI-controller (5.16).

The USM starts in a straight configuration with all joints outstretched, with its base at position $[0,\ 10,\ -5]^\top$, and pointing parallel to the path.

The scaling factors for the reference angle of each joint due to the different choices of scaling functions $g(i)$ in (5.12) are given in Table 6.3. Joints 1 and 2 always have the base angle as reference. Joints 3 and 4, 5 and 6 and 7 and 8 have pairwise the same scaling factor, since they have the same index among joints rotating about the same axis.

Figures 6.2 and 6.3 show the results of exponential curvature with different values of α. In Figures 6.4 and 6.5, simulation results from using the uniform

Table 6.3: Scaling factors of joint references to form different body shapes.

	Joints 3 & 4	Joints 5 & 6	Joints 7 & 8
$g_1(i)$, uniform curvature	1	1	1
$g_2(i)$, linear curvature	0.75	0.5	0.25
$g_3(i)$, $\alpha = 0.1$	0.90	0.82	0.74
$g_3(i)$, $\alpha = 0.3$	0.74	0.55	0.41
$g_3(i)$, $\alpha = 0.5$	0.61	0.37	0.22
$g_3(i)$, $\alpha = 0.7$	0.50	0.25	0.12
$g_3(i)$, $\alpha = 1$	0.37	0.14	0.05
$g_3(i)$, $\alpha = 1.5$	0.22	0.05	0.01

and linear curvatures are shown together with the exponential curvature with two selected values of α. Figure 6.6 shows a closer view of the the cross-track error along the y-axis from the previous two sets of simulations. More details from the simulations of the uniform and linear shapes are shown in Figures 6.7-6.9.

The simulations show that the USM does not quite follow the path. In the horizontal plane, it oscillates about the path, while in the vertical plane, its convergence towards the path is slow, and the USM appears to approach a stationary offset from the depth at which the path lies. This offset is fairly small, however, at less than 0.5 m, as seen in e.g. Figure 6.4b. Figure 6.6b shows that the oscillations about the path in the horizontal plane are within ±0.5 m.

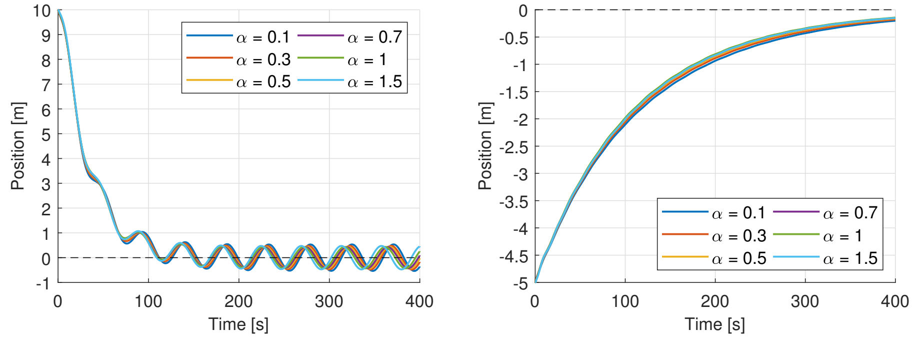

(a) Cross-track error along y-axis (b) Cross-track error along z-axis

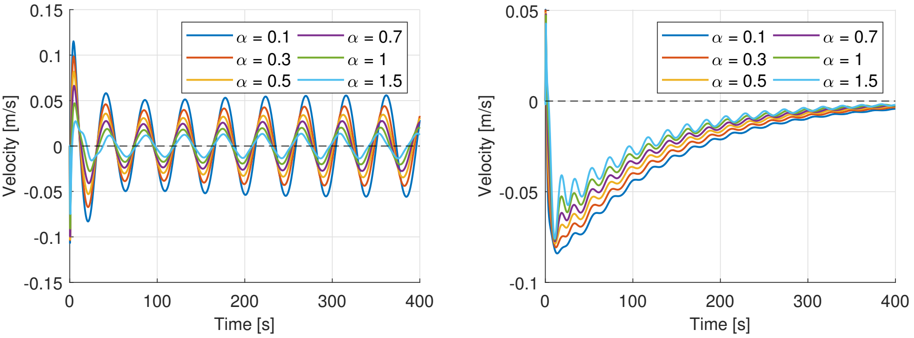

(c) End-effector sway velocity (d) End-effector heave velocity

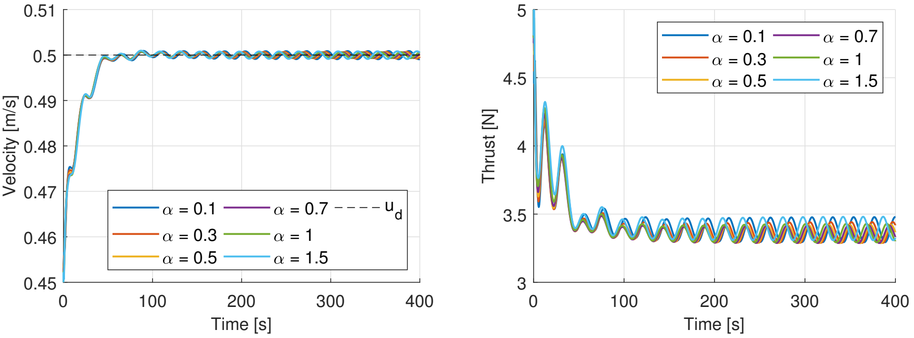

(e) End-effector surge velocity (f) Thruster force

Figure 6.2: Simulation results of path-following with varying exponential body curvature.

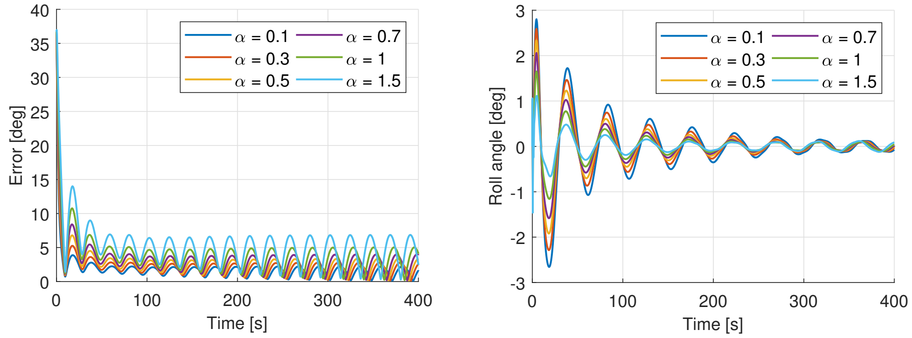

(a) Total error angle $\tilde{\phi}$ (b) Roll of end-effector frame

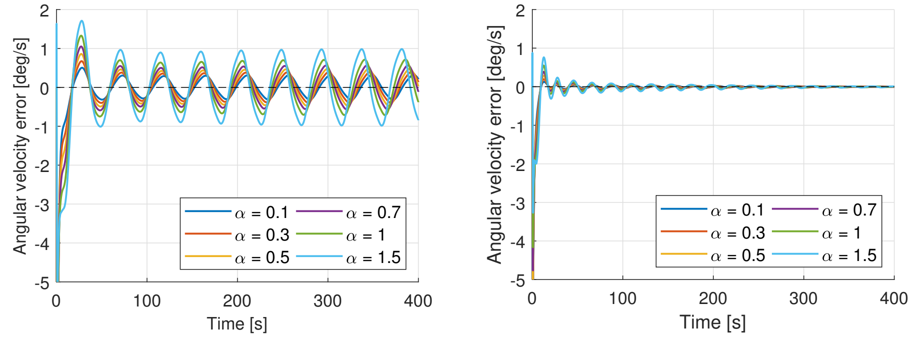

(c) $\tilde{\boldsymbol{\omega}}^e$ about z-axis (d) $\tilde{\boldsymbol{\omega}}^e$ about y-axis

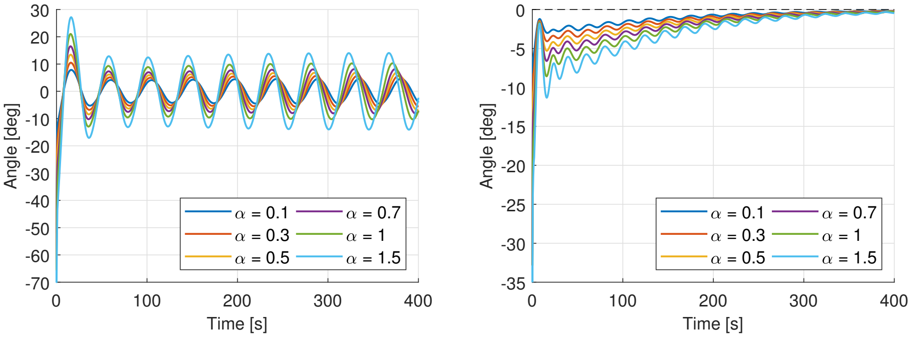

(e) Base angle $\theta_{z,0}$ (f) Base angle $\theta_{y,0}$

Figure 6.3: Simulation results of path-following with varying exponential body curvature, continued.

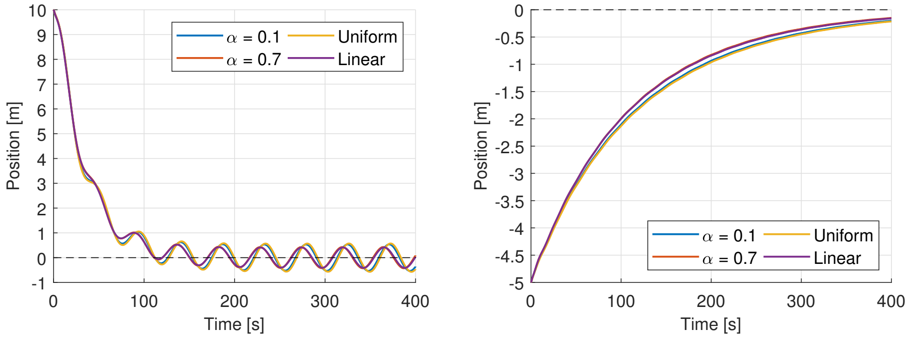

(a) Cross-track error along y-axis (b) Cross-track error along z-axis

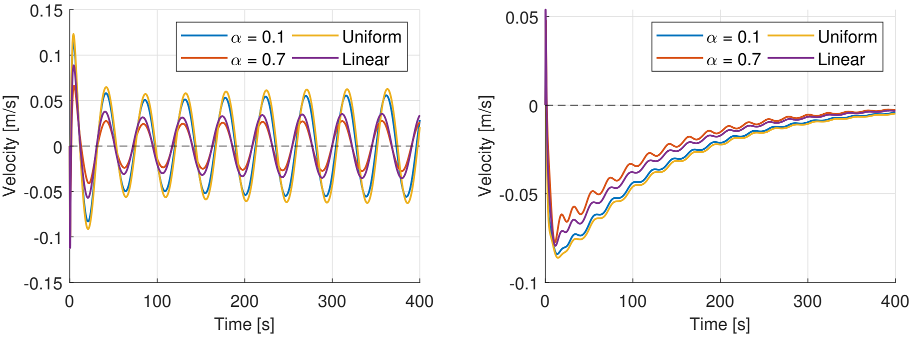

(c) End-effector sway velocity (d) End-effector heave velocity

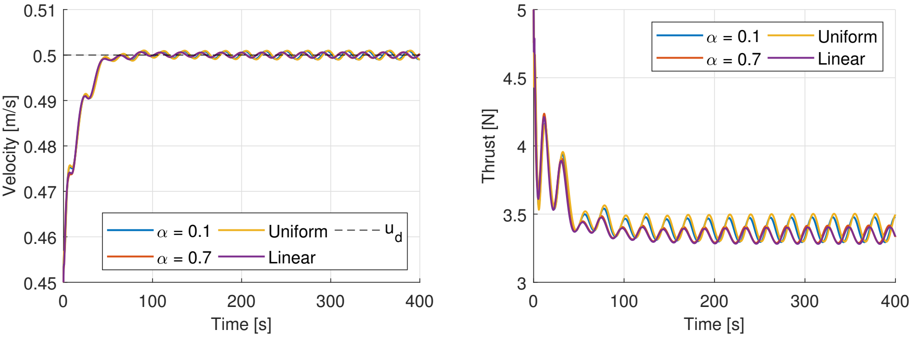

(e) End-effector surge velocity (f) Thruster force

Figure 6.4: Simulation results of path-following with uniform, linear and exponential body curvature.

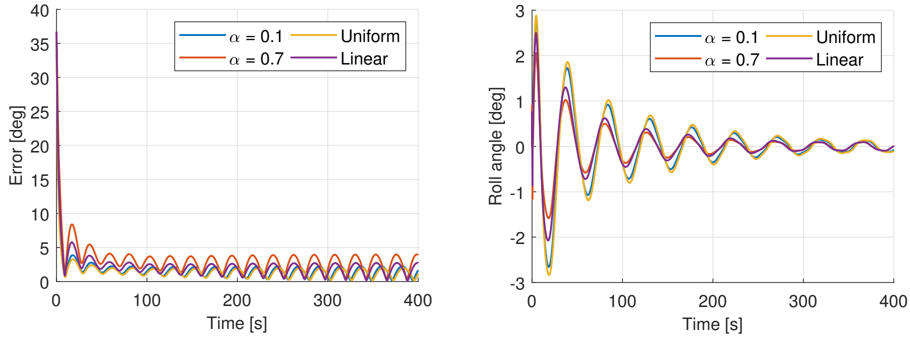

(a) Total error angle $\tilde{\phi}$ (b) End-effector frame roll

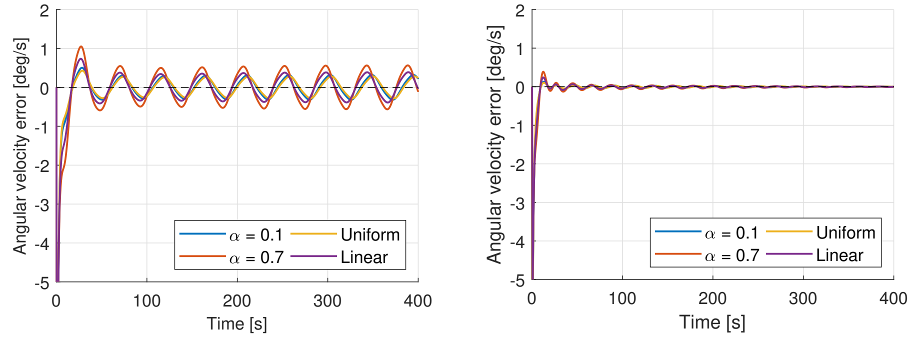

(c) $\tilde{\boldsymbol{\omega}}^e$ about z-axis (d) $\tilde{\boldsymbol{\omega}}^e$ about y-axis

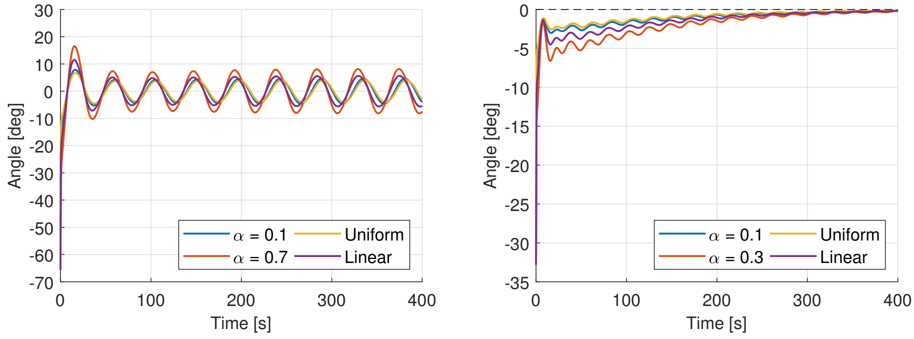

(e) Base angle $\theta_{z,0}$ (f) Base angle $\theta_{y,0}$

Figure 6.5: Simulation results of path-following with uniform, linear and exponential body curvature, continued.

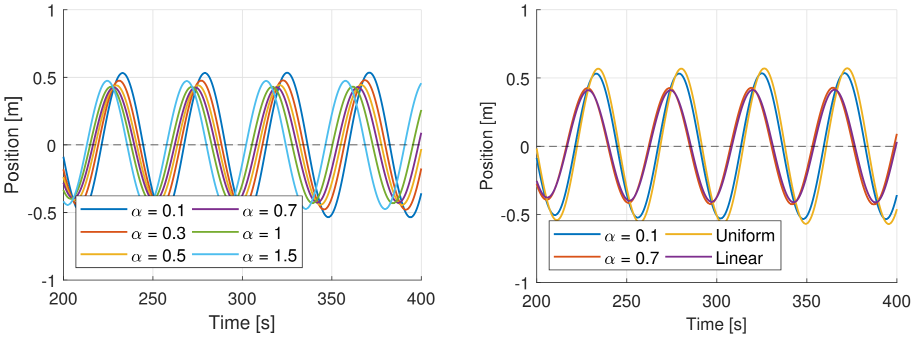

(a) Close-up of Figure 6.2a

(b) Close-up of Figure 6.4a

Figure 6.6: Close-ups of cross-track error comparisons along y-axis

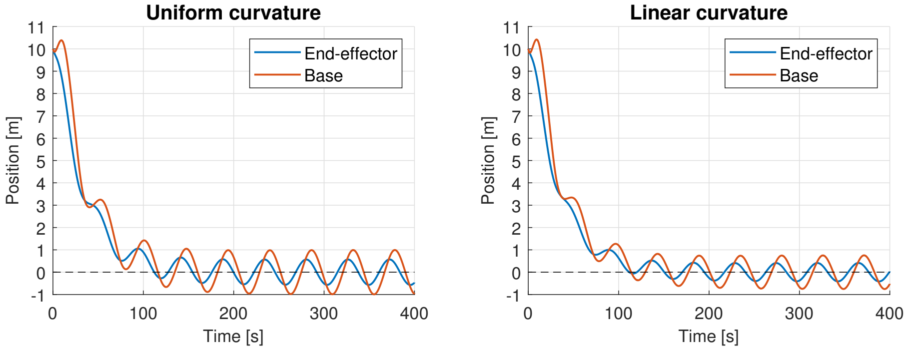

(a) Cross-track error along y-axis

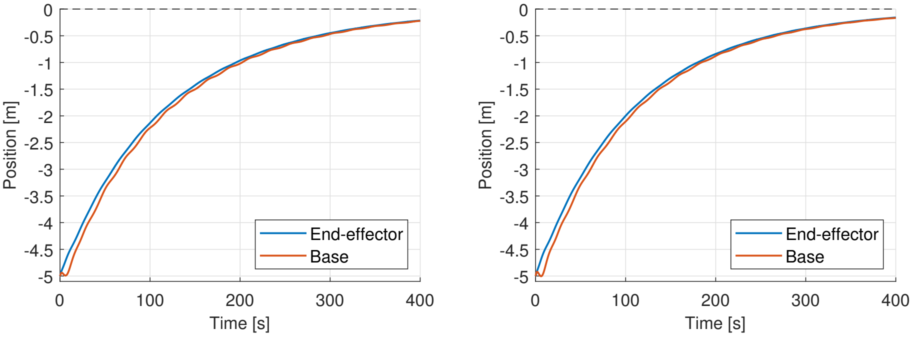

(b) Cross-track error along z-axis

Figure 6.7: Simulation results of path-following with uniform and linear body curvature. End-effector and base positions.

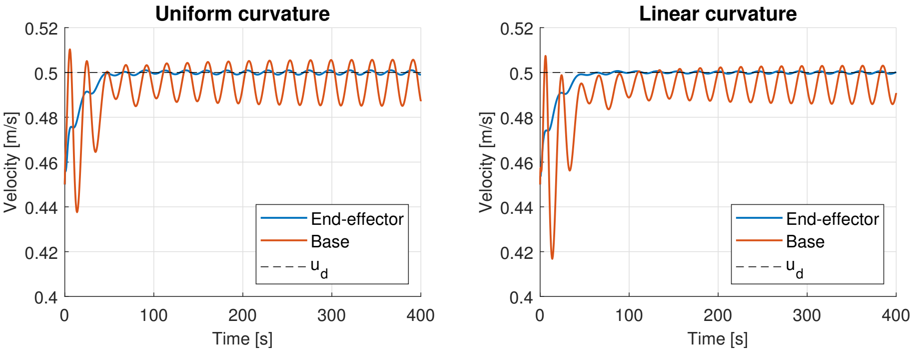

(a) Surge velocity

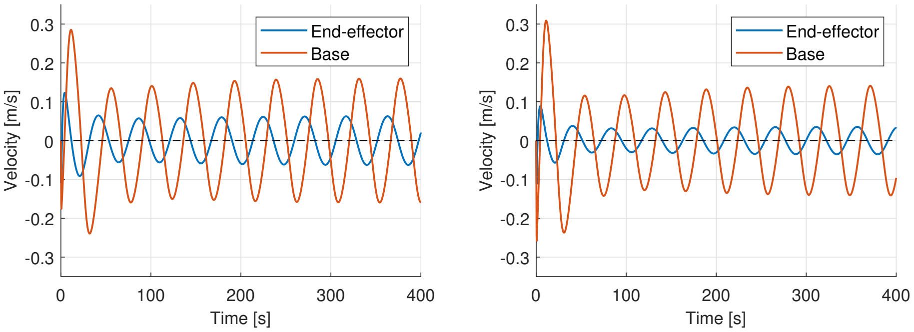

(b) Sway velocity

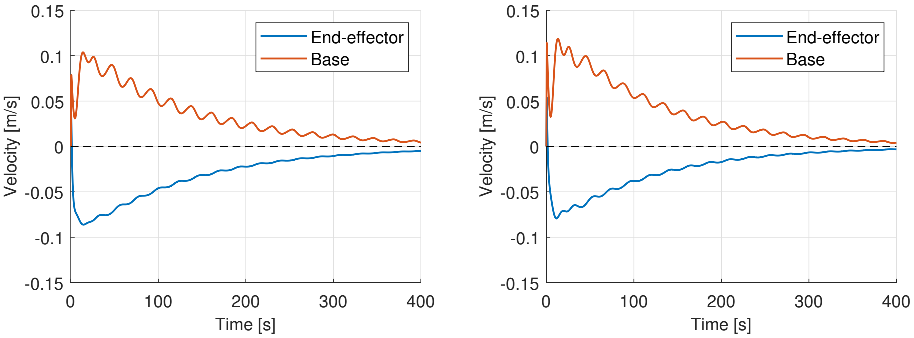

(c) Heave velocity

Figure 6.8: Simulation results of path-following with uniform and linear body curvature, velocities.

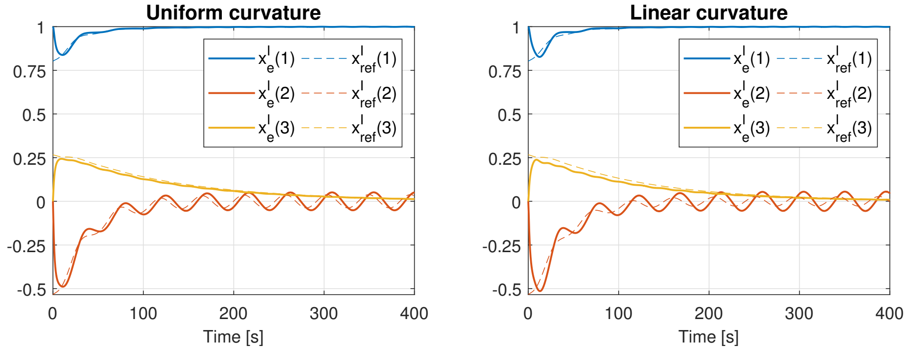

(a) Inertial-frame representation of the end-effector pointing direction

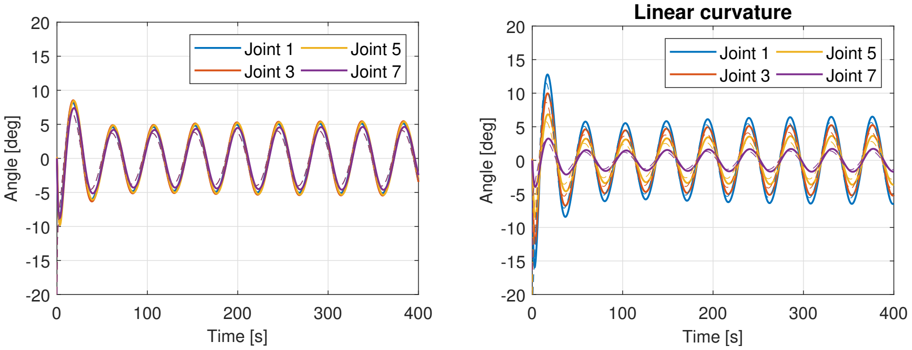

(b) Joint angles of joints rotating about z-axis

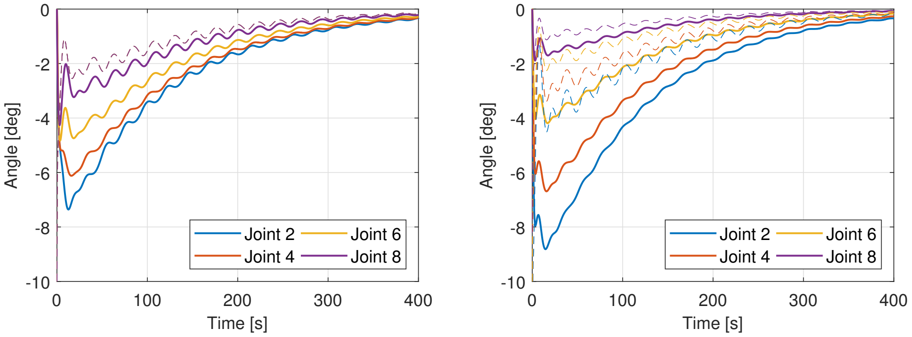

(c) Joint angles of joints rotating about y-axis

Figure 6.9: Simulation results of path-following with uniform and linear body curvature. End-effector pointing direction and joint angles, with references in dashed lines.

6.3 Large initial angle errors

The following Figures 6.10-6.13 show simulation results when the initial angle away from desired pointing direction is larger. Figures 6.10 and 6.11 show simulation results using the uniform, linear and exponential curvatures, the last with $\alpha = 1.5$. The USM starts with its base again at position $[0,\ 10,\ -5]^\top$, but is now rotated 90° about the z-axis, away from the path. This puts the initial position of the end-effector at $[0,\ 13.3,\ -5]^\top$.

In Figures 6.12 and 6.13, the USM starts on the path, but pointed and with forward velocity in the opposite direction.

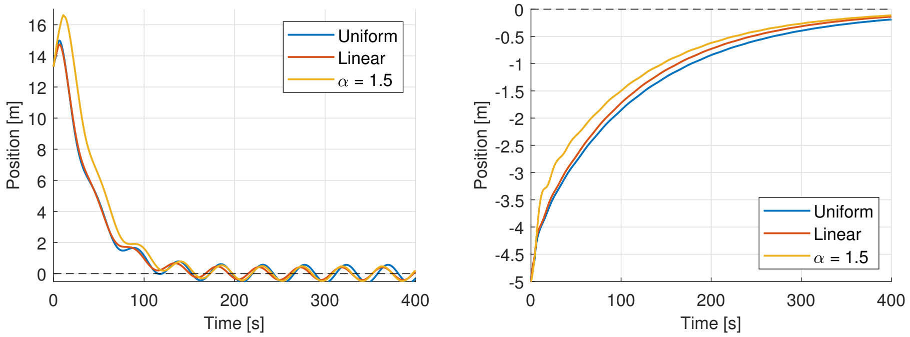

(a) Cross-track error along y-axis (b) Cross-track error along z-axis

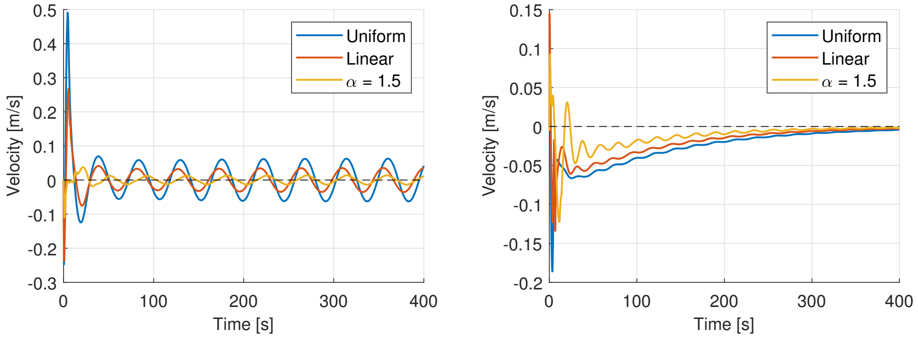

(c) End-effector sway velocity (d) End-effector heave velocity

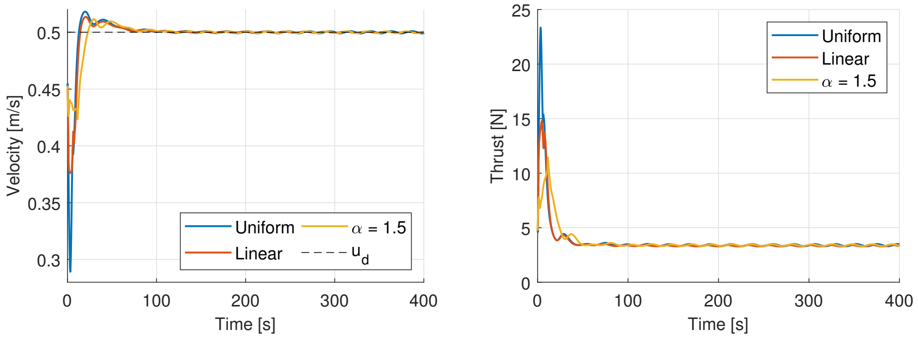

(e) End-effector surge velocity (f) Thruster force

Figure 6.10: Simulation results with the USM starting pointing away from the path.

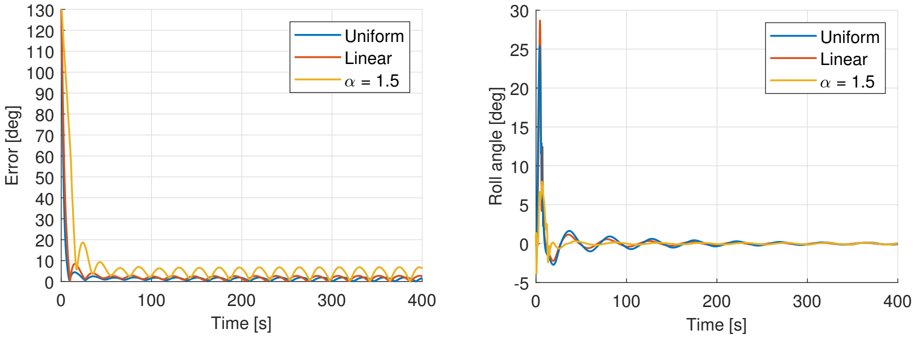

(a) Total error angle $\tilde{\phi}$ (b) Roll of end-effector frame

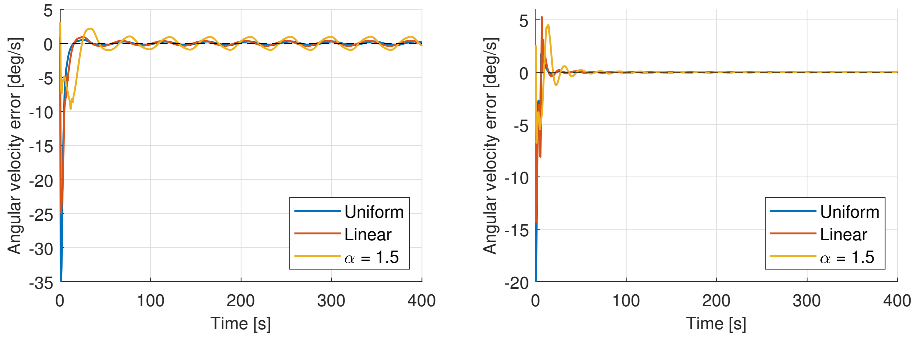

(c) $\tilde{\boldsymbol{\omega}}^e$ about z-axis (d) $\tilde{\boldsymbol{\omega}}^e$ about y-axis

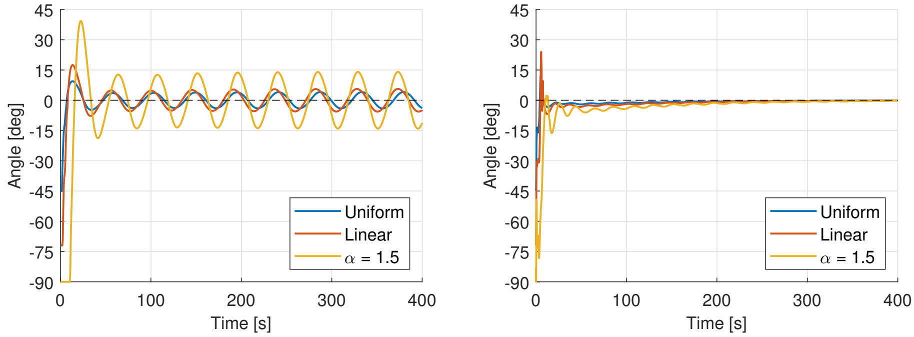

(e) Base angle $\theta_{z,0}$ (f) Base angle $\theta_{y,0}$

Figure 6.11: Simulation results with the USM starting pointing away from the path, continued.

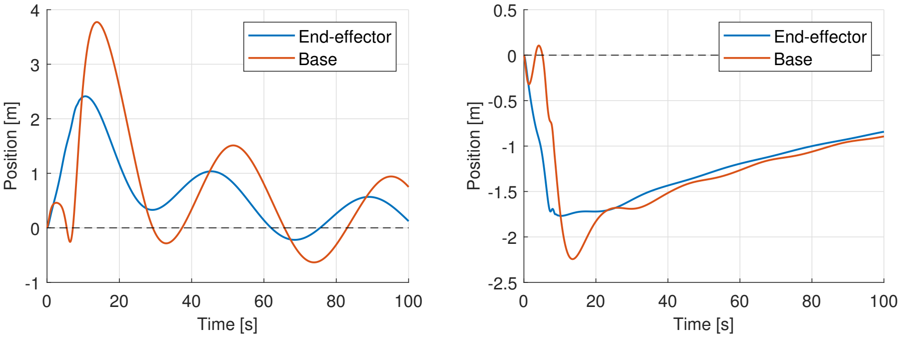

(a) Cross-track error along y-axis (b) Cross-track error along z-axis

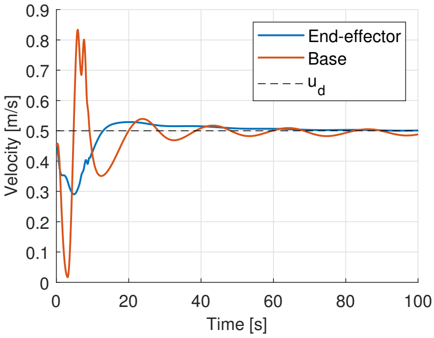

(c) Surge velocity

Figure 6.12: Simulation results of the USM starting on the path, pointing in the opposite direction.

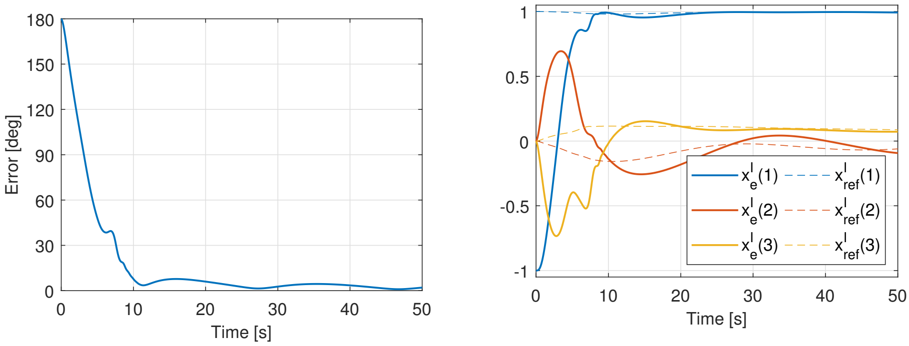

(a) Total error angle $\tilde{\phi}$

(b) Inertial-frame representation of end-effector x-axis

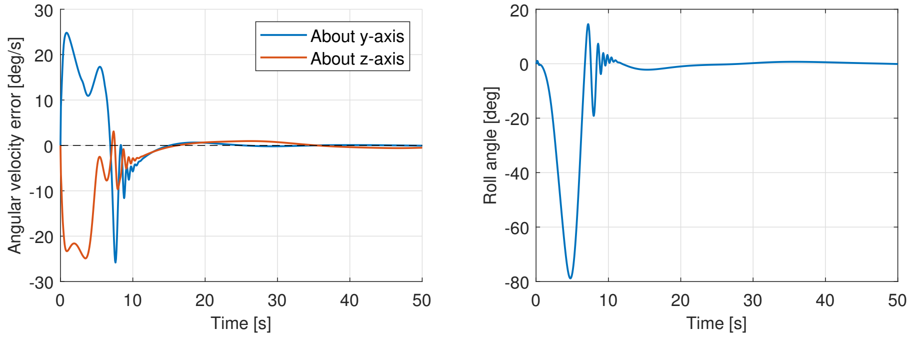

(c) Angular velocity tracking error $\tilde{\boldsymbol{\omega}}^e$

(d) Roll of end-effector frame

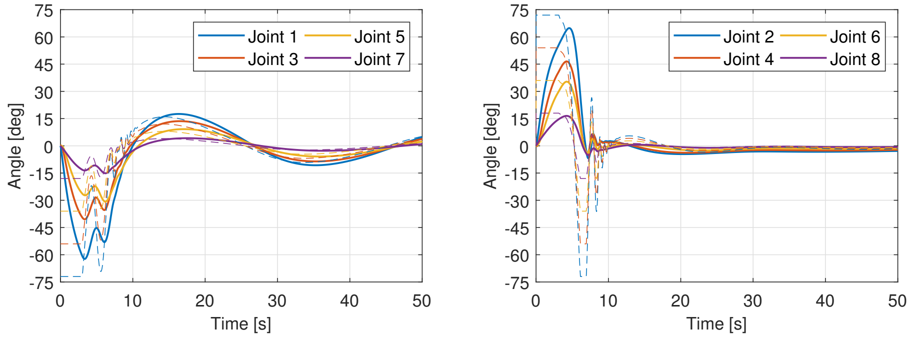

(e) Joints rotating about z-axis

(f) Joints rotating about y-axis

Figure 6.13: Simulation results of the USM starting on the path pointing in the opposite direction, continued.

6.4 Joint control

The physical USM on which the model used in these simulation is based has joint motors which can exert a maximum torque of magnitude 11 Nm. In the following simulations, the influence of saturation of the joint torque, as well as the hydrostatic compensation term in the joint controller (5.15), is examined. This gives four different modes of joint control, summarised in Table 6.4.

Figures 6.14 and 6.15 show simulation results of path-following using the four modes of joint control. The linear curvature is used, and the surge of the end-effector is controlled using the PI-controller. The USM starts pointing parallel to the path. Figure 6.14 shows the positions, pointing direction tracking error and heave velocity for the four modes. Since there is no observable difference in behaviour due to saturation of torques, and no visible difference in the motion in the horizontal plane for any of the modes, Figure 6.15 shows only the joint angles and torques of the joints rotating about the y-axis, and makes only the distinction between with and without hydrostatic compensation, rather than the full four modest.

Table 6.4: Joint control modes.

	Hydrostatic compensation	Saturation
Mode 1	Yes	No
Mode 2	No	No
Mode 3	Yes	Yes
Mode 4	No	Yes

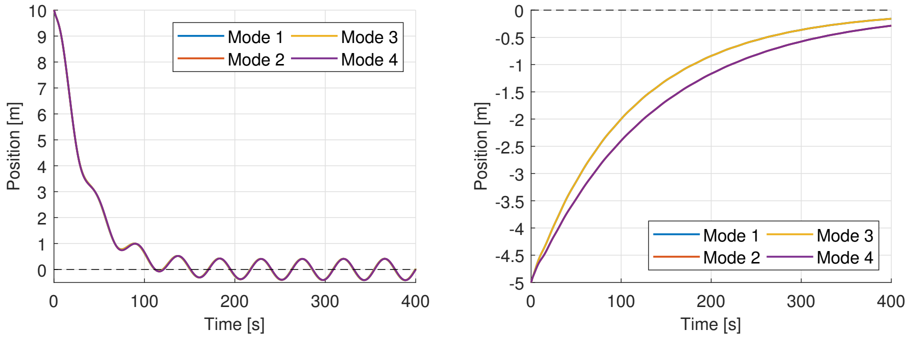

(a) Cross-track error of the end-effector along the y-axis

(b) Cross-track error of the end-effector along the z-axis

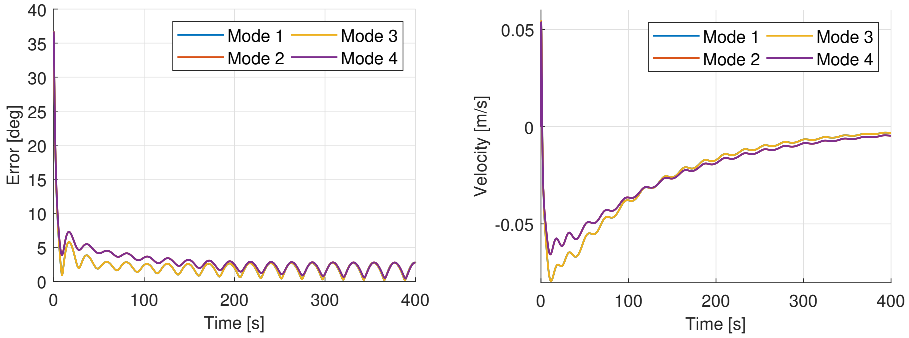

(c) Total pointing direction error angle $\tilde{\phi}$

(d) Heave velocity

Figure 6.14: Simulation results with and without hydrostatic compensation in joints and saturation of joint torques.

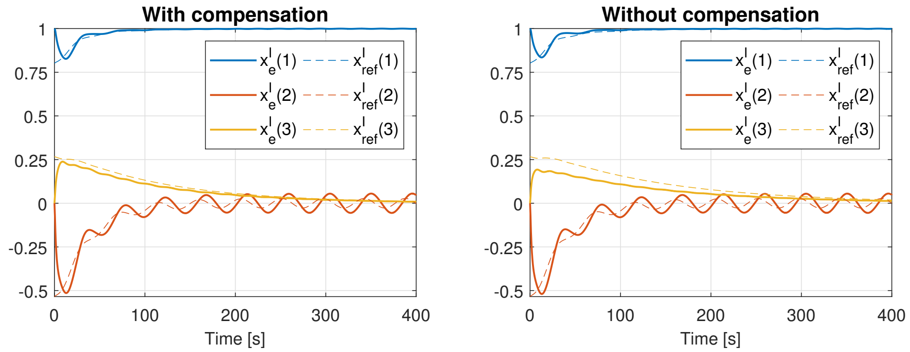

(a) End-effector pointing direction in the inertial frame

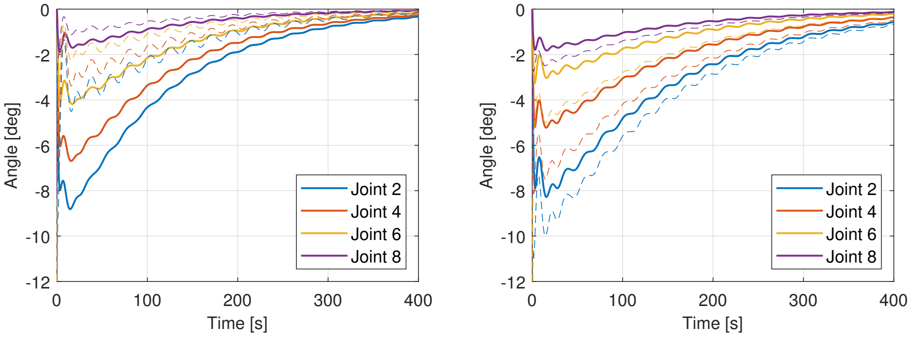

(b) Joint angles of joints rotating about y-axis, references in dashed lines

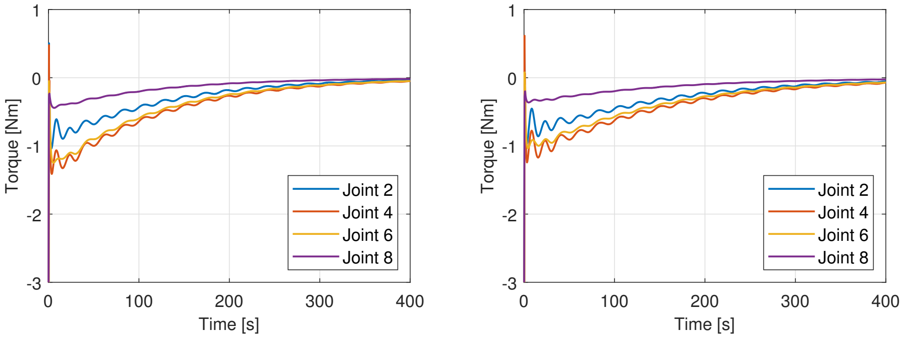

(c) Joint torques of joints rotating about y-axis

Figure 6.15: Simulation results with and without compensation for hydrostatic moments, without saturation of torque.

6.5 Thruster combinations

The thrust allocation method presented in Section 5.4 can be used with thrust and desired forces and moments calculated with respect to either the base or the end-effector of the USM. The desired acceleration can also be found using feedback from the velocity of either the base or the end-effector, changing which velocity is controlled. This gives four possible combinations for the thrust allocation, listed in Table 6.5.

Figures 6.16-6.23 show simulation results of the four combinations using all available thrusters. The use of thrusters is combined with the uniform curvature, due to difficulties in finding control parameters which would work with the linear curvature.

Figures 6.24-6.27 show simulation results of combinations 1 and 3 using only the longitudinal thrusters. Combination 2 was found to give results very similar to combination 3, while combination 4 gave oscillations similar to those observed in Section 6.2, when thrusters were used for forward propulsion only.

All simulation use control parameters as listed in Table 6.2.

Table 6.5: Thrust allocation combinations

	Control of velocity of	Control forces with respect to
Combination 1	End-effector	End-effector
Combination 2	Base	End-effector
Combination 3	End-effector	Base
Combination 4	Base	Base

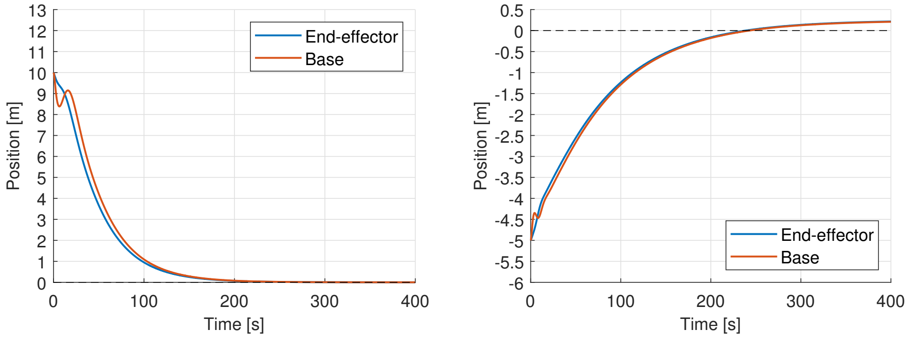

(a) Cross-track error along y-axis (b) Cross-track error along z-axis

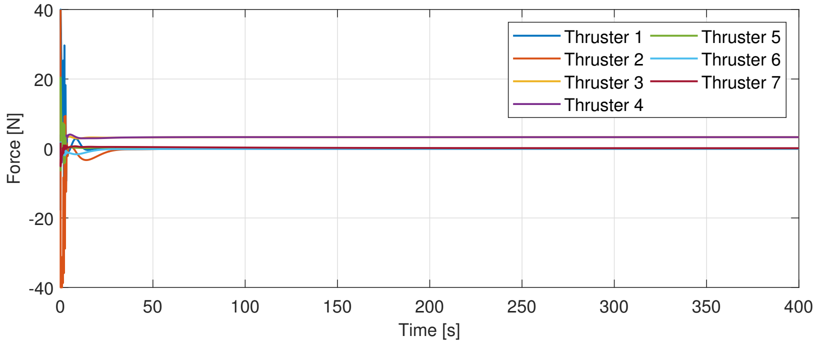

(c) Thruster forces

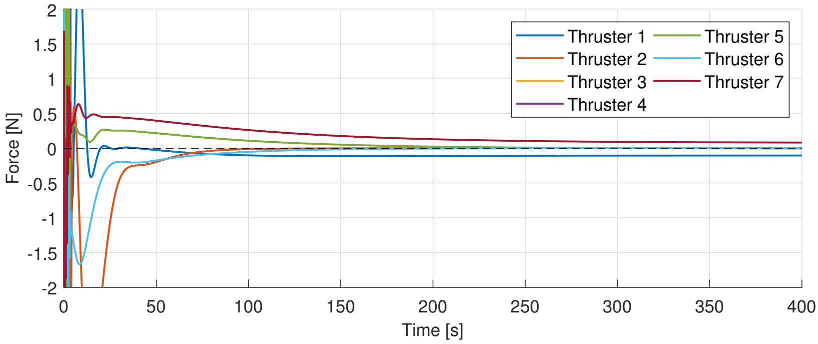

(d) Close-up of thruster forces

Figure 6.16: Simulation results using thrust allocation combination 1 with all thrusters. Cross-track errors and thrust.

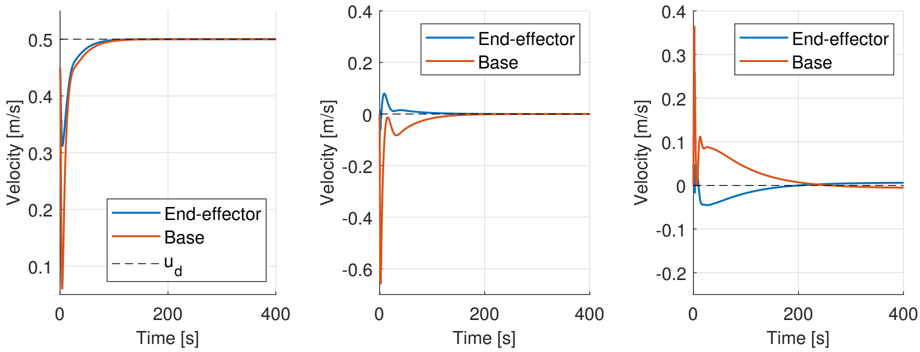

(a) Surge velocity (b) Sway velocity (c) Heave velocity

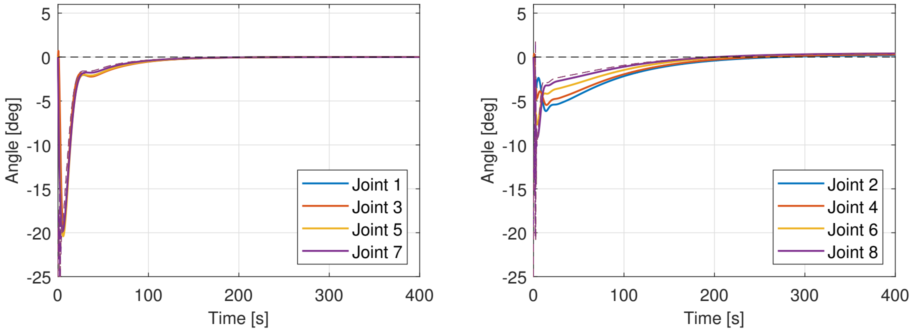

(d) Joint angles of joints rotation about z-axis, reference in dashed coloured line

(e) Joint angles of joints rotation about y-axis, reference in dashed coloured line

Figure 6.17: Simulation results using thrust allocation combination 1 with all thrusters. Velocities and joint angles.

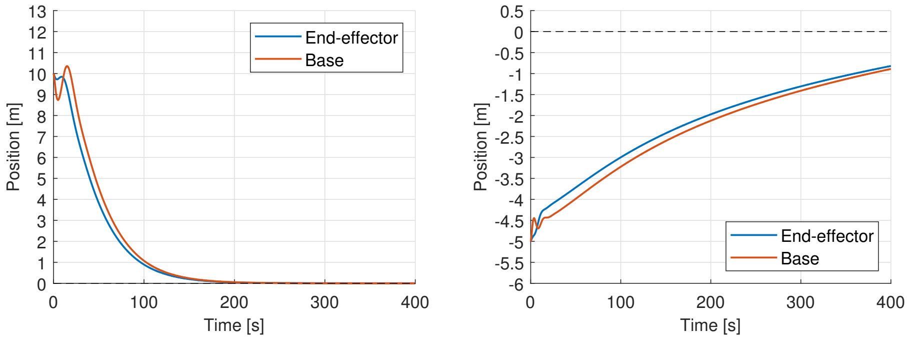

(a) Cross-track error along y-axis (b) Cross-track error along z-axis

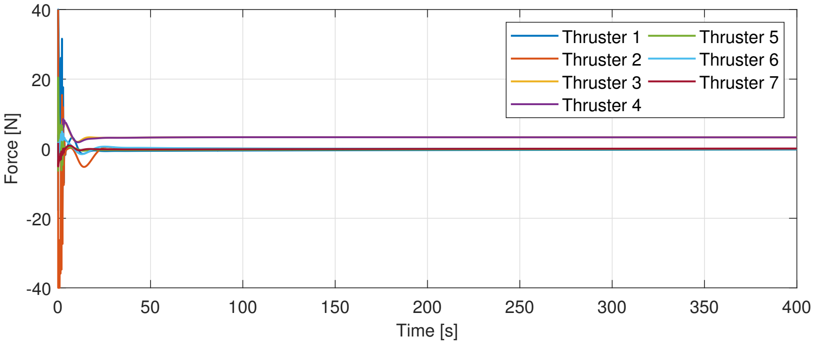

(c) Thruster forces

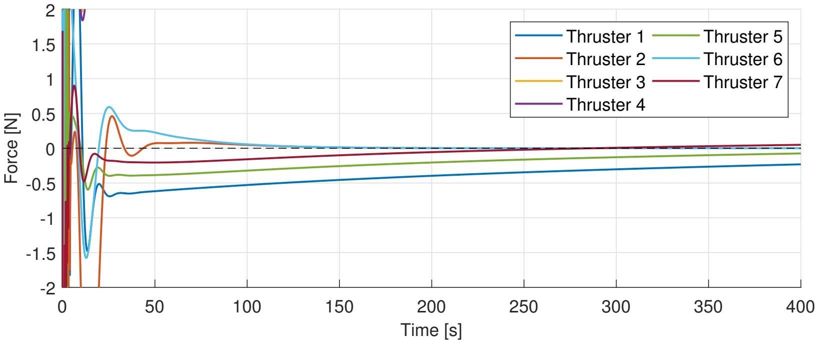

(d) Close-up of thruster forces

Figure 6.18: Simulation results using thrust allocation combination 2 with all thrusters. Cross-track errors and thrust.

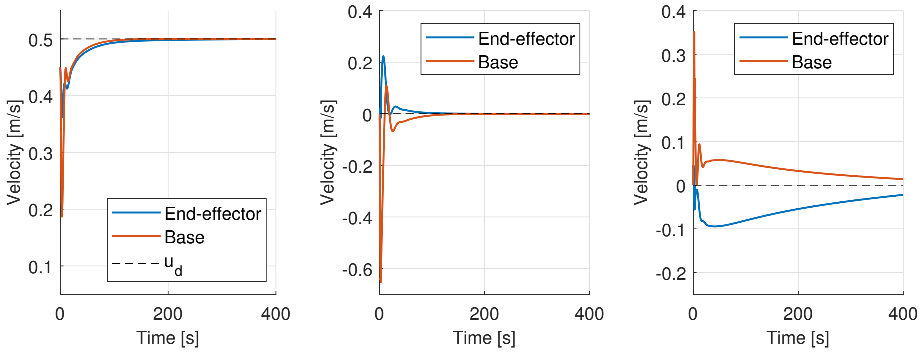

(a) Surge velocity (b) Sway velocity (c) Heave velocity

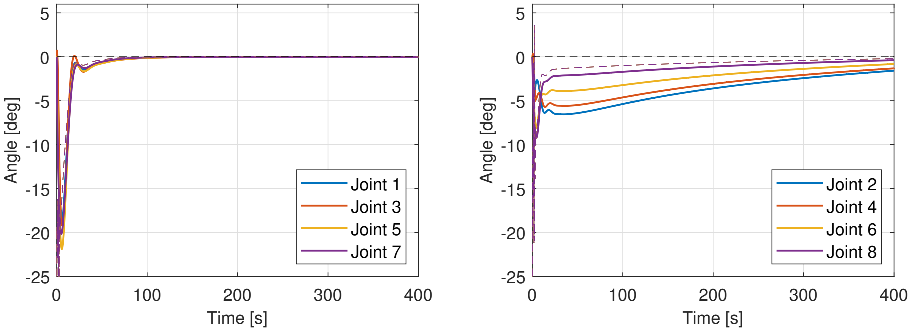

(d) Joint angles of joints rotation about z-axis, reference in dashed coloured line

(e) Joint angles of joints rotation about y-axis, reference in coloured dashed line

Figure 6.19: Simulation results using thrust allocation combination 2 with all thrusters. Velocities and joint angles.

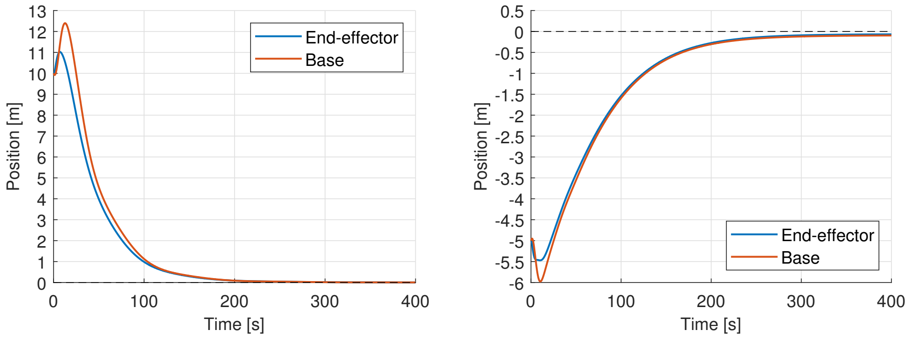

(a) Cross-track error along y-axis (b) Cross-track error along z-axis

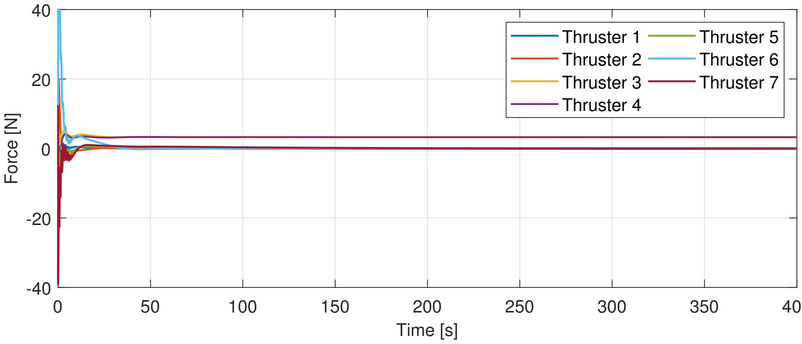

(c) Thruster forces

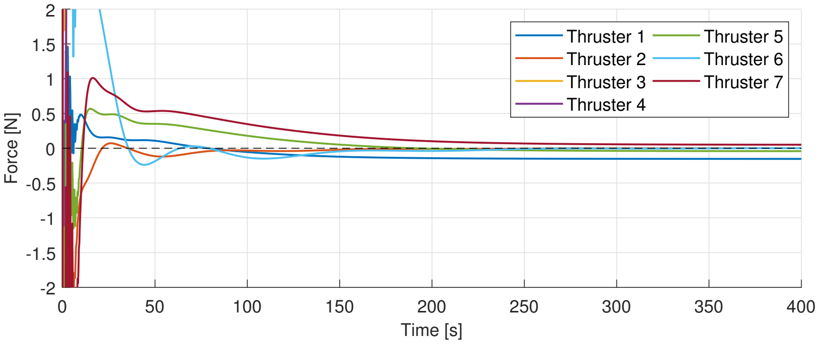

(d) Close-up of thruster forces

Figure 6.20: Simulation results using thrust allocation combination 3 with all thrusters. Cross-track errors and thrust.

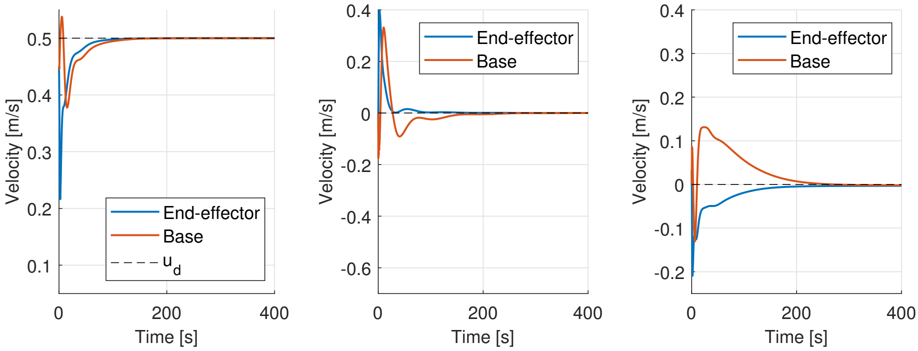

(a) Surge velocity (b) Sway velocity (c) Heave velocity

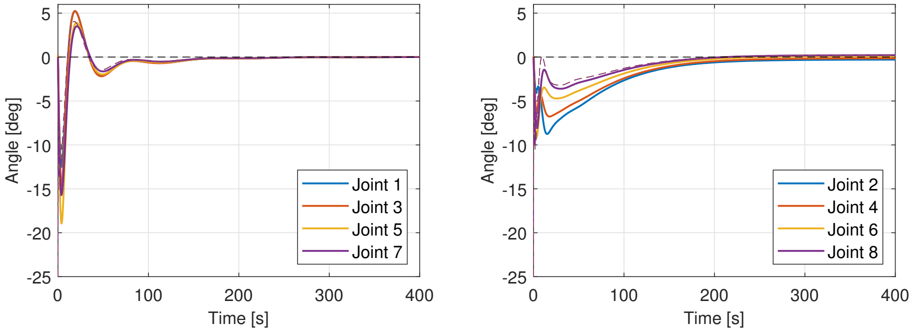

(d) Joint angles of joints rotation about z-axis, reference in coloured dashed line

(e) Joint angles of joints rotation about y-axis, reference in coloured dashed line

Figure 6.21: Simulation results using thrust allocation combination 3 with all thrusters. Velocities and joint angles.

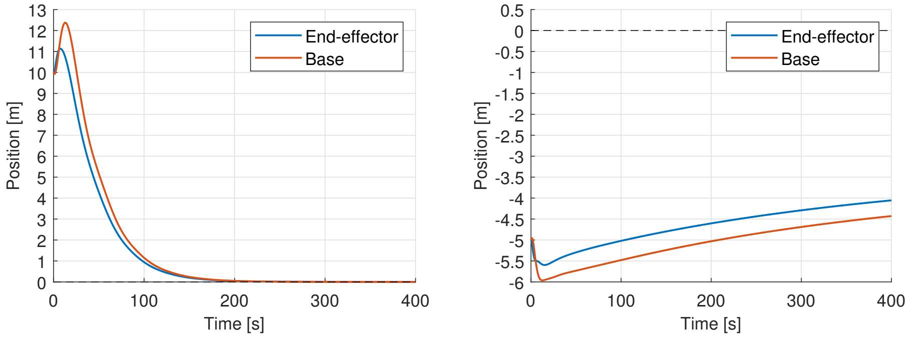

(a) Cross-track error along y-axis

(b) Cross-track error along z-axis

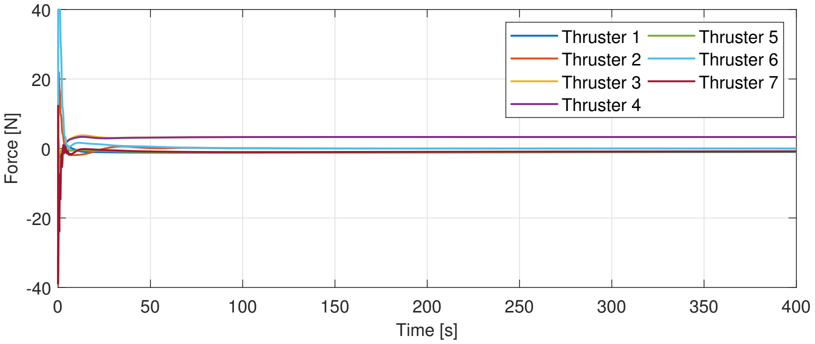

(c) Thruster forces

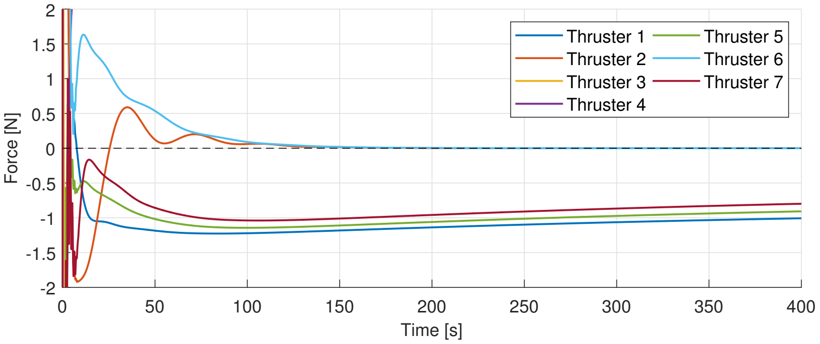

(d) Close-up of thruster forces

Figure 6.22: Simulation results using thrust allocation combination 4 with all thrusters. Cross-track errors and thrust.

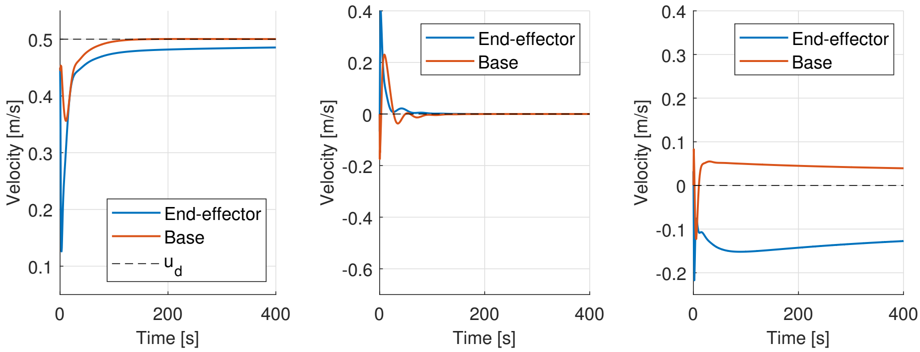

(a) Surge velocity (b) Sway velocity (c) Heave velocity

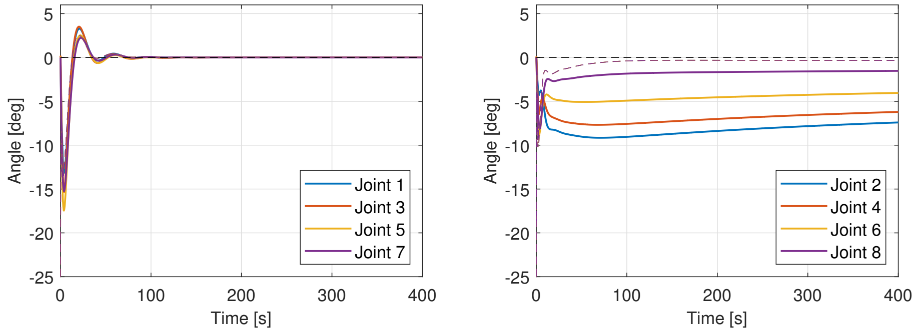

(d) Joint angles of joints rotation about z-axis, reference in coloured dashed line

(e) Joint angles of joints rotation about y-axis, reference in coloured dashed line

Figure 6.23: Simulation results using thrust allocation combination 4 with all thrusters. Velocities and joint angles.

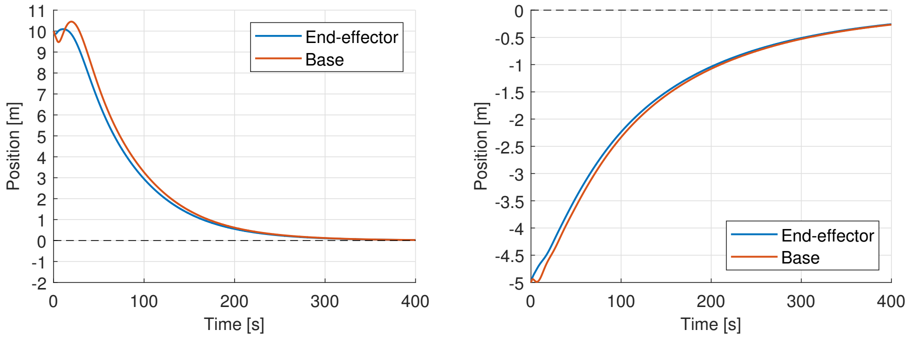

(a) Cross-track error along y-axis (b) Cross-track error along z-axis

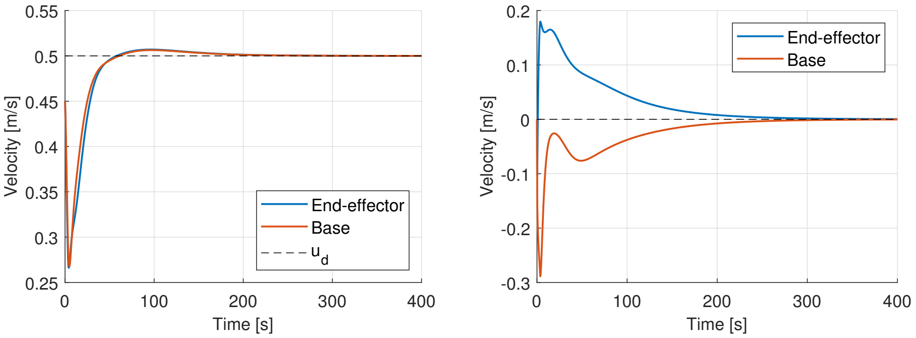

(c) Surge velocity (d) Sway velocity

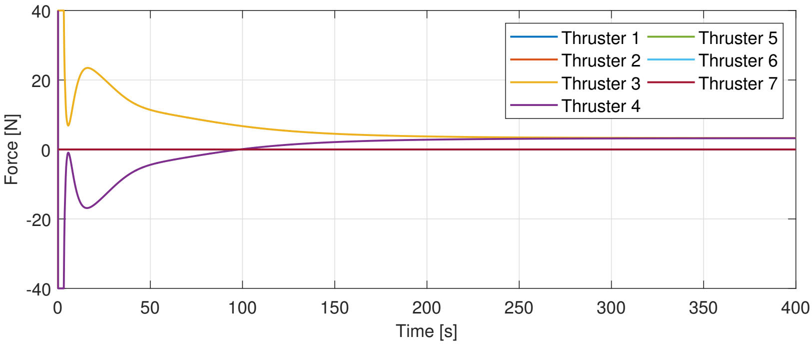

(e) Thruster forces

Figure 6.24: Simulation results using thrust allocation combination 1 with longitudinal thrusters only. Cross-track errors, velocities and thrust.

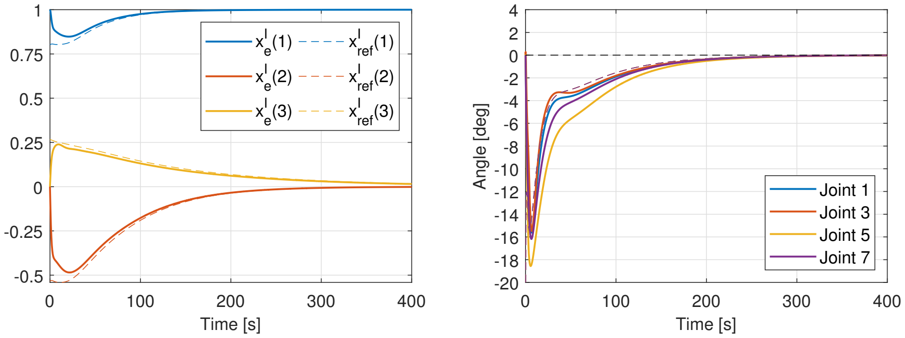

(a) Inertial-frame representation of end-effector x-axis

(b) Joint angles of joints rotating about z-axis

Figure 6.25: Simulation results using thrust allocation combination 1 with longitudinal thrusters only. End-effector pointing direction and joint angles. References in coloured dashed lines.

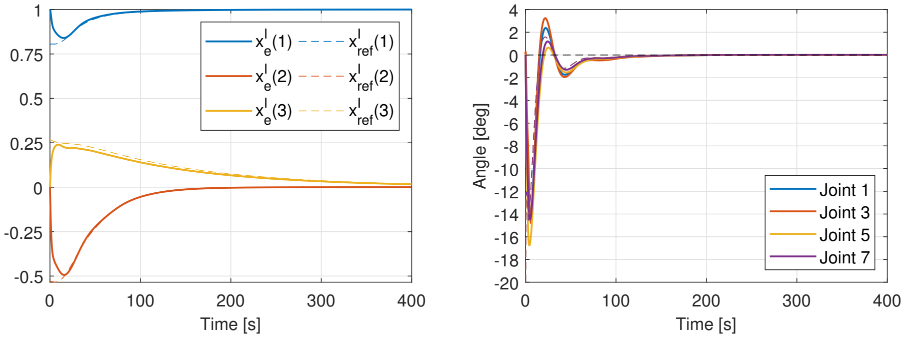

(a) Inertial-frame representation of end-effector x-axis

(b) Joint angles of joints rotating about z-axis

Figure 6.26: Simulation results using thrust allocation combination 3 with longitudinal thrusters only. End-effector pointing direction and joint angles. References in coloured dashed lines.

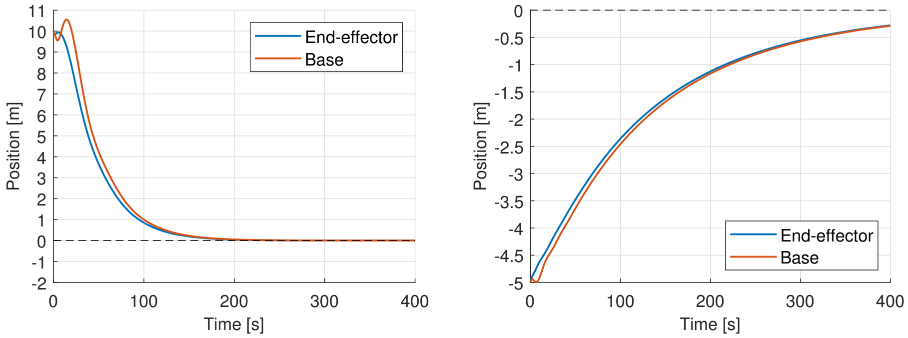

(a) Cross-track error along y-axis (b) Cross-track error along z-axis

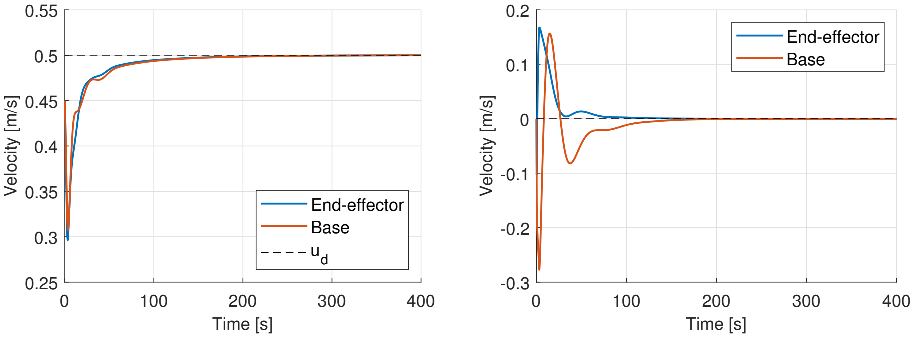

(c) Surge velocity (d) Sway velocity

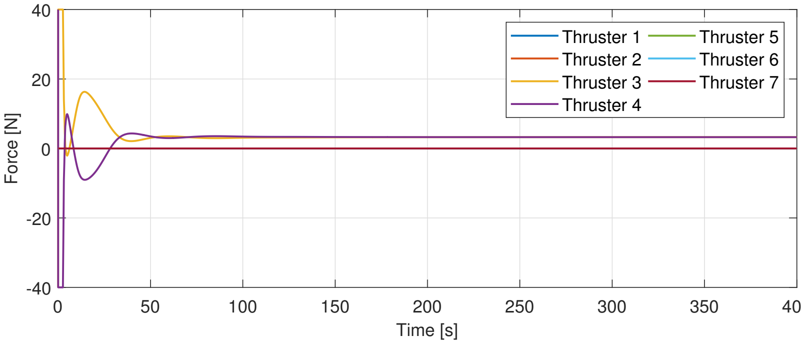

(e) Thruster forces

Figure 6.27: Simulation results using thrust allocation combination 3 with longitudinal thrusters only. Cross-track errors, velocities and thrust.

Chapter 7

Discussion

7.1 Performance of the proposed path-following method

In the simulations presented in Section 6.2, in which the joints are the sole means of controlling the direction of the USM, the USM does not manage to follow the path.

The oscillations in the xy-plane were observed to be be somewhat reduced, but not eliminated by increasing the coefficient k_D in the base angle (5.9). Increasing k_D would however also lead to unstable behaviour during large manoeuvres. A possible cause is discussed in Section 7.6.1.

The control law (3.9) on which the direction control is based relies on exact cancellation of system dynamics. However, the dynamics of the turning motion due to a bent body shape, and considering the joint angles as inputs, have not been derived. If the joints close to the head are used, the end-effector pointing direction will change directly. If the front portion of the USM is kept more straight to keep the direction of the end-effector steady, the turning motion has a natural delay from bending the joints until the end-effector turns due to the forward motion of a curved body. More precise direction control would therefore likely be achieved if the dynamics of the turning motion were derived and taken into consideration. These dynamics would have the joint angles as inputs, by means of changing the mass matrix and coriolis and centripetal matrix.

In [39], where only joints were used for direction control of a USM to achieve planar path following experimentally, no oscillations about the path were reported.

A major difference between the method used in [39] and in the one presented in this thesis is the use of integral action in the base angle. Whether or not this is the deciding factor is uncertain. However, it is not possible to easily extend the control law (5.9) to include integral action due to the attitude error essentially being parametrised as an angle-axis representation. There is therefore no error signal which can be integrated and still have a valid geometrical interpretation. This is further discussed in Section 7.5.

An additional difference between the case considered in this thesis and that in [39] are the properties of the vehicle. The USM used in the experiments in [39] is lighter and more slender than the USM model used in this work. As illustrated by the simulations in Appendix E, increased inertia leads to larger oscillations about the path, likely due to the increased delay in the turning motion. In addition, the USM used in [39] consists of more links, making it able to form a smoother curve.

As it is, the path following method without use of thrusters to stabilise the direction of travel is unsuitable for situations where precise path following is required, such as surveying with a camera or other sensor, or when navigating a cluttered environment. However, for travelling from A to B on fairly open seas it would serve its purpose.

Recovering from a 180° error

The base angles, like the control law upon which they are based, will be zero if the error $\tilde{\phi}$ from the pointing direction is 180°, and both the angular velocity tracking error $\tilde{\boldsymbol{\omega}}^e$ and reference angular acceleration are zero. When combined with the guidance law (5.1), this can only occur if the USM travels straight ahead along the path, but in the opposite direction. As demonstrated by the results in Figures 6.12 and 6.13, the slightest disturbance away from this state will allow the USM to turn in the right direction. In this case, the end-effector of the USM tips slightly down. The shortest distance along the surface of the unit sphere towards the reference direction, which then points gently up back towards the path, is in fact along the lower hemisphere. The reason for why the USM pitches down is explained in Section 7.6.2.

This suggests that even though the case when $\tilde{\phi} = \pi$ has not been analysed for the control law (3.9) due to it being discontinuous at that point, it is likely to behave as an unstable equilibrium, from which the system is easily dislodged. Due to the discontinuous control law, recovery once dislodged from this equilibrium will be very aggressive, as was demonstrated in the simulation of the USM in Figure 6.13.

7.2 Performance of body shapes

The general tendency which can be observed in Figures 6.2-6.5 is that the shapes which keep the front part of the USM more straight follow the path more closely, up to a certain point. Looking closely at Figure 6.6a, increasing α from 0.7 to 1 leads to a marginal increase in the oscillations about the path in the horizontal plane. Increasing α again to 1.5 only increases this amplitude further.

While the straighter shapes stay closer to the path, they perform worse at tracking the pointing direction itself, as can be seen in Figures 6.3a and 6.5a. When the joints nearer the head link are used more, the pointing direction of the end-effector is controlled directly, in the fashion of a manipulator arm. The body is bent so that the end-effector points in the desired direction, without needing to turn the whole body. On the other hand, when the front portion of the USM is kept straight, the pointing direction of the end-effector relies on turning the whole body, while the back portion acts as a tail used to turn the body while in motion. The turning motion due to the combination of a bent shape and forward velocity is slower than due to joint motion directly. This can especially be seen in Figure 6.10a, where use of the exponential curvature causes the USM to travel further away from the path before it turns around.

Since the longitudinal thrusters of the USM used in the simulations are mounted on its center link, keeping the front portion of the USM more straight also points the thrust more in the pointing direction of the end-effector. This explains why the straighter shapes stay closer to the path, despite the greater error from desired pointing direction. Pointing the end-effector towards the path will not help if the thrusters propel the USM in a different direction. As can be seen in Figures 6.2c and 6.2d, straighter shapes give smaller sway and heave velocities of the end-effector, meaning that the velocity of the USM is better aligned with the pointing direction of the end-effector.

Figure 6.9a shows that the uniform and linear curvatures lead to near-identical pointing directions while trying to follow the path. The angle between current and desired pointing direction, shown in Figure 6.11a, is greater for the uniform curvature because the *reference* is different, on account of the difference in cross-track error. The two shapes point their end-effector just as steeply, but the linear remains closer to the path, because its direction of motion is better aligned with the pointing direction of the end-effector.

Among the tested body shapes for the USM, the linear curvature appears to give the smallest oscillations about the path in the xy-plane, as shown in Figure 6.6, while it tracks the reference better than the straighter exponential curvature with $\alpha = 0.7$, as can be seen in Figure 6.5a. Because the linear shape uses the front joints more than the similarly performing exponential curvature, this USM shape results in the reference attitude being tracked faster. However, Figure 6.4c shows that the linear curvature leads to greater sway velocity of the end-effector, meaning the direction of motion is not aligned as well with the end-effector. Since the linear curvature gives less oscillations about the path in the xy-plane despite this, it appears the benefit from directing thrust along the end-effector is at some point offset by the disadvantage of delayed attitude tracking.

When the thrust is pointed more along the x-axis of the end-effector, the effort required to maintain the desired forward velocity is also generally reduced. This can be seen in Figures 6.2f and 6.4f. However, the thrust effort increases again for the exponential curvature with $\alpha = 1.5$. Since this is not due to more of the thrust contributing to velocity in other directions than surge, as confirmed by Figures 6.2c and 6.2d, a possible explanation is that the shape is less hydrodynamically efficient. At $\alpha = 1.5$, the two front joints are kept nearly straight, and the angle of the backmost joint is significantly larger than of the next joint (see Table 6.3). The large base angles due to the large attitude tracking error $\tilde{\phi}$, as seen in Figure 6.3a and e, combined with the steep increase in joint angle give a sharp bend rather than a smooth curve.

In the case of depth control, the observed tendency is that the straighter shapes consequently give faster convergence to the desired depth, though not by much. This is further discussed in the following section.

7.3 Hydrostatic restoring forces

7.3.1 ...Acting on the USM as a whole

When bent in the vertical vertical plane, the USM will experience hydrostatic forces acting on the body as a whole, rotating the body into its hydrostatic equilibrium [1]. Looking at Figure 6.7b, the base and the end-effector of the USM remain at almost the same depth, while the joints about the link frame y-axes are bent, shown by Figure 6.9c. The base and end-effector are almost level for both the uniform an linear curvature. This means that with the linear curvature, the center link must be pointed more upwards, while when the curvature is uniform it will be near horizontal. In the horizontal plane, the USM turns on account if its forward velocity while being a bent shape. In the vertical plane under water, turning upwards is determined more by whether the new hydrostatic equilibirum hasthe end-effector pointing upwards.

The direction of the thrusters is likely the most important factor for vertical motion. As seen in Figures 6.2b and 6.4b, the straighter shapes consequently converge a little faster towards the correct depth. In addition, Figures 6.2d and 6.4d show that the magnitude of the heave velocity is smaller when the shape of the USM is straighter at the front. The heave velocity of the end-effector frame is negative, while its x-axis is pointed upwards, as can be read from Figures 6.8c and 6.9a. Consequently, the total velocity of the USM points less upwards than the end-effector itself, and the USM does not travel as steeply upwards as the guidance law prescribes.

Looking at Figure 6.10b, the USM appears to converge to a stationary offset from the depth at which the path is located. At this depth, the joint angles are likely too small to point the thrusters upwards, especially when counteracted by hydrostatic restoring forces.

7.3.2 ...Acting on individual joints

As can be seen in Figure 6.15b, without the additional term compensating for hydrostatic moments acting on the joints, the joints rotating about the y-axis do not reach their references. The offset is larger for joints 4 and 6. Joints 2 and 8 are placed between an end link and the rest of the USM, and bending them requires moving only one link out of hydrostatic equilibrium. Joints 4 and 6, on the other hand, have to shift larger portions of the USM out of hydrostatic equilibrium when they bend.

However, when the hydrostatic moments are compensated for, the joints still do not follow their references. Instead, they overshoot. Looking at the comparison between the uniform and linear curvature, Figure 6.9c shows that in the case of the uniform curvature, where all joints have the same reference, the overshoot is greater in the joints towards the back of the USM. This means that the "uniform curvature" simulated is not really uniform. Instead, the resulting shape increases in curvature towards the tail of the USM. The overshoot experienced when hydrostatic compensation is applied is larger than the error without, indicating that the total influence of other forces such as due to thrusters, drag or coriolis and centripetal forces exceeds the influence of the hydrostatic moments. In addition, Figure 6.14b shows that hydrostatic compensation does not improve convergence along the z-axis drastically. The improvement can also be in part due to the overshoot of references, and the improvement from the case of no compensation to following the references precisely would likely be smaller. This suggests that the largest influence on vertical motion are not joint angles directly, but hydrostatic forces acting on the USM as a whole.

Additionally, if the available torques are not large enough to match the hydrostatic moments, they may not be able to maintain any semblance of the desired shape, as is the case in Figure E.11 in Appendix E. While the majority of the joints are closer to following their reference, Figure E.9b shows that the resulting shape performs worse than without compensation. The curve without compensation is gentler than desired, but has a more correct curvature, which appears to be the deciding factor in tipping the direction of end-effector and thrusters up.

7.4 Performance of thruster combinations

The main difference between the performance of the four combinations of control using all available thrusters is seen in the cross-track error along z-axis. The control parameters have been chosen such that they eliminate the oscillations seen when attitude was controlled only by means of joints, in particular by the choice of large $k_{\text{ang},D}$. This leads to large and fast-changing forces at the start of the turn, as can be seen in e.g. Figure 6.20c. Such behaviour is at best taxing on the actuators, and at worst impossible to achieve in reality. If parameters were chosen such that the initial input was smoother and smaller, it is possible there would be more visible differences in the influence of the considered thrust allocation combinations on the horizontal motion.

In general, finding and distributing control forces and moments with respect to the base will attempt to rotate the USM about the base, and therefore favour the front transverse thrusters which have a greater lever arm with respect to the base. Correspondingly, control with respect to the end-effector will favour thrusters towards the back of the USM. In order to point the USM end-effector upwards, thrust allocation with respect to base will in general attempt to push the end-effector upwards, while thrust allocation with respect to end-effector will push the base downwards. The danger of such an approach is illustrated by Figure E.12, in which the inertia and hydrostatic restoring moments acting on the USM are too large for the thrusters to be able to rotate the USM. The attempt of pushing only the tail downwards contributes little to rotation, but it does contribute to linear velocity, causing the entire USM to travel downwards.

In the case of which velocity to control, it is important to keep in mind that the USM will curve upwards into a U-shape due to the direction control using joints, but will be rotated into its hydrostatic equilibrium. The x-axis of the end-effector frame will therefore point upwards in the desired direction of travel, and the x-axis of the base will point downwards. Since the thrusters are not pointed up as steeply as the end-effector, the direction of travel is also less steep. This leads to a negative heave velocity of the end-effector, but positive heave velocity of the base, in their respective frames when only longitudinal thrusters are used. This can be seen in Figure 6.8c. Reducing the heave using transverse thrusters will therefore be achieved by thrust up and backwards for the end-effector, and down and forward for the base. Controlling the velocity of the base therefore leads to much slower convergence upwards along the z-axis, as can be seen in Figures 6.16b and 6.20b. Even even though finding the desired forces and moments with respect to the base should lead to the thrusters trying to pull the end-effector upwards, the objective of reducing the heave velocity dominates. Figure 6.20b shows that even the thrust from thruster 7, located towards the front of the USM, is negative, contributing to rotating the end-effector downwards. Since the joint angles about the y-axis still have non-zero references, as seen in Figure 6.21e, the end-effector has not reached its pointing direction reference.

In situations where the USM is used as a manipulator, the position of the base is often desired to be constant, and will be kept steady by the use of thrusters. Using thrusters to rotate about the base is therefore desirable, as the rotation will not disturb the position of the base. However, the inertia of the USM about an endpoint is larger than about its center of mass [12]. Rotating the USM about its CM would require less thrust effort. In addition, the sum of forces required to rotate the USM about its CM will be smaller because they will act in opposite directions, thus interfering less with control of linear velocity. Finding the desired control moments about the CM and allocating control also with respect to the CM could therefore be beneficial for settings where the USM is travelling like a vehicle, and control of both attitude and velocity takes precedence over precise positioning.

While the mass matrix and TCM already depend on the configuration of the

USM, having the point with respect to which they are found also move depending on the joint configuration increases the complexity of finding these matrices. A compromise could be to use the mass matrix and TCM with respect to a point which can be assumed to remain relatively close to the true CM in most configurations. Such a point could be the CM of the USM in an outstretched configuration.

Thrust allocation among only the longitudinal thrusters is less influenced by the choice of which point the forces and thrust are found with respect to, because these thrusters cause rotation in the same direction about either point. Comparing Figures 6.24a and 6.27a shows that control with respect to the base turns the USM towards the path faster. This is also seen from the pointing direction of the end-effector in Figures 6.25a and 6.26a. The sway velocity in Figure 6.27d is reduced quickly, causing the thrust from the two thrusters to converge faster to the same thrust required for forward travel at the desired surge velocity, as seen in Figure 6.27e.

In the case of control with respect to the end-effector, the pointing direction is slow to converge, causing the USM to remain bent towards the path for a longer time, as seen in Figure 6.25b. Thruster 3 is then on the inside of the C-shape formed by the USM, and thruster 4 on the outside. Figure 6.25b shows that thruster 3 gives forward thrust, and thruster 4 backwards, which contributes to rotation *away* from the path. A possible explanation for this is that the gain $k_{\text{ang},P}$ is too small, and the combination of mass matrix when in a bent configuration, and desired linear and angular accelerations requires the thrusters to create an opposite moment for the resulting angular acceleration to be equal to $a_{c,\text{ang}}$. This illustrates the challenge in combining the use of both thrusters and joints for direction control. The two means of influencing the attitude may interfere with each other if the control parameters are not carefully selected.

Despite this, the use of different thrust for the two available longitudinal thrusters makes it possible to stabilise the oscillations in the xy-plane which occurred when equal thrust was applied to both thrusters. Comparing the results in Figures 6.24b and 6.27b to those in Figure 6.7b, thrust allocation between longitudinal thrusters did not significantly change convergence in depth compared to the case of simple forward thrust. This is as expected, given the fairly small roll angles the USM had, shown in Figure 6.5b. The two longitudinal thrusters then act in the xy-plane, in which the USM is not naturally stabilised by hydrostatic forces. The combination of passive stabilisation and longitudinal thrusters on either side of the USM therefore shows great promise for the purpose of steady direction control.

It is worth noting that the thruster forces in Figures 6.24e and 6.27e undergo fast and large changes in magnitude in order to perform the initial turn towards the path. This may not be possible with realistic actuator dynamics, and the method of stabilising the motion in the xy-plane by use of the longitudinal thrusters only might therefore perform worse when realistic actuator dynamics are taken into consideration.

When direction control of the end-effector is performed mainly using the joints of the USM, the tail end will need to swing sideways, and will therefore necessarily undergo great changes in velocity, as seen in Figure 6.8a-b. Control of the base velocity when only longitudinal thrusters are used therefore gave in general poor performance, and has not been shown. That control of the base velocity when using thrust allocation among longitudinal thrusters with respect to the end-effector gave results similar to those shown in Figures 6.26 and 6.27 is therefore surprising.

Parameters such that the thrust allocations methods could be combined with the linear or exponential curvatures were difficult to find. A possible reason is again the delay in turning the pointing direction using these shapes. The thrusters would therefore have to contribute more to the turning, making it more important to select parameters that balance the control of rotation and linear velocity when thrusters are used to perform both.

A better approach could be to use thrusters for controlling only the velocity of the end-effector, ensuring it has the desired forward velocity and minimal transverse velocity. The task of pointing the end-effector, and consequently its velocity, in the right direction would then be left entirely to the joints. The question remains whether the resulting improvement at path-fallowing compared to the case of using only the longitudinal thrusters would be large enough to make it worth engaging additional thrusters.

7.5 Is geometric attitude control suitable for USMs?

The benefits of the geometric approach taken in this work is that it does not have fixed singularities, allowing the USM to be pointed in any direction. In addition, the error measures lie directly in the plane spanned by the actuated axes regardless of the roll about the pointing direction. Moreover, the resulting trajectory towards the reference is always along the shortest path on the surface of the unit sphere.

As it turns out, the USM used in the simulations presented in Chapter 6 is not able to fully reap the benefits of this method of attitude control. This is mainly due to its passively stabilised links.

Throughout the simulations, the roll of the end-effector frame tends to zero. This should not be a surprise, as the USM will tend to a straight configuration when the error from the desired pointing direction is small, in which it is similar to a typical, slender rigid-body AUV. The motion of a passively stabilised vehicle is distinctly different in the horizontal and vertical plane, where vertical is to be understood as parallel to the direction of gravity. The geometric control law, on the other hand, treats all directions the same. This is especially true when all elements of the error variables are scaled by the same gains, both in the guidance law and the direction control by means of base angles. This was done with the intention of observing the performance of the proposed method if nothing is assumed about the system's behaviour, nor the orientation of the world frame, aligned with the path, relative to the direction of gravity.

Not only does the proposed control scheme treat all direction equally, but they are also connected through the error angle $\tilde{\phi}$ by which all inputs are scaled. The influence of this can be seen by comparing the convergence in depth when the initial error angle is small, in Figure 6.4b, with the case of a large initial error in Figure 6.10b. Because all inputs are scaled by the same error, the large initial error in the horizontal plane also leads to faster convergence in the vertical plane. This coupling can also have some very undesirable effects, such as the oscillations about the path in the xy-plane causing oscillation in all joint references, seen in e.g. Figure 6.9c.

In an underwater setting, and if hydrostatic forces are in play, controlling attitude along the shortest distance on the surface of the unit sphere is not necessarily the most efficient. This is illustrated by the case of the 180° error in Figure 6.13, where the disturbance leads to the shortest distance being along the underside of the sphere, along which the USM has to battle the hydrostatic restoring forces.

Passively stabilised USMs would therefore benefit from decomposing the attitude error into a rotation about the direction of gravity, and a rotation in a vertical plane. In other words, using a control law based on tracking of Euler angles in an inertial frame with one axis parallel to the direction of gravity, like in previous works on slender-bodied AUVs such as [9, 10, 32]. Since the simulations in Chapter 6, using a roll-indepent method of attitude control, confirm that the roll of the USM will tend to zero, joints rotating about the y-axes can reasonably be used directly for control of pitch, and those rotating about the z-axes for control of yaw.

The nature of vertical and horizontal motion is even more distinct for USMs, which can have a varying placement of their CM and CB. If control of horizontal and vertical motion was decoupled, vertical motion could be achieved by exploiting this ability to simply tilt the thrusters of the USM upwards or downwards.

In addition, unlike the total angle error $\tilde{\phi}$ used in this work, errors in pitch and yaw in the Euler angle representation have a defined direction, and can reasonably be integrated. A reason why this might be important for direction control of USM using their joints is that for sufficiently small joint angles, the resulting curvature of the body may be too small to cause it to turn. A control law which curves joints proportionally to the attitude error risks having a "blind zone" about the reference, in which the error is too small to give a body curve with any effect.

Finally, the control law (3.9) for the general two-torque system gives tracking only for systems whose inertia fulfils Assumption 1. As said in Remark 1, the assumption can be fulfilled also under the influence of added mass effects by the body having rotational symmetry about the unactuated axis, or reflectional symmetry through the plane perpendicular to the unactuated axis. A USM can only achieve this when kept rigid, or if its link configuration is fore/aft symmetric, and its joints are bent such that the curve is also symmetric. Assumption 1 would then hold for a frame located at the midpoint of the USM, about which the whole USM would be fore/aft symmetric.

However, Assumption 1 does not take into account the possibility of coupling between the linear and rotational DOFs. This would have to be handled by inverting the mass matrix to find accelerations directly, and cancelling all effects due to the coupling.

7.6 Disturbances

7.6.1 Coupling between joints dynamics

During simulations it was observed that the motion of joints rotating about the z-axes induced oscillations in the joints which rotate about the y-axes. The phenomenon is shown in Figure 7.1, where a unit step has been given as reference to the joints acting in the horizontal plane, and no thrust is applied. The PD-controller (5.15) is used without the hydrostatic compensation term.

The opposite, applying a unit step reference to the joints rotating about the y-axes, did not induce motion in the other joints. Oscillation in joint angles about the y-axes while having non-zero angles in the joints rotating abut the z-axes will give the end-effector frame an oscillating roll. Since the full orientation of the end-effector frame is used for transforming the reference into the end-effector frame, these oscillations can spread to the direction control and joint references.

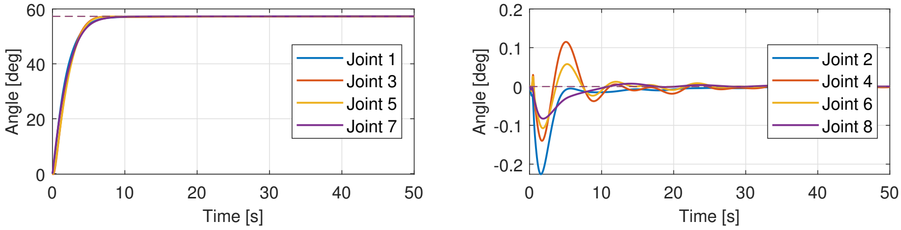

(a) Angle of joints rotating about z-axis, reference in dashed line

(b) Angle of joints rotating about y-axis

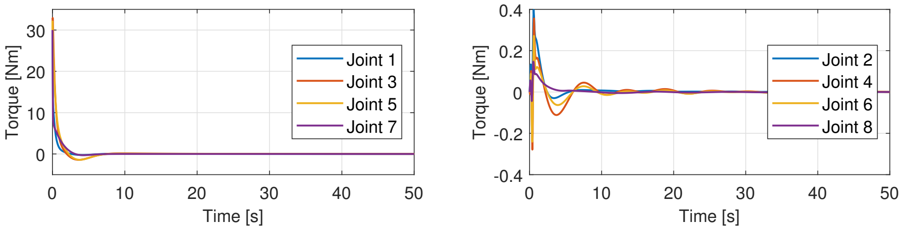

(c) Joint torques about z-axis

(d) Joint torques about y-axis

Figure 7.1: Response of joints to a unit step (in radians) as reference for joints rotating about z-axis.

This is likely the cause of the oscillations which can be observed in Figure 6.11, in both roll, angular velocity error and the base angles for the joints references. When the roll angle is large due to performing a large turn, the angular velocity about the y-axis has a greater influence on the attitude.

These high-frequency oscillations during large attitude manoeuvres are in turn the reason why the parameters of the direction controller (5.9) were not chosen such that they reduce oscillations about the path in the horizontal plane any more.

7.6.2 Moment about y-axis from longitudinal thrusters

In the simulations shown throughout Chapter 6, the USM is started at a velocity slightly lower than the desired. Otherwise, the USM would slow down due to drag and no thrust to compensate, before returning to the desired surge. Either way, the USM will need to accelerate by use of thrusters. The same thruster force will tip the front end of the USM down. This is due to its center of mass being located below the plane through the middle of the cylindrical links, while the two longitudinal thrusters are located in this plane. The longitudinal thrusters therefore have a small lever arm about the center of mass.

Figure 7.2 shows the case when the USM is kept rigid, that is, all joints are given reference 0, and it has to accelerate from initial surge velocity 0.45 m/s to the desired surge velocity 0.5 m/s using the PI-controller (5.16). The USM tips back and forth before settling, likely due to the stabilising hydrostatic moments. However, it ends up at a slight offset from the depth at which it started. The greater the thruster forces used, the greater the offset. Since most of the turning scenarios use more thrust at the start of the turn, they will be influenced more by this phenomenon than the scenario in Figure 7.2.

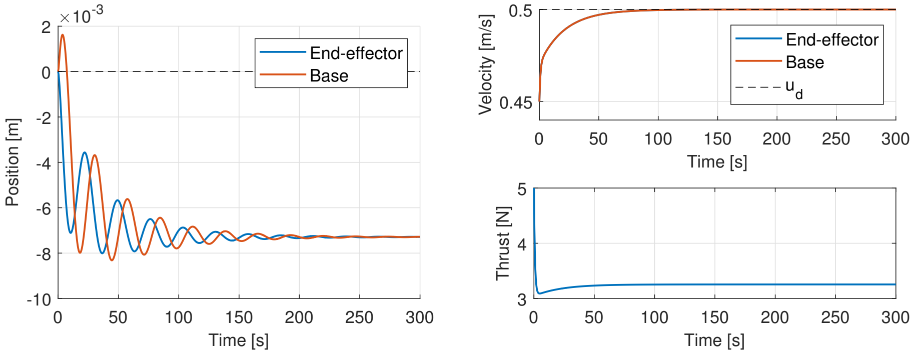

(a) Position along z-axis (b) Surge velocity and thrust

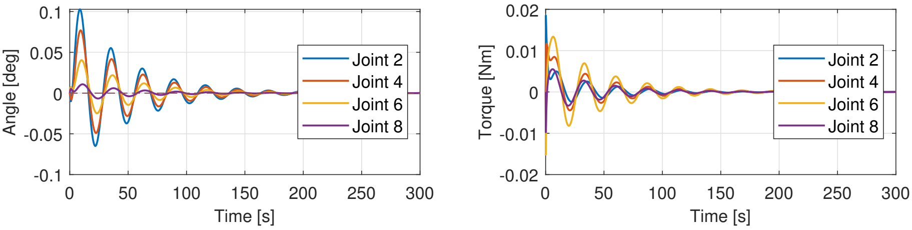

(c) Joint angles about y-axes (d) Joint torques about y-axes

Figure 7.2: Response to accelerating while maintaining a straight shape.

The forward tipping bring each of the links out of hydrostatic equilibrium, inducing moments and consequently oscillations in the joints as well. The full version of the joint controller (5.15) is used in the scenario shown in Figure 7.2. Using it without the hydrostatic compensation reduced the duration of the oscillations, and also slightly reduced the final offset from starting depth.

7.7 Assumptions and limitations

The controllers used in this work rely on feedback from numerous states of the USM, without regard for which of them may realistically be measured. It is also assumed that parameters of the USM required to compute hydrostatic moments on joints, and parameters of the mass matrix are fully known. Especially in the case of the mass matrix, this is difficult to achieve, as the full mass matrix has been used, including added mass effects. These rely on hydrodynamic coefficients which can be difficult to determine exactly. A compromise could be to use only the rigid body mass and inertia, as was done in [45]. This would likely change the performance of the thrust allocation methods which use the mass matrix to compute the desired forces and moments.

Dynamics of the actuators have also not been considered. Especially the transverse thrusters may struggle with providing some of the more aggressively changing forces seen in the simulations. Transverse thrusters are typically tunnel thrusters, which must shift the flow of the water through the tunnel when they change the thrust.

Most of the simulations have also been performed without saturating the joint torques. The scenarios requiring large joint angles, esecially at the beginning, will therefore likely have worse performance. In addition, the joints of the real-life USM upon which the model is based are actuated by servo motors capable providing a maximum rate of 30 rpm. While working with the model subject to the too large inertia and hydrostatic forces, the angular rates of the joints were observed to be well within what the actuators could realistically provide, and were therefore not considered further. With the correct model parameters the USM is capable of faster joint movements, and the realistic angular rates could have been exceeded. Saturating the angular velocities of the joints could therefore also impact the scenarios requiring aggressive control.

Chapter 8

Conclusion

In this thesis, a path-following method for USM moving in 3D has been presented. As a first step, a control law for the tracking of a pointing direction of a body possessing only two control torques was developed. The control law gives asymptotic tracking of the reference from any initial conditions where the initial pointing direction is not exactly opposite to the reference, and for sufficiently small velocity errors. This means that unlike control laws formulated on representations with singularities, this control law places no restrictions on what the system and reference pointing directions may be relative to an inertial world frame.

Based on the control law, a method for direction control of USMs using their joints to point the end-effector in the desired direction of travel is proposed. The direction control method is combined with a guidance law to form a path-following controller for following straight paths.

Simulations of the path-following method show that the method gives oscillations about the path in the horizontal plane, with an amplitude of less than 0.5 m about the path. A possible cause of these oscillations is the inherent latency in the turning motion of a bent body with forward velocity.

In contrast, the convergence in depth is slow, and appears to tend to a stationary offset. Due to hydrostatic restoring forces, the USM is rotated back into its hydrostatic equilibrium, in which the tail and end-effector have the same depth. The direction of travel is therefore primarily influenced by the direction of thrust at hydrostatic equilibrium. Compensating for hydrostatic moments acting on the individual joints improves the convergence in depth somewhat, however, it also causes the joints to overshoot their references due to the remaining uncompensated dynamics.

Investigation of different body curvatures for the purpose of turning the USM show that there appears to be an optimal balance between keeping the front of the USM straight in order to point the thrusters along the desired direction of travel in which the end-effector points, and better tracking of the pointing direction by actively using the joints closer to the head. Among the curvatures tested, linearly increasing curvature towards the tail end gave the smallest oscillations in the horizontal plane. In the vertical plane, the straighter shapes performed consequently better, due to the direction of thrust at hydrostatic equilibrium pointing more upwards.

Exploiting the presence of multiple longitudinal thrusters to stabilise the turning motion eliminated the oscillations about the path, making it a promising option for steady direction control without angaging more thrusters. The use of transverse thrusters improved convergence to the correct depth in some of the combinations tested. However, using thrusters to generate control moments found with respect to an endpoint of the USM can lead to inefficient attempts at rotating the USM. This would likely improve if the control moments were instead found with respect to the CM of the USM.

Simulations of the USM also show the strength of the type of geometric attitude control laws to which the control law developed in this thesis belongs. Even if the system does start pointing exactly opposite the reference, the slightest disturbance can dislodge it from that state, and the system will converge to its reference.

Without further improvement, the proposed path following method when using thrusters solely for forward propulsion is not suitable for precise path following. It could however serve for transportation of the USM over open areas.

8.1 Further work

Additional simulations should be run to investigate the performance of the proposed path-following method on USM models with different physical properties, in particular a model of the USM used in [39]. This could help understand the cause of the oscillations observed in this work, which were not reported in [39]. It would also be useful to observe the performance of different shapes on a USM with longitudinal thrusters at its tail rather than center, since placing the thrusters at the tail makes it more difficult to direct the thrust along the pointing direction of the head.

If the cause lies in the inertia and turning dynamics of the USM, deriving the dynamics of the turn with joints as inputs would enable the development of more accurate direction control.

For the use of thrusters to control the attitude of the USM while travelling like a vehicle, the mass and thrust configuration matrices should be derived with respect to the CM, or a fixed point which can be assume to be reasonably close to the CM. In order to better examine the performance of options relying on thrusters, thruster dynamics should also be taken into consideration. A more realistic behaviour without modelling the full thruster dynamics could be achieved by limiting the rate of change of the commanded thrust.

Based on the observations in this work, the following combinations of body shape and thrusters could be worth testing: the linear curvature with different slopes, and a shape in which the front three links are kept rigid and the two backmost joint are used more. Using only vertical transverse thrusters for better depth control could also be a good compromise between conserving energy by using less thrust and achieving precise path following. For the purpose of developing energy-efficient methods, actual energy consumption by the actuators used would have to be investigated.,

Long-term possibilities for furture work include extending the path-following method to handle ocean currents by including an observer, similarly to what was done for surface vessels and USRs moving in a plane in [22, 33].

Appendix A

Definitions and Theorems

A.1 Mathematical Definitions

Definition A.1 (Special Orthogonal Group)**.** The special orthogonal group $SO(3)$ is the set of all rotation matrices, and is defined as

$$SO(3) = \left\{ \mathbf{R} \in \mathbb{R}^{3\times 3} \mid \mathbf{R}\mathbf{R}^\top = \mathbf{R}^\top\mathbf{R} = I,\ \det(\mathbf{R}) = 1 \right\}$$

Definition A.2 (Two-sphere)**.** The two-sphere $\mathbb{S}^2$ is defined as

$$\mathbb{S}^2 = \left\{ \mathbf{x} \in \mathbb{R}^3 \mid \|\mathbf{x}\| = 1 \right\}$$

where $\|\cdot\|$ is the Euclidean norm.

Definition A.3 (Definition 2.2, [13])**.** The vector cross-product can be expressed as

$$\boldsymbol{\lambda} \times \mathbf{a} \triangleq \mathbf{S}(\boldsymbol{\lambda})\mathbf{a}$$

where $\mathbf{S}(\boldsymbol{\lambda})$ is defined as

$$\mathbf{S}(\boldsymbol{\lambda}) = -\mathbf{S}(\boldsymbol{\lambda})^\top = \begin{bmatrix} 0 & -\lambda_3 & \lambda_2 \\ \lambda_3 & 0 & -\lambda_1 \\ -\lambda_2 & \lambda_1 & 0 \end{bmatrix}, \quad \boldsymbol{\lambda} = \begin{bmatrix} \lambda_1 \\ \lambda_2 \\ \lambda_3 \end{bmatrix}$$

Lemma A.1 (Lemma 2.8.2, [2]). *Let* $\mathbf{A} \in \mathbb{R}^{n\times n}$ *and* $\mathbf{D} \in \mathbb{R}^{m\times m}$ *be nonsingular. Then,*

$$\begin{bmatrix} \mathbf{A} & \mathbf{0} \\ \mathbf{0} & \mathbf{D} \end{bmatrix}^{-1} = \begin{bmatrix} \mathbf{A}^{-1} & \mathbf{0} \\ \mathbf{0} & \mathbf{D}^{-1} \end{bmatrix}$$

A.2 Stability Theorems and Definitions

Consider the system

$$\dot{x} = f(x) \tag{A.1}$$

where $f : D \to \mathbb{R}^n$ is locally Lipschitz in x for $x \in D \subset \mathbb{R}^n$.

Definition A.4 (Definition 4.1, [20]). The equilibrium point $x = 0$ of (A.1) is

stable if, for each $\epsilon > 0$, there is $\delta = \delta(\epsilon) > 0$ such that

$$\|x(0)\| < \delta \Rightarrow \|x(t)\| < \epsilon, \quad \forall t \geq 0$$

unstable if it is not stable.

asymptotically stable if it is stable and δ can be chosen such that

$$\|x(0)\| < \delta \Rightarrow \lim_{t\to\infty} x(t) = 0$$

Definition A.5 (Positively invariant set [20, p. 127]). A set M is said to be a *positively invariant set* with respect to (A.1) if

$$x(0) \in M \Rightarrow x(t) \in M, \quad \forall t \geq 0$$

Theorem A.1 (LaSalle's invariance theorem, Theorem 4.4, [20]). *Let* $\Omega \subset D$ *be a compact set that is positively invariant with respect to* (A.1). *Let* $V : D \to \mathbb{R}$ *be a continuously differentiable function such that* $\dot{V} \leq 0$ *in* Ω. *Let* E *be the set of all points in* Ω *where* $\dot{V}(x) = 0$. *Let* M *be the largest invariant set in* E. *Then every solution starting in* Ω *approaches* M *as* $t \to \infty$.

Corollary A.1 (Corollary 4.1, [20]). *Let* $x = 0$ *be an equilibrium point for* (A.1). *Let* $V : D \to \mathbb{R}$ *be a continuously differentiable positive definite function on a domain* D *containing the origin* $x = 0$, *such that* $\dot{V}(x) \leq 0$ *in* D. *Let* $S = \{x \in D \mid \dot{V}(x) = 0$ *and suppose that no solution can stay identically in* S, *other than the trivial solution* $x \equiv 0$. *Then, the origin is asymptotically stable.*

Appendix B

Stability Proof

The proof of Theorem 1 is given here. Some useful properties of the matrices involved are introduced as preliminaries. The rest of the proof is divided into two parts. First, asymptotic stability of the tracking controller is shown. Then it is shown that the region of attraction is as given by the expression (3.10).

Preliminaries

Since the columns of $\mathbf{H}$ are the unit vectors $\mathbf{e}_2$, $\mathbf{e}_3$ respectively, $\mathbf{H}$ has the following properties:

$$\mathbf{H}^\top \mathbf{H} = \mathbf{I}_2 \tag{B.1}$$

$$\mathbf{v} \perp \mathbf{e}_1 \Leftrightarrow \mathbf{H}\mathbf{H}^\top \mathbf{v} = \mathbf{v} \tag{B.2}$$

Due to the block-diagonal structure of $\mathbf{J}$ imposed by assumption 1, it holds that

$$\mathbf{H}\mathbf{H}^\top \mathbf{J} = \left(\mathbf{H}\mathbf{H}^\top \mathbf{J}\right)^\top = \mathbf{J}\mathbf{H}\mathbf{H}^\top \tag{B.3}$$

Furthermore, by Lemma A.1, the inverse $\mathbf{J}^{-1}$ has the same block diagonal structure as $\mathbf{J}$, which means that

$$\left(\mathbf{H}^\top \mathbf{J}\mathbf{H}\right)^{-1} = \mathbf{J}_{22}^{-1} = \mathbf{H}^\top \mathbf{J}^{-1}\mathbf{H} \tag{B.4}$$

Proof of Theorem 1

Inspired by the choice in [7], consider the Lyapunov function candidate $V(\tilde{\phi},\ \tilde{\boldsymbol{\omega}}^b) : D \ \rightarrow \ \mathbb{R}$, where the domain D is $[0,\pi) \times \mathbb{R}^2$

$$V = \frac{k_P}{2}\tilde{\phi}^2 + \frac{1}{2}\tilde{\boldsymbol{\omega}}^{b\top}\mathbf{H}^\top\mathbf{J}\mathbf{H}\tilde{\boldsymbol{\omega}}^b \tag{B.5}$$

where $\tilde{\boldsymbol{\omega}}^b = \mathbf{H}^\top\left(\boldsymbol{\omega}^b - \tilde{\mathbf{R}}\boldsymbol{\omega}^b_{\text{ref}}\right)$ is the angular velocity tracking error represented in the body frame. V is continuous and continuously differentiable on the domain $[0,\pi) \times \mathbb{R}^2$, since $\tilde{\mathbf{R}}$ is continuous on the interval $\tilde{\phi} \in [0,\pi)$.

By Assumption 1, the inertia matrix $\mathbf{J}$ has a block diagonal structure such that $\mathbf{H}^\top\mathbf{J}\mathbf{H} = \mathbf{J}_2$, the lower-right block of $\mathbf{J}$. Since the leading principal minors of $\mathbf{J}_{22}$ are also leading principal minors of $\mathbf{J}$, this gives $\mathbf{J} > 0 \Rightarrow \mathbf{J_2} > \mathbf{0}$. Hence V is positive definite.

The time derivative of V is

$$\dot{V} = k_P\tilde{\phi}\dot{\tilde{\phi}} + \tilde{\boldsymbol{\omega}}^{b\top}\mathbf{J}_{22}\mathbf{H}^\top\left(\dot{\boldsymbol{\omega}}^b - \dot{\tilde{\mathbf{R}}}\boldsymbol{\omega}^b_{\text{ref}} - \tilde{\mathbf{R}}\dot{\boldsymbol{\omega}}^b_{\text{ref}}\right) \tag{B.6}$$

The matrix $\tilde{\mathbf{R}}$ is defined as the matrix rotating the reference $\mathbf{x}^b_{\text{ref}}$ to $\mathbf{e}_1$, but it can also be viewed as the matrix which transforms the representation of a vector in the body frame into its representation in a frame with x-axis aligned with the reference $\mathbf{x}^b_{\text{ref}}$, obtained by rotating the whole body frame by $\tilde{\mathbf{R}}^\top$. The angular velocity of this frame relative to the body frame is the same as the angular velocity of the reference relative to the body frame, which is $\boldsymbol{\omega}^b_{\text{ref}} - \boldsymbol{\omega}^b$.

The derivative of $\tilde{\mathbf{R}}$, and in turn $\mathbf{x}^b_{\text{ref}}$, is therefore

$$\dot{\tilde{\mathbf{R}}} = \tilde{\mathbf{R}}\mathbf{S}(\boldsymbol{\omega}^b - \boldsymbol{\omega}^b_{\text{ref}}) \tag{B.7}$$

$$\begin{aligned} \dot{\mathbf{x}}^b_{\text{ref}} &= \dot{\tilde{\mathbf{R}}}^\top\mathbf{e}_1 = \left(\tilde{\mathbf{R}}\mathbf{S}(\boldsymbol{\omega}^b - \boldsymbol{\omega}^b_{\text{ref}})\right)^\top\mathbf{e}_1 \\ &= -(\boldsymbol{\omega}^b - \boldsymbol{\omega}^b_{\text{ref}}) \times (\tilde{\mathbf{R}}^\top\mathbf{e}_1) = -(\boldsymbol{\omega}^b - \boldsymbol{\omega}^b_{\text{ref}}) \times \mathbf{x}^b_{\text{ref}} \end{aligned} \tag{B.8}$$

Then $\dot{\tilde{\phi}}$ is found by differentiating (3.6) and inserting (B.8) for $\dot{\mathbf{x}}^b_{\text{ref}}$, which gives

$$\begin{aligned}\dot{\tilde{\phi}} &= -\frac{1}{\sqrt{1-(\mathbf{e}_1^\top \mathbf{x}^b_{\text{ref}})^2}}\mathbf{e}_1^\top \dot{\mathbf{x}}^b_{\text{ref}} = \frac{1}{\sqrt{1-(\cos\tilde{\phi})^2}}\mathbf{e}_1^\top \left(\left(\boldsymbol{\omega}^b - \boldsymbol{\omega}^b_{\text{ref}}\right) \times \mathbf{x}^b_{\text{ref}}\right) \\ &= \frac{1}{\sin\tilde{\phi}}\mathbf{e}_1^\top \left(\left(\boldsymbol{\omega}^b - \boldsymbol{\omega}^b_{\text{ref}}\right) \times \mathbf{x}^b_{\text{ref}}\right)\end{aligned} \tag{B.9}$$

Inserting (B.9), (3.5) for $\dot{\boldsymbol{\omega}}^b_{\text{ref}}$, and the dynamics (3.1) into $\dot{V}$ in (B.6) gives

$$\begin{aligned}\dot{V} = k_P \frac{\tilde{\phi}}{\sin\tilde{\phi}}\mathbf{e}_1^\top \left(\left(\boldsymbol{\omega}^b - \boldsymbol{\omega}^b_{\text{ref}}\right) \times \mathbf{x}^b_{\text{ref}}\right) + \tilde{\boldsymbol{\omega}}^{b\top}\mathbf{J}_2\mathbf{H}^\top \Big(\mathbf{J}^{-1}\left(\mathbf{f} + \mathbf{H}\mathbf{u}\right) \\ - \tilde{\mathbf{R}}\left(\left(\boldsymbol{\omega}^b - \boldsymbol{\omega}^b_{\text{ref}}\right) \times \boldsymbol{\omega}^b_{\text{ref}}\right) - \tilde{\mathbf{R}}\left(-\boldsymbol{\omega}^b \times \boldsymbol{\omega}^b_{\text{ref}} + \mathbf{R}^b_i\left(\mathbf{x}^i_{\text{ref}} \times \ddot{\mathbf{x}}^i_{\text{ref}}\right)\right)\Big)\end{aligned} \tag{B.10}$$

Inserting (3.9) for $\mathbf{u}$ then gives

$$\begin{aligned}\dot{V} = {} & k_P \frac{\tilde{\phi}}{\sin\tilde{\phi}}\mathbf{e}_1^\top \left(\left(\boldsymbol{\omega}^b - \boldsymbol{\omega}^b_{\text{ref}}\right) \times \mathbf{x}^b_{\text{ref}}\right) \\ & + \tilde{\boldsymbol{\omega}}^{b\top}\mathbf{J}_2\mathbf{H}^\top \Bigg[\mathbf{J}^{-1}\Bigg(\mathbf{f} + \mathbf{H}\mathbf{H}^\top \Bigg(-\mathbf{f} - k_P \frac{\tilde{\phi}}{\sin\tilde{\phi}}\left(\mathbf{x}^b_{\text{ref}} \times \mathbf{e}_1\right) \\ & - \; k_D\Big(\boldsymbol{\omega}^b - \tilde{\mathbf{R}}\boldsymbol{\omega}^b_{\text{ref}}\Big) + \mathbf{J}\tilde{\mathbf{R}}\mathbf{R}^b_i\left(\mathbf{x}^i_{\text{ref}} \times \ddot{\mathbf{x}}^i_{\text{ref}}\right)\Bigg)\Bigg) \\ & - \tilde{\mathbf{R}}\left(\boldsymbol{\omega}^b \times \boldsymbol{\omega}^b_{\text{ref}}\right) - \tilde{\mathbf{R}}\left(-\boldsymbol{\omega}^b \times \boldsymbol{\omega}^b_{\text{ref}} + \mathbf{R}^b_i\left(\mathbf{x}^i_{\text{ref}} \times \ddot{\mathbf{x}}^i_{\text{ref}}\right)\right)\Bigg]\end{aligned} \tag{B.11}$$

This is where the part of $\dot{\boldsymbol{\omega}}^b_{\text{ref}}$ due to it being a representation in the moving body frame is cancelled out by the derivative of $\tilde{\mathbf{R}}$, removing the need to cancel it by feedforward.

Regrouping of the terms in (B.11) results in

$$\begin{aligned}\dot V = &-k_D\tilde{\boldsymbol\omega}^{b\top}\mathbf J_2\overbrace{\mathbf H^\top\mathbf J^{-1}\mathbf H}^{=\mathbf J_2^{-1}}\overbrace{\mathbf H^\top\left(\boldsymbol\omega^b-\tilde{\mathbf R}\boldsymbol\omega^b_{\mathrm{ref}}\right)}^{=\tilde{\boldsymbol\omega}^b}\\ &+k_P\frac{\tilde\phi}{\sin\tilde\phi}\left(\mathbf e_1^\top\left(\left(\boldsymbol\omega^b-\boldsymbol\omega^b_{\mathrm{ref}}\right)\times\mathbf x^b_{\mathrm{ref}}\right)-\tilde{\boldsymbol\omega}^{b\top}\mathbf J_2\mathbf H^\top\mathbf J^{-1}\mathbf H\mathbf H^\top\left(\mathbf x^b_{\mathrm{ref}}\times\mathbf e_1\right)\right)\\ &+\tilde{\boldsymbol\omega}^{b\top}\mathbf J_2\mathbf H^\top\Big[\mathbf J^{-1}\left(\mathbf I_3-\mathbf H\mathbf H^\top\right)\mathbf f\\ &+\mathbf J^{-1}\underbrace{\mathbf H\mathbf H^\top\mathbf J}_{=\mathbf J\mathbf H\mathbf H^\top}\tilde{\mathbf R}\mathbf R_i^b\left(\mathbf x^i_{\mathrm{ref}}\times\ddot{\mathbf x}^i_{\mathrm{ref}}\right)-\tilde{\mathbf R}\mathbf R_i^b\left(\mathbf x^i_{\mathrm{ref}}\times\ddot{\mathbf x}^i_{\mathrm{ref}}\right)\Big]\end{aligned}\tag{B.12}$$

Manipulation of the first of the last three terms gives

$$\begin{aligned}&\tilde{\boldsymbol\omega}^{b\top}\mathbf J_2\mathbf H^\top\mathbf J^{-1}\left(\mathbf I_3-\mathbf H\mathbf H^\top\right)\mathbf f=\tilde{\boldsymbol\omega}^{b\top}\mathbf H^\top\mathbf J\mathbf H\mathbf H^\top\mathbf J^{-1}\left(\mathbf I_3-\mathbf H\mathbf H^\top\right)\mathbf f\\ &=\tilde{\boldsymbol\omega}^{b\top}\mathbf H^\top\mathbf H\mathbf H^\top\left(\mathbf I_3-\mathbf H\mathbf H^\top\right)\mathbf f=\tilde{\boldsymbol\omega}^{b\top}\mathbf H^\top\mathbf H\left(\mathbf H^\top-\underbrace{\mathbf H^\top\mathbf H}_{=\mathbf I_2}\mathbf H^\top\right)\mathbf f=0\end{aligned}\tag{B.13}$$

The vector $\mathbf R_i^b\left(\mathbf x^i_{\mathrm{ref}}\times\ddot{\mathbf x}^i_{\mathrm{ref}}\right)$ (appearing in (B.12)) is perpendicular to $\mathbf x^b_{\mathrm{ref}}$. After rotation by $\tilde{\mathbf R}$ it becomes perpendicular to $\mathbf e_1$. Then due to the property in (B.2), $\mathbf H\mathbf H^\top\tilde{\mathbf R}\mathbf R_i^b\left(\mathbf x^i_{\mathrm{ref}}\times\ddot{\mathbf x}^i_{\mathrm{ref}}\right)=\tilde{\mathbf R}\mathbf R_i^b\left(\mathbf x^i_{\mathrm{ref}}\times\ddot{\mathbf x}^i_{\mathrm{ref}}\right)$, and the last two terms of (B.11) cancel each other.

(B.11) then simplifies to

$$\begin{aligned}\dot V = &-k_D\|\tilde{\boldsymbol\omega}^b\|^2\\ &+k_P\frac{\tilde\phi}{\sin\tilde\phi}\left(\mathbf e_1^\top\left(\left(\boldsymbol\omega^b-\boldsymbol\omega^b_{\mathrm{ref}}\right)\times\mathbf x^b_{\mathrm{ref}}\right)-\left(\boldsymbol\omega^b-\tilde{\mathbf R}\boldsymbol\omega^b_{\mathrm{ref}}\right)^\top\mathbf H\mathbf H^\top\left(\mathbf x^b_{\mathrm{ref}}\times\mathbf e_1\right)\right)\\ = &-k_D\|\tilde{\boldsymbol\omega}^b\|^2+k_P\frac{\tilde\phi}{\sin\tilde\phi}\Big(\mathbf e_1^\top\left(\left(\boldsymbol\omega^b-\boldsymbol\omega^b_{\mathrm{ref}}\right)\times\mathbf x^b_{\mathrm{ref}}\right)\\ &-{\boldsymbol\omega^b}^\top\left(\mathbf x^b_{\mathrm{ref}}\times\mathbf e_1\right)+{\boldsymbol\omega^b_{\mathrm{ref}}}^\top\tilde{\mathbf R}^\top\left(\mathbf x^b_{\mathrm{ref}}\times\mathbf e_1\right)\Big)\end{aligned}\tag{B.14}$$

Since $\tilde{\mathbf R}$ and hence also $\tilde{\mathbf R}^\top$ is a rotation about the axis parallel to $\mathbf x^b_{\mathrm{ref}}\times\mathbf e_1$, the vector $\mathbf x^b_{\mathrm{ref}}\times\mathbf e_1$ is invariant under rotation by $\tilde{\mathbf R}^\top$. This property was also exploited in [7]. This gives

$$\begin{aligned}\dot{V} =& -k_D\|\tilde{\boldsymbol{\omega}}^b\|^2 \\ &+ k_P\frac{\tilde{\phi}}{\sin\tilde{\phi}}\left(\mathbf{e}_1^\top\left(\left(\boldsymbol{\omega}^b-\boldsymbol{\omega}^b_{\text{ref}}\right)\times\mathbf{x}^b_{\text{ref}}\right)-\left(\boldsymbol{\omega}^b-\boldsymbol{\omega}^b_{\text{ref}}\right)^\top\left(\mathbf{x}^b_{\text{ref}}\times\mathbf{e}_1\right)\right) \\ =& -k_D\|\tilde{\boldsymbol{\omega}}^b\|^2 \quad \le 0\end{aligned} \tag{B.15}$$

where it has been used that $\mathbf{a}\cdot(\mathbf{b}\times\mathbf{c})=\mathbf{b}\cdot(\mathbf{c}\times\mathbf{a})$.

$\dot{V}$ can remain 0 if and only if $\tilde{\boldsymbol{\omega}}^b\equiv 0\Rightarrow\dot{\boldsymbol{\omega}}^b_e=0$. Following the same steps as when finding $\dot{V}$ eventually gives

$$\begin{aligned}\dot{\boldsymbol{\omega}}^b_e =& \mathbf{H}^\top\Big(\mathbf{J}^{-1}\left(\mathbf{f}+\mathbf{H}\mathbf{u}\right) \\ &-\tilde{\mathbf{R}}\left(\left(\boldsymbol{\omega}^b-\boldsymbol{\omega}^b_{\text{ref}}\right)\times\boldsymbol{\omega}^b_{\text{ref}}\right)-\tilde{\mathbf{R}}\left(-\boldsymbol{\omega}^b\times\boldsymbol{\omega}^b_{\text{ref}}+\mathbf{R}^b_i\left(\mathbf{x}^i_{\text{ref}}\times\ddot{\mathbf{x}}^i_{\text{ref}}\right)\right)\Big) \\ =& -k_D\mathbf{J}_2^{-1}\tilde{\boldsymbol{\omega}}^b-k_P\mathbf{J}_2^{-1}\mathbf{H}^\top\left(\frac{\tilde{\phi}}{\sin\tilde{\phi}}\left(\mathbf{x}^b_{\text{ref}}\times\mathbf{e}_1\right)\right) \\ =& -k_P\mathbf{J}_2^{-1}\mathbf{H}^\top\left(\frac{\tilde{\phi}}{\sin\tilde{\phi}}\left(\mathbf{x}^b_{\text{ref}}\times\mathbf{e}_1\right)\right)\end{aligned} \tag{B.16}$$

when $\tilde{\boldsymbol{\omega}}^b=\mathbf{0}$. Since $\mathbf{x}^b_{\text{ref}}\times\mathbf{e}_1\perp\mathbf{e}_1$, it will not disappear under multiplication with $\mathbf{H}^\top$. Hence $\dot{\boldsymbol{\omega}}^b_e=0$ requires $\frac{\tilde{\phi}}{\sin\tilde{\phi}}\left(\mathbf{x}^b_{\text{ref}}\times\mathbf{e}_1\right)=0$, which happens when $\mathbf{x}^b_{\text{ref}}\parallel\mathbf{e}_1$, i.e. when $\tilde{\phi}=0\vee\pi$, where the latter is outside the domain D.

Remark. The term $\frac{\tilde{\phi}}{\sin\tilde{\phi}}\left(\mathbf{x}^b_{\text{ref}}\times\mathbf{e}_1\right)$ in $\dot{\boldsymbol{\omega}}^b_e$ comes from the control input $\mathbf{u}$, and is by design 0 when $\tilde{\phi}=0\vee\pi$, as stated in Remark 3.

At $\tilde{\phi}=0$, the matrix $\tilde{\mathbf{R}}$ is equal to the identity matrix, and the velocity error $\tilde{\boldsymbol{\omega}}^b$ is equal to the last two elements of the velocity of $\mathbf{x}^b_{\text{ref}}$ relative to $\mathbf{e}_1$. Then $\tilde{\boldsymbol{\omega}}^b=0$ means the only angular velocity they can have relative to each other is about the axis $\mathbf{e}_1$ of the body frame. Since $\mathbf{x}^b_{\text{ref}}$ is aligned with $\mathbf{e}_1$ when $\tilde{\phi}=0$, rotation about this axis does not change the angle $\tilde{\phi}$ between the two. Hence the origin is the only invariant subset of the set $\{\tilde{\phi},\boldsymbol{\omega}^b_e\in D\,|\,\dot{V}=0\}$.

The by Corollary A.1, the origin is asymptotically stable, which gives asymptotic tracking of the reference $\mathbf{x}^i_{\text{ref}}$ by the system (3.1), (3.3).

Region of attraction

The requirement (3.10) on the initial conditions describes the open region

$$\frac{k_P\pi^2}{2} > \frac{k_P}{2}\tilde{\phi}^2 + \frac{1}{2}\tilde{\boldsymbol{\omega}}^{b\top}\mathbf{J}_2\tilde{\boldsymbol{\omega}}^b \tag{B.17}$$

Let the region (B.17) be denoted $\Omega_{\max}$. Since $\dot{V} \leq 0 \Rightarrow V \leq V(0)\,\forall t \geq 0$, for all trajectories starting in $\Omega_{\max}$ it holds that

$$\frac{k_P}{2}\tilde{\phi}^2 + \frac{1}{2}\tilde{\boldsymbol{\omega}}^{b\top}\mathbf{J}_2\tilde{\boldsymbol{\omega}}^b \leq \frac{k_P}{2}\tilde{\phi}(0)^2 + \frac{1}{2}\tilde{\boldsymbol{\omega}}^b(0)^\top\mathbf{J}_2\tilde{\boldsymbol{\omega}}^b(0) < \frac{k_P\pi^2}{2} \tag{B.18}$$

meaning that the set $\Omega_{\max}$ is positively invariant. Furthermore,

$$\begin{aligned}\tilde{\phi}(t)^2 &\leq \frac{2}{k_P}V(t) \leq \frac{2}{k_P}V(0)\\ &\leq \tilde{\phi}(0)^2 + \frac{1}{k_P}\tilde{\boldsymbol{\omega}}^b(0)^\top\mathbf{J}_2\tilde{\boldsymbol{\omega}}^b < \tilde{\phi}(0)^2 + \pi^2 - \tilde{\phi}(0)^2 = \pi^2\\ &\Rightarrow \tilde{\phi}(t) < \pi\,\forall t\end{aligned} \tag{B.19}$$

This means that $\Omega_{\max}$ lies entirely in D.

For any initial condition $(\tilde{\phi}(0), \tilde{\boldsymbol{\omega}}^b(0)) \in \Omega_{\max}$, let $c = V(\tilde{\phi}(0), \tilde{\boldsymbol{\omega}}^b(0))$. Since V is quadratic, the closed set $\Omega_c = \{\tilde{\phi}, \boldsymbol{\omega}_e^b \in D \,|\, V(\tilde{\phi}, \boldsymbol{\omega}_e^b) \leq c\}$ is bounded. Among the points in Ω_c such that $\dot{V} = 0$, the largest invariant set is the origin, $\{(0, \mathbf{0})\}$.

Hence by LaSalle's invariance theorem (Theorem A.1) every trajectory starting in Ω_c approaches the origin. Since a c can be found for every point in $\Omega_{\max}$, every trajectory starting in $\Omega_{\max}$ approaches the origin.

The system (3.1), (3.3) converges to its reference from any initial conditions described by (3.10).

Appendix C

Simulation Model Parameters

The physical parameters of the links of the USM model used in the simulations in Chapter 6 are given in Table C.1, and the position of its thrusters in Table C.2.

All the links are neutrally buoyant.

Table C.1: USM link dimensions and masses

Link	1	3	5	7	9	2, 4, 6, 8
Mass [kg]	14.3	12.7	9.8	12.7	7.8	6.0
Length [m]	0.62	0.584	0.726	0.584	0.37	0.104
Radius [m]	0.085	0.085	0.085	0.085	0.085	0.085

Table C.2: Thruster positions and thrust directions, given in the link frame of the link to which they are attached. The thrust direction is denoted $\boldsymbol{\beta}_{t,i}$, and the position $\mathbf{r}_{t,i}$

Thruster	1	2	3	4	5	6	7
Link	3	3	5	5	5	7	7
$\boldsymbol{\beta}_{t,i}$	$\mathbf{e}_3$	$\mathbf{e}_2$	$\mathbf{e}_1$	$\mathbf{e}_1$	$\mathbf{e}_3$	$\mathbf{e}_2$	$\mathbf{e}_3$
$\mathbf{r}_{t,i}$	0.237	0.347	0.278	0.278	0.488	0.237	0.347
	0	0	-0.1	0.1	0	0	0
	0	0	0	0	0	0	0

Appendix D

Implementation Overview

Figure D.1 shows an overview of the attached Simulink implementation. The model requires MATLAB release 2017b or newer.

Among the attached `.m`-files, only `find_sat.m` has been written as part of this work. The rest belongs to the model dynamics and trust allocation.

The simulation can be run through the attached file `run_3D_simulation.m`. This will run a simulation, show a 3D visualisation, then plot a set of states. The correct path to the folder with the code must first be set in `initializePath.m`.

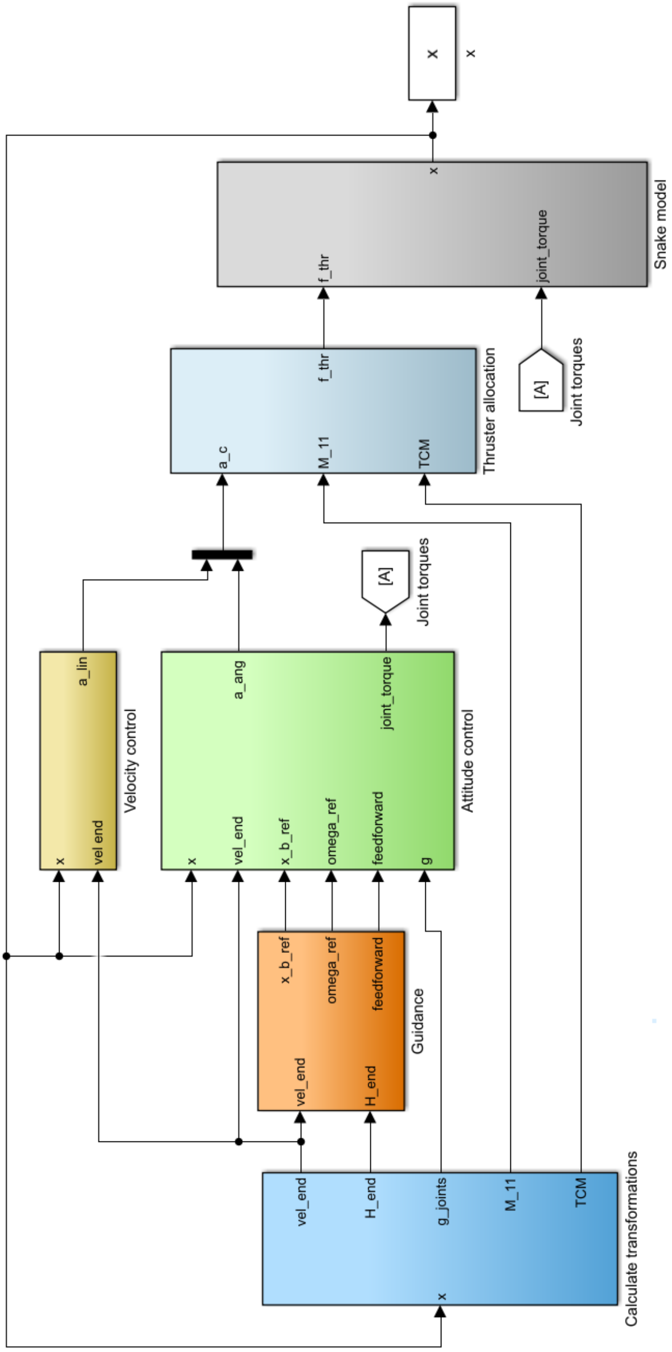

Figure D.1: Overview of the Simulink diagram

Appendix E

Additional simulation results

In this appendix, additional simulation results using the USM model with too large inertia and hydrostatic forces are presented. The links have the same length and radius as given in Appendix C, but the mass used to compute rigid body mass and hydrostatic forces is ten times larger. The USM is still neutrally buoyant, as buoyancy is computed using link volumes ten times larger.

The result is a robot subject to very large inertia and hydrostatic forces relative to the hydrodynamic effects, which are computed for the correct dimensions.

Control parameters

The simulations in this appendix all use the guidance and control parameters as given in Tables E.1 and E.2. The direction of gravity is downwards along the inertial z-axis, making the path along the inertial x-axis horizontal.

Table E.1: Parameters for guidance, direction control and joint control

u_d	k_e	k_P	k_D	$k_{\theta,P}$	$k_{\theta,D}$
0.5	$\frac{u_d}{20}$	2	10	100	200

Table E.2: Control parameters of the thruster controllers; the PI-controller for surge, and thrust allocation using all thrusters, or longitudinal only

	PI-controller	Thrust allocation
$\mathbf{K}_{\text{lin},P}/k_{u,P}$	500	diag(0.2, 0.2, 0.2)
$k_{u,I}$	5	0.01
$k_{\text{ang},P}$	-	0.2
$k_{\text{ang},D}$	-	2

E.1 Comparison of body curvatures

Simulation results of path-following using the three proposed shapes, as well as several different values of the parameter α for the exponential curvature are shown in Figures E.1-E.6. The surge of the end-effector is controlled using the basic PI-controller (5.16).

Figures E.1-E.4 show the results of using exponential curvature with different values of α, and for two initial conditions. In both cases, the initial position of the base is $[0,\ 10,\ -5]^\top$. In Figures E.1 and E.2, the USM starts pointing parallel to the path. In Figures E.3 and E.4, the initial position of the base is the same, but the USM starts pointing away from the path, increasing not only the angle between current and desired pointing direction, but also the initial cross-track error measured from end-effector.

Simulation results using the linear and uniform curvature are then shown in Figures E.5 and E.6, together with two selected versions of the exponential curvature for reference. Finally, more details from the simulations using the uniform and linear curvatures are shown in Figures E.7 and E.8.

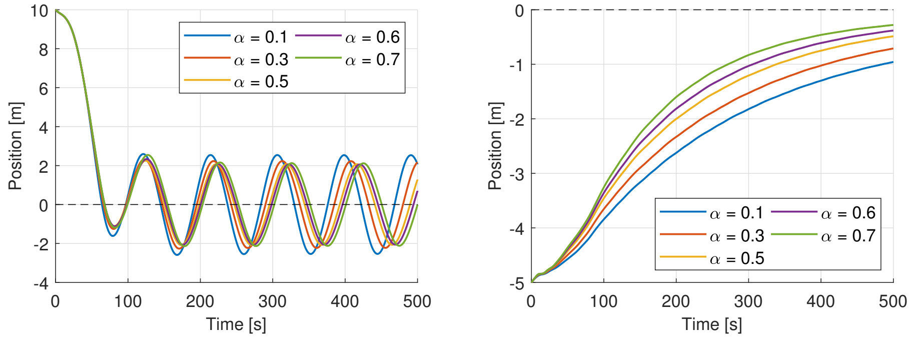

(a) Cross-track error along y-axis (b) Cross-track error along z-axis

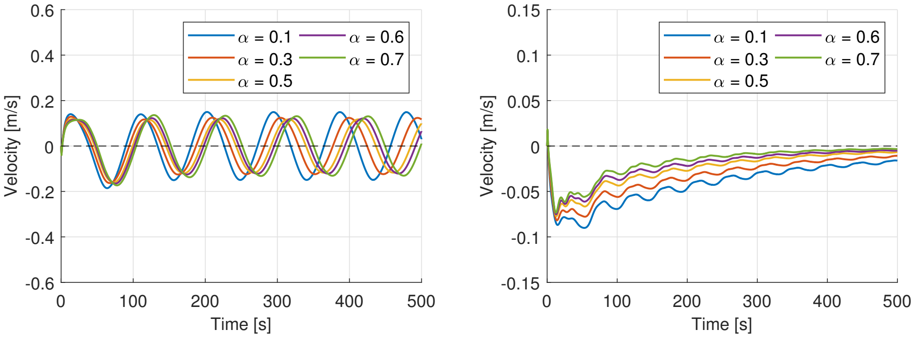

(c) End-effector sway velocity (d) End-effector heave velocity

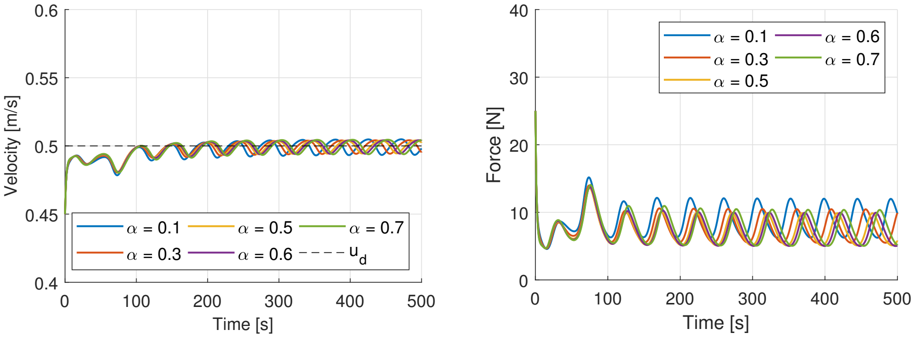

(e) End-effector surge velocity (f) Thruster force

Figure E.1: Simulation results of path-following with varying exponential body curvature, with the USM starting pointing parallel to the path.

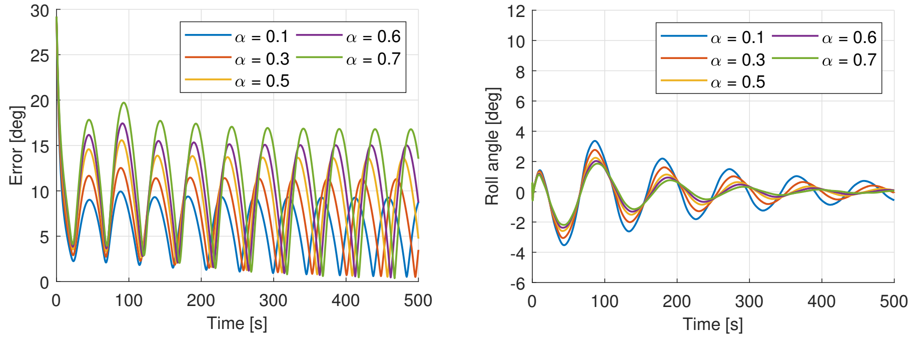

(a) Total error angle $\tilde{\phi}$

(b) Roll of end-effector frame

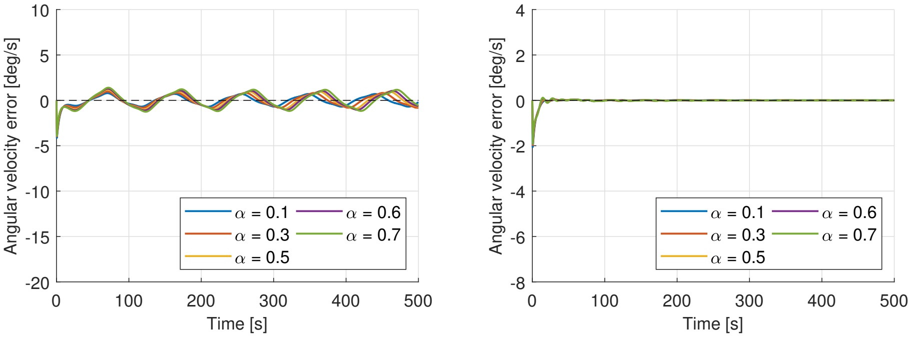

(c) $\tilde{\boldsymbol{\omega}}^e$ about z-axis

(d) $\tilde{\boldsymbol{\omega}}^e$ about y-axis

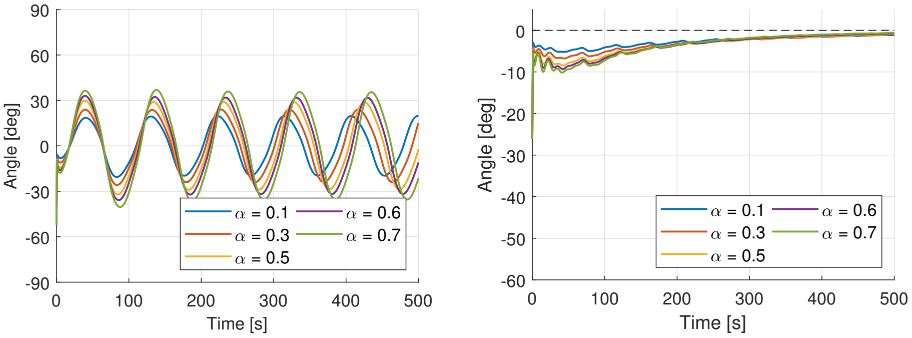

(e) Base angle $\theta_{z,0}$

(f) Base angle $\theta_{y,0}$

Figure E.2: Simulation results of path-following with varying exponential body curvature, with the USM starting pointing parallel to the path, continued.

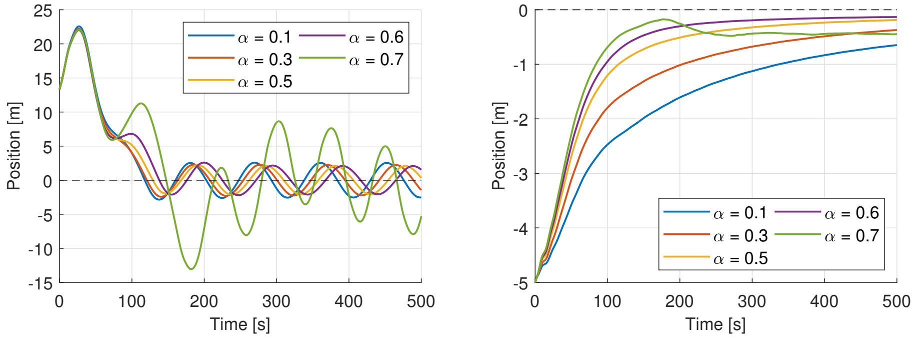

(a) Cross-track error along y-axis (b) Cross-track error along z-axis

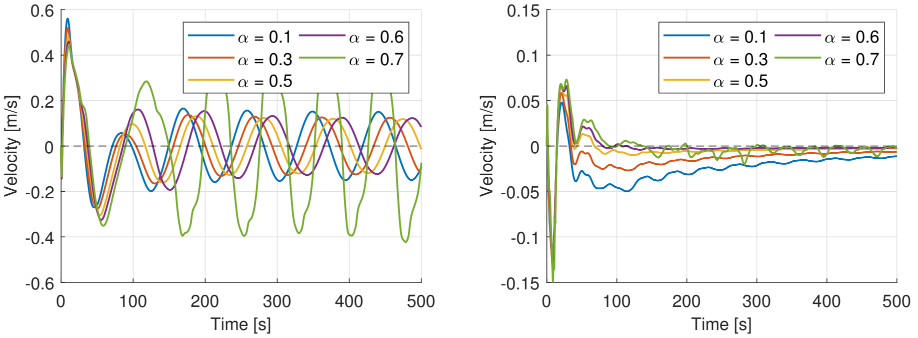

(c) End-effector sway velocity (d) End-effector heave velocity

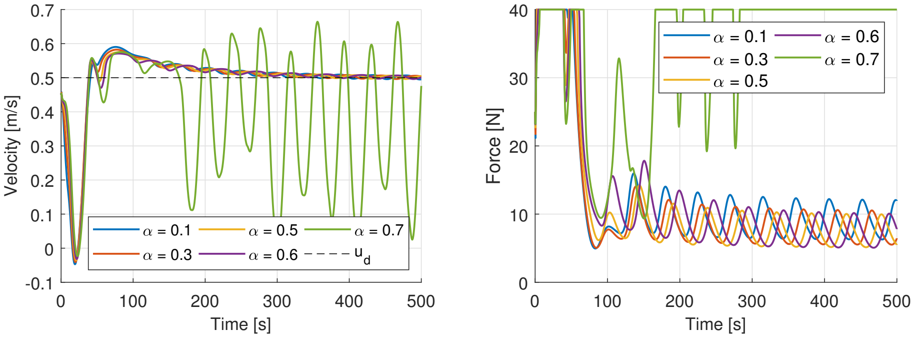

(e) End-effector surge velocity (f) Thruster force

Figure E.3: Simulation results of path-following with varying exponential body curvature, with the USM starting pointing away from the path.

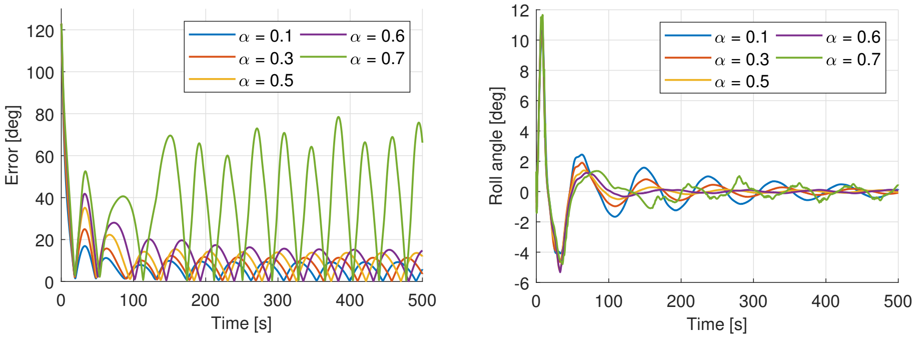

(a) Total error angle $\tilde{\phi}$ (b) Roll of end-effector frame

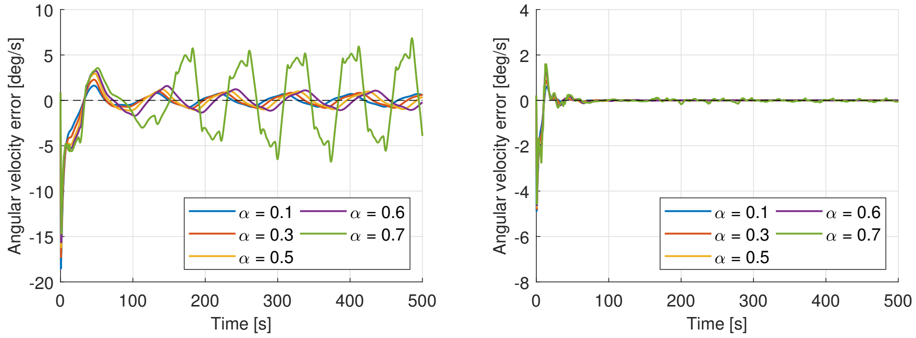

(c) $\tilde{\boldsymbol{\omega}}^e$ about z-axis (d) $\tilde{\boldsymbol{\omega}}^e$ about y-axis

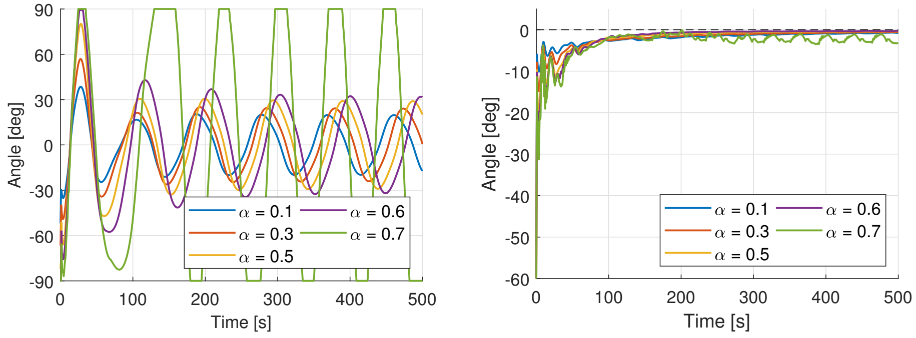

(e) Base angle $\theta_{z,0}$ (f) Base angle $\theta_{y,0}$

Figure E.4: Simulation results of path-following with varying exponential body curvature, with the USM starting pointing away from the path, continued.

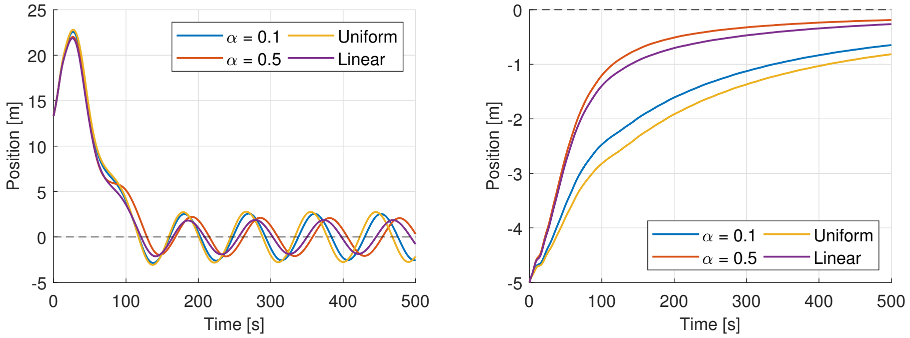

(a) Cross-track error along y-axis (b) Cross-track error along z-axis

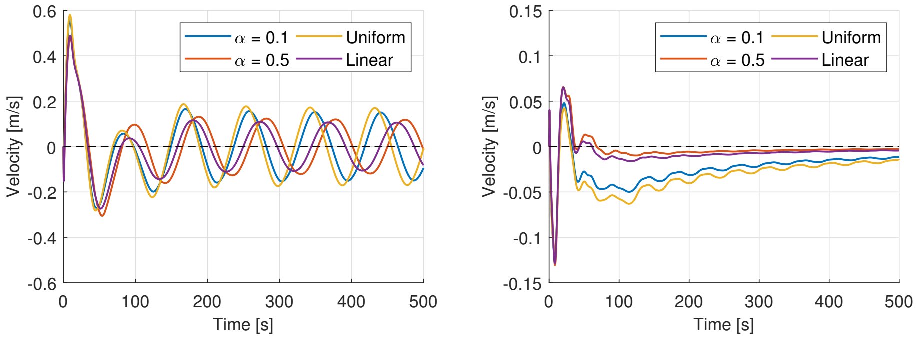

(c) End-effector sway velocity (d) End-effector heave velocity

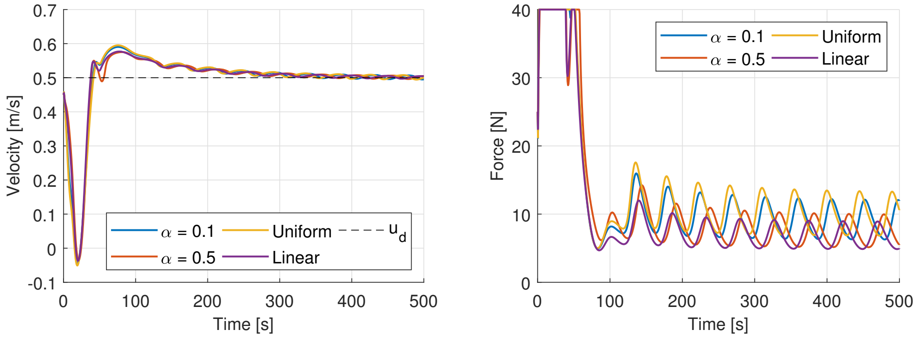

(e) End-effector surge velocity (f) Thruster force

Figure E.5: Simulation results of path-following with uniform, linear and exponential body curvature.

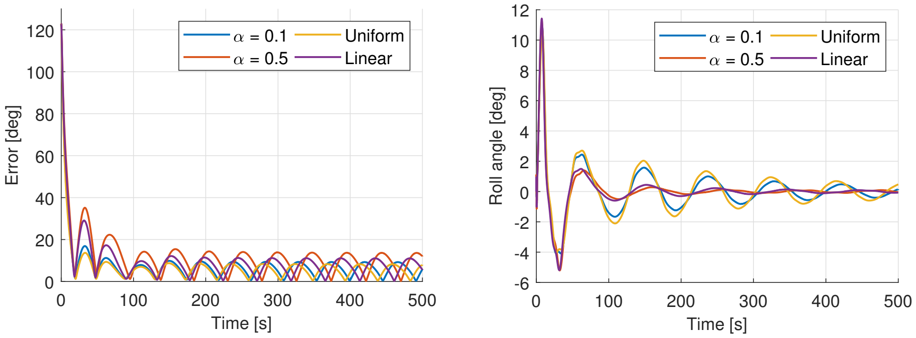

(a) Total error angle $\tilde{\phi}$ (b) End-effector frame roll

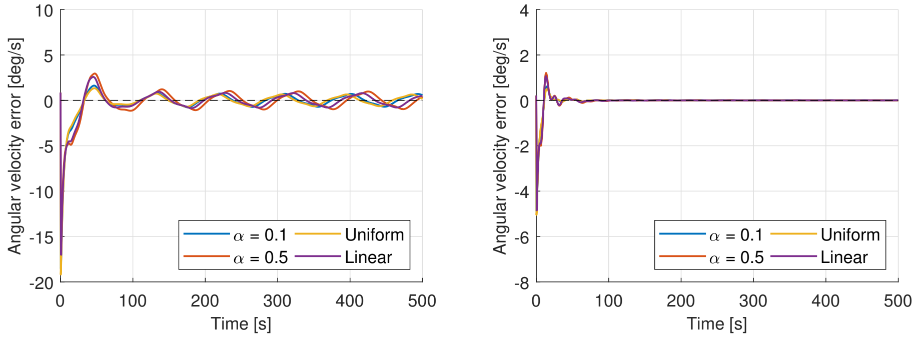

(c) $\tilde{\boldsymbol{\omega}}^e$ about z-axis (d) $\tilde{\boldsymbol{\omega}}^e$ about y-axis

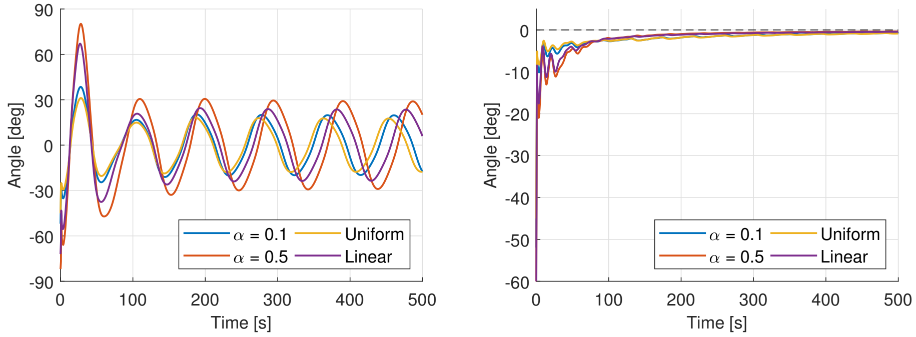

(e) Base angle $\theta_{z,0}$ (f) Base angle $\theta_{y,0}$

Figure E.6: Simulation results of path-following with uniform, linear and exponential body curvature, continued.

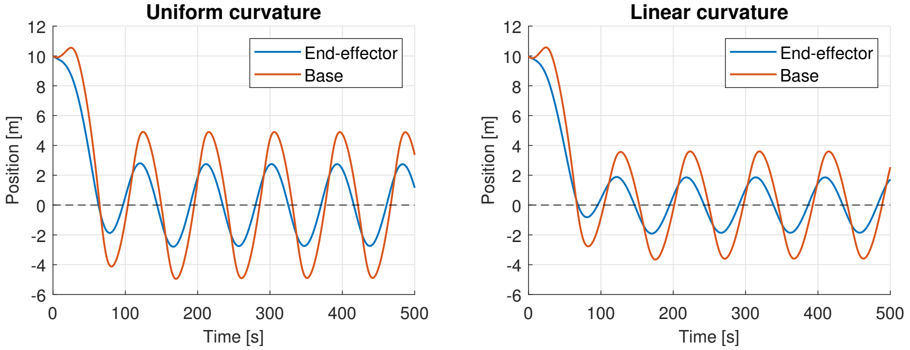

(a) Cross-track error along y-axis

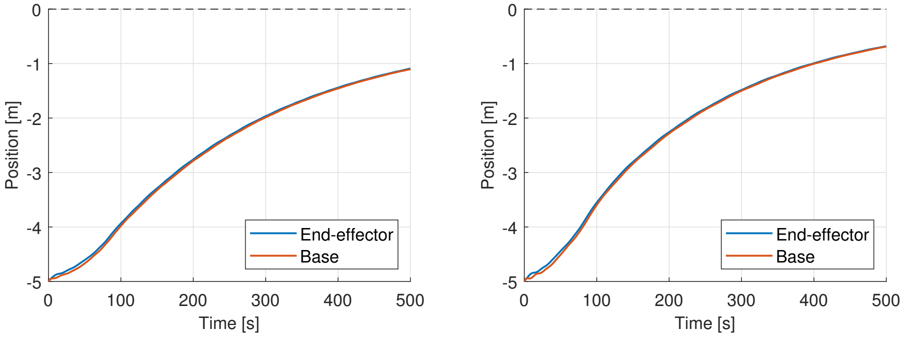

(b) Cross-track error along z-axis

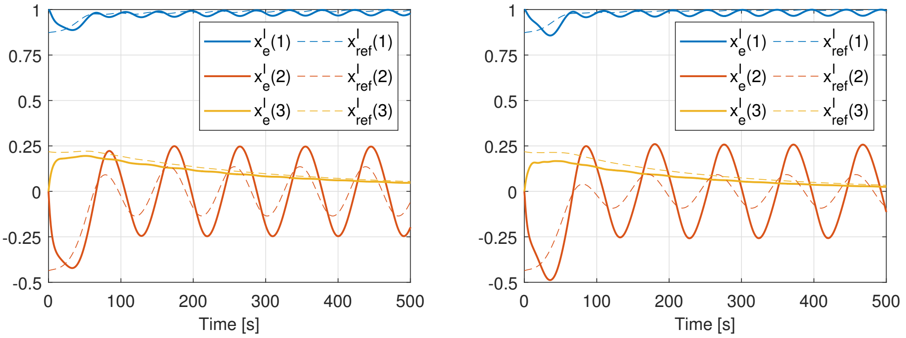

(c) Inertial-frame representation of the end-effector pointing direction

Figure E.7: Simulation results of path-following with uniform and linear body curvature. End-effector and base positions, and end-effector pointing direction.

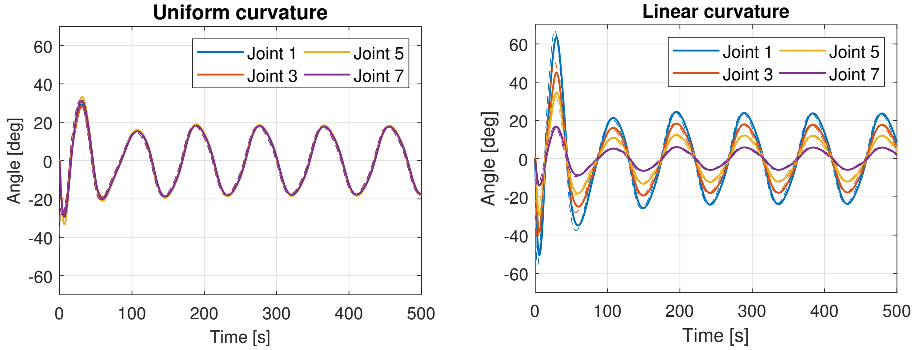

(a) Joint angles of joints rotating about z-axis, references in dashed lines

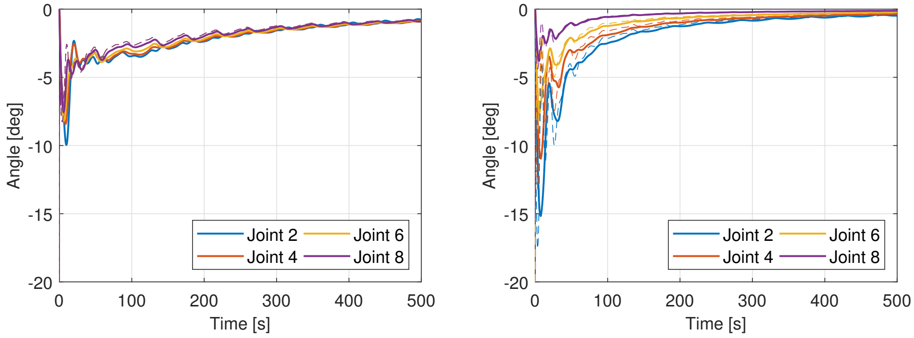

(b) Joint angles of joints rotating about y-axis, references in dashed lines

Figure E.8: Simulation results of path-following with uniform and linear body curvature, joint angles.

E.2 Hydrostatic compensation and torque saturation in joint control

This section presents simulation results with and without compensation for hydrostatic restoring moments in the joint controller (5.15), and with and without saturation of the control torques. The torques are saturated at 11 Nm, as for the correct USM model. The four possible combinations make up the joint control modes as summarised in Table 6.4.

Figures E.9-E.11 show simulation results of path-following using the four modes of joint control. The linear curvature is used, and the surge of the end-effector is controlled using the PI-controller (5.16). The USM starts pointing parallel to the path.

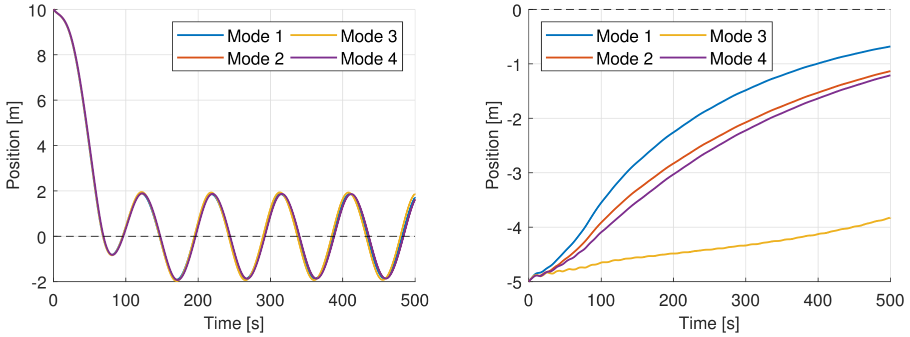

(a) Cross-track error of the end-effector along the y-axis

(b) Cross-track error of the end-effector along the z-axis

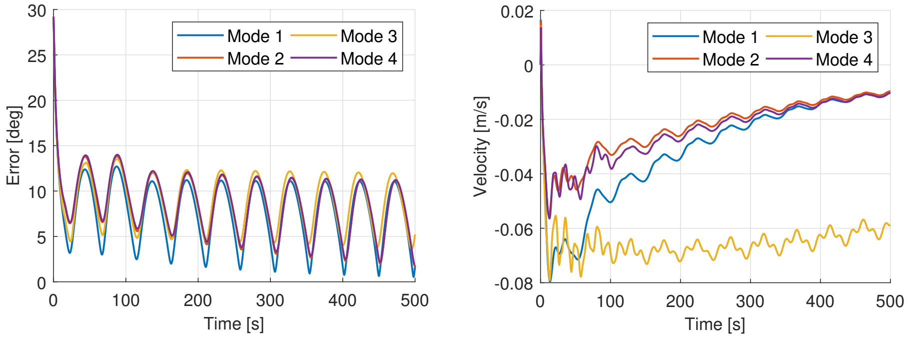

(c) Total pointing direction error angle $\tilde{\phi}$

(d) Heave velocity

Figure E.9: Simulation results of path-following with and without hydrostatic compensation in joints and saturation of joint torques.

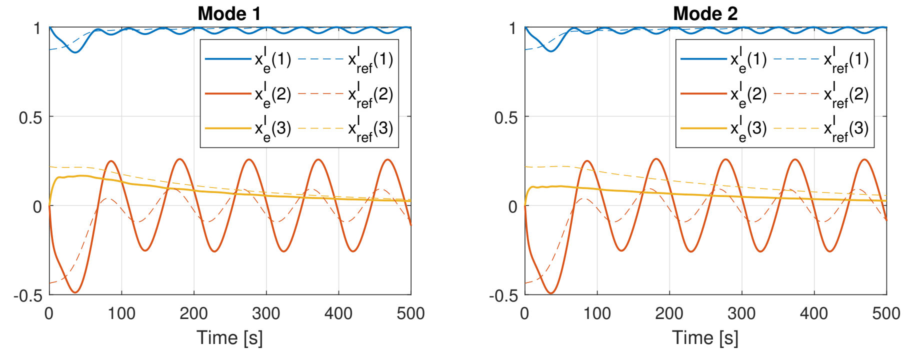

(a) End-effector pointing direction in the inertial frame

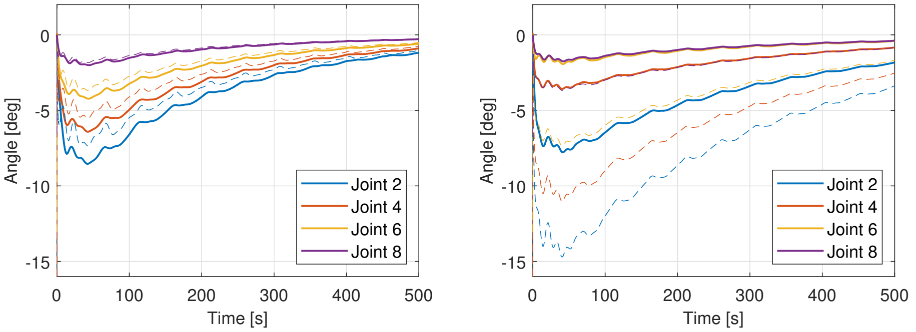

(b) Joint angles of joints rotating about y-axis, references in dashed lines

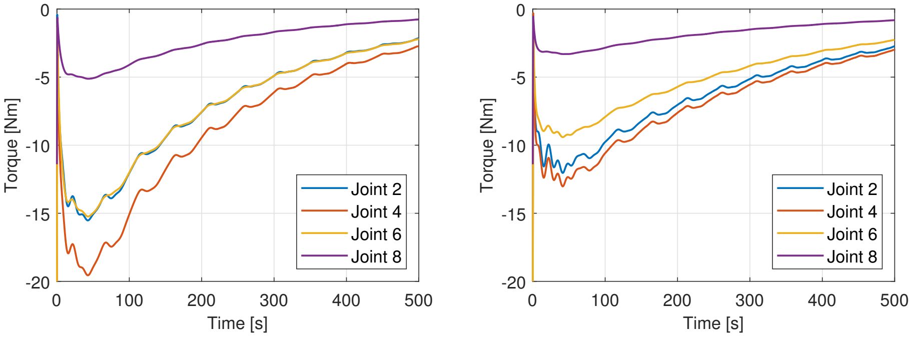

(c) Joint torques of joints rotating about y-axis

Figure E.10: Simulation results of path-following with and without hydrostatic compensation, without saturation of torques.

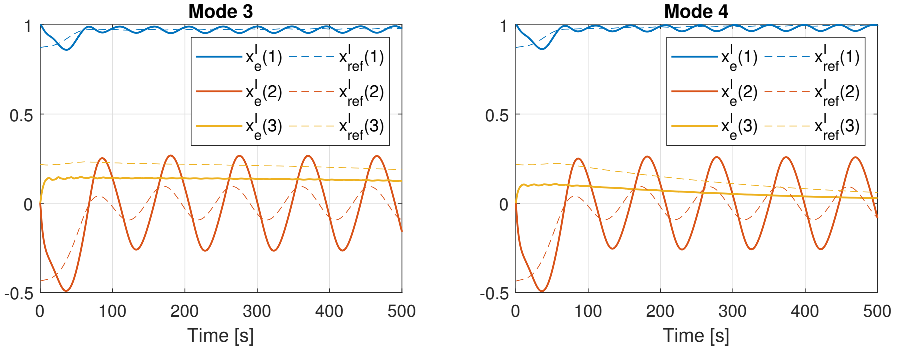

(a) End-effector pointing direction in the inertial frame

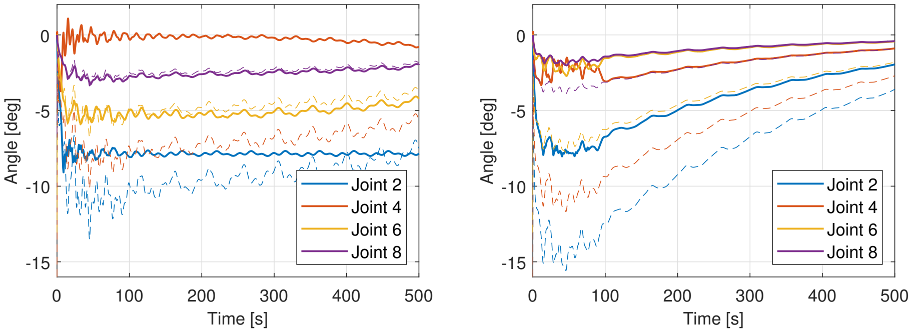

(b) Joint angles of joints rotating about the y-axis, references in dashed lines

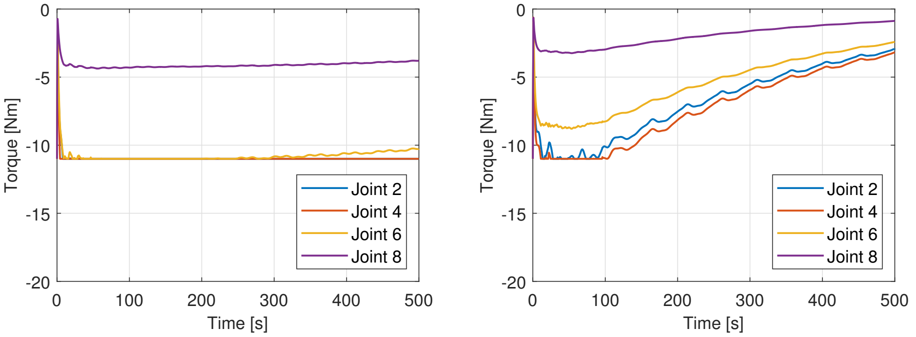

(c) Joint torques of joints rotating about the y-axis

Figure E.11: Simulation results of path-following with saturation of joint torques, with and without hydrostatic moment compensation.

E.3 Thruster modes

Figures E.12-E.15 show the results of using thrust allocation among all available thrusters to help stabilise velocity and attitude. Out of the combinations listed in Table 6.5, only combinations 1, 3 and 4 are shown, as combination 2 gave even worse performance than combination 1.

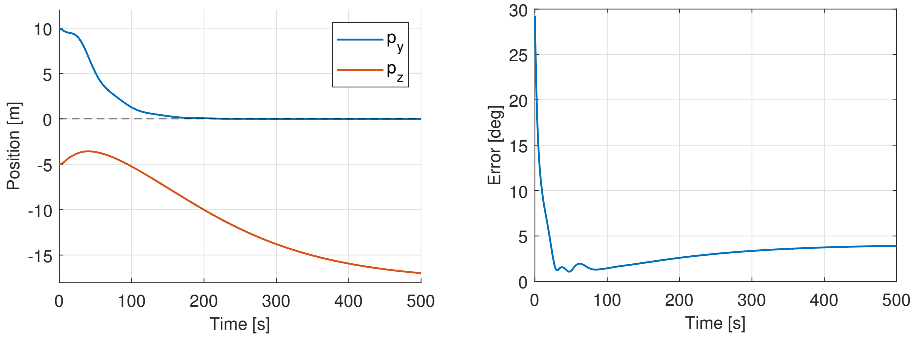

(a) End-effector position (b) Total error angle $\tilde{\phi}$

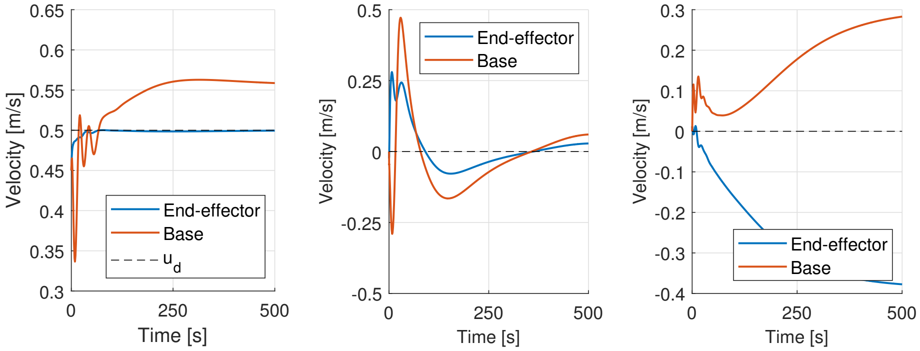

(c) Surge velocity (d) Sway velocity (e) Heave velocity

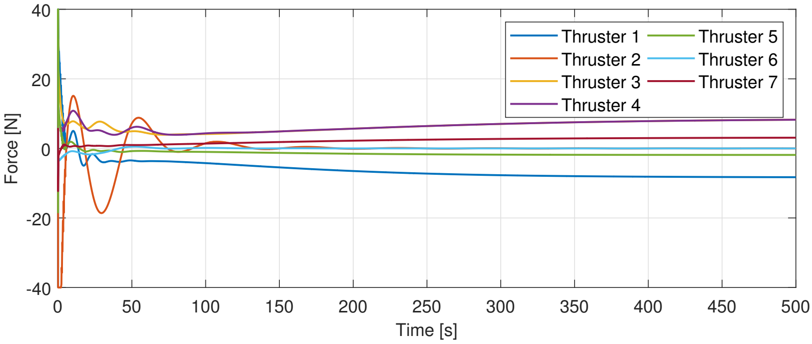

(f) Thruster forces

Figure E.12: Simulation results using thrust allocation combination 1.

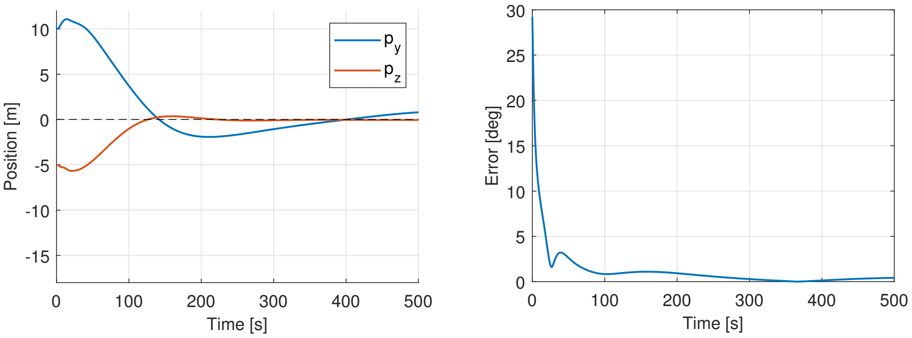

(a) End-effector position (b) Total error angle $\tilde{\phi}$

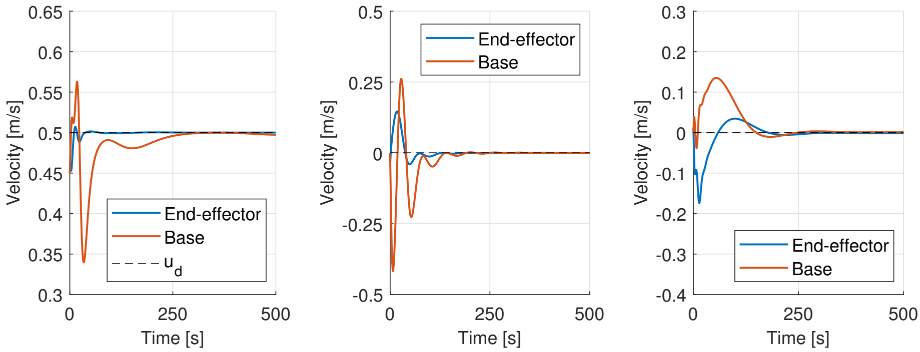

(c) Surge velocity (d) Sway velocity (e) Heave velocity

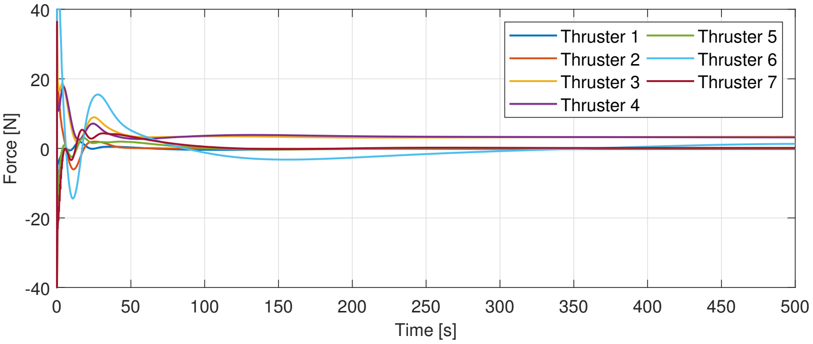

(f) Thruster forces

Figure E.13: Simulation results using thrust allocation combination 3.

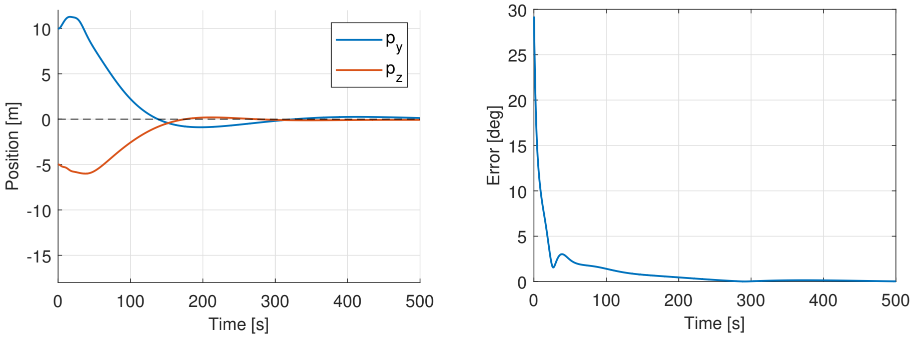

(a) End-effector position (b) Total error angle $\tilde{\phi}$

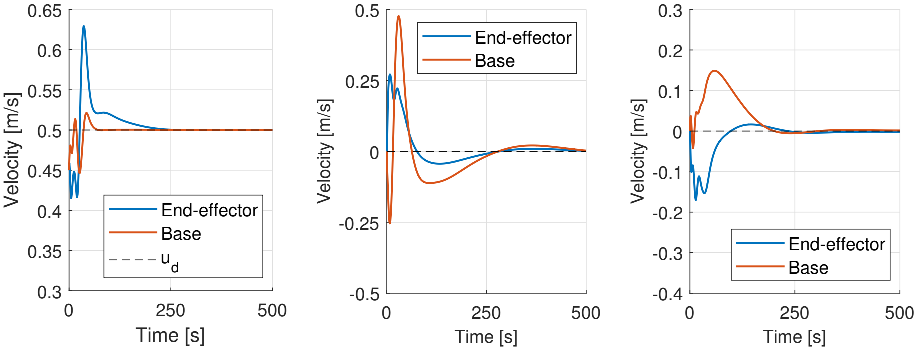

(c) Surge velocity (d) Sway velocity (e) Heave velocity

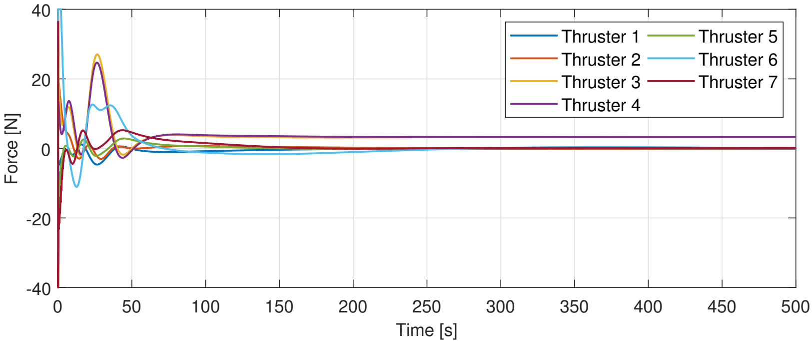

(f) Thruster forces

Figure E.14: Simulation results using thrust allocation combination 4.

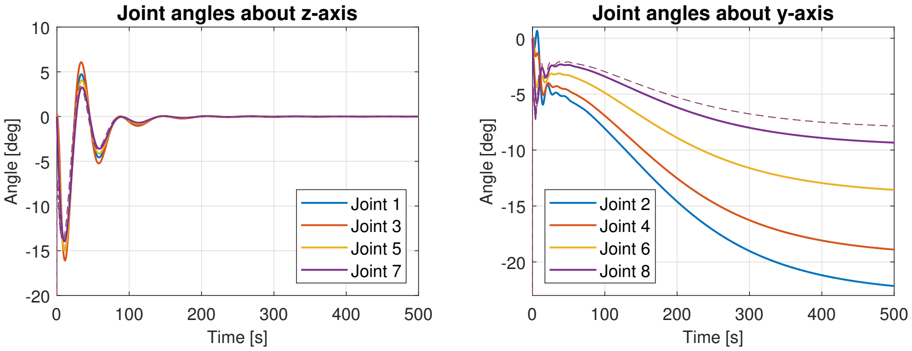

(a) Combination 1

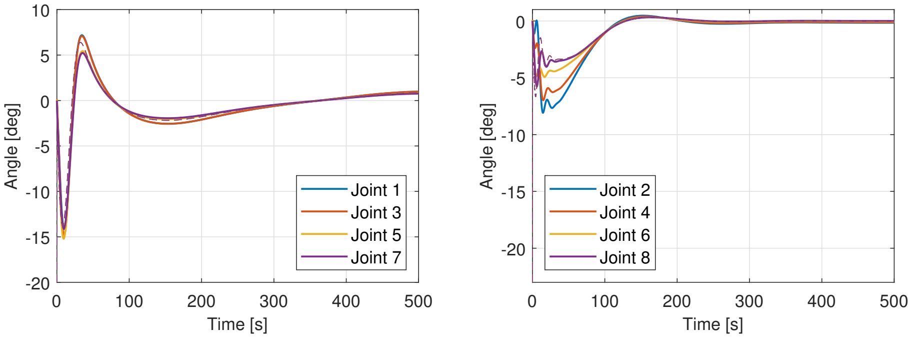

(b) Combination 3

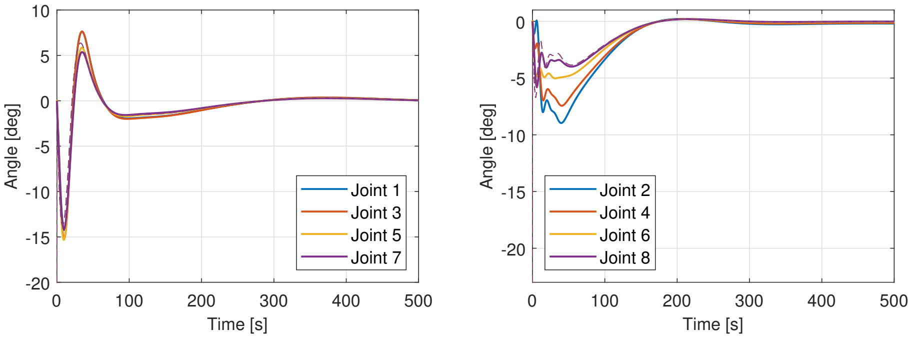

(c) Combination 4

Figure E.15: Joint angles when using all available thrusters.

References

[1] M. F. Amundsen, “Control of an underwater swimming manipulator, with compensation for reaction forces and hydrostatic forces,” Master’s thesis, Norwegian University of Science and Technology, June 2017.

[2] D. S. Bernstein, *Matrix Mathematics: Theory, Facts, and Formulas*, 2nd ed. Princeton University Press, 2009.

[3] S. P. Bhat and D. S. Bernstein, “A topological obstruction to continuous global stabilization of rotational motion and the unwinding phenomenon,” *Systems & Control Letters*, vol. 39, no. 1, pp. 63 – 70, 2000.

[4] I.-L. G. Borlaug, “Higher-order sliding mode control - stability analysis and application to underwater snake robots,” Master’s thesis, Norwegian University of Science and Technology, June 2017.

[5] M. Breivik and T. I. Fossen, “Guidance-based path following for autonomous underwater vehicles,” in *Proceedings of OCEANS 2005 MTS/IEEE*, Sept 2005, pp. 2807–2814.

[6] F. Bullo, R. Murray, and A. Sarti, “Control on the sphere and reduced attitude stabilization,” *IFAC Proceedings Volumes*, vol. 28, no. 14, pp. 495 – 501, 1995, 3rd IFAC Symposium on Nonlinear Control Systems Design.

[7] ——, “Control on the sphere and reduced attitude stabilization,” California Institute of Technology, Tech. Rep., 1995, available at http://resolver.caltech.edu/CaltechCDSTR:1995.CIT-CDS-95-005.

[8] E. Børhaug, A. Pavlov, and K. Y. Pettersen, “Integral LOS control for path following of underactuated marine surface vessels in the presence of constant

ocean currents," in *Proc. 47th IEEE Conference on Decision and Control*, December 2008, pp. 4984–4991.

[9] E. Børhaug and K. Y. Pettersen, "LOS path following for underactuated underwater vehicle," in *Proc. 7th IFAC Conference on Manoevring and Control of Marine Craft*, Lisbon, Portugal, September 2006.

[10] W. Caharija, K. Y. Pettersen, J. T. Gravdahl, and A. J. Sørensen, "Topics on current compensation for path following applications of underactuated underwater vehicles," *IFAC Proceedings Volumes*, vol. 45, no. 5, pp. 184 – 191, 2012, 3rd IFAC Workshop on Navigation, Guidance and Control of Underwater Vehicles.

[11] N. A. Chaturvedi, A. K. Sanyal, and N. H. McClamroch, "Rigid-body attitude control," *IEEE Control Systems*, vol. 31, no. 3, pp. 30–51, June 2011.

[12] O. Egeland and J. T. Gravdahl, *Modeling and Simulation for Automatic Control*. Marine Cybernetics, 2002.

[13] T. I. Fossen, *Handbook of Marine Craft Hydrodynamics and Motion Control*. John Wiley & Sons, 2011.

[14] J. Guo, "A waypoint-tracking controller for a biomimetic autonomous underwater vehicle," *Ocean Engineering*, vol. 33, no. 17, pp. 2369 – 2380, 2006.

[15] E. Kelasidi, P. Liljeback, K. Y. Pettersen, and J. T. Gravdahl, "Innovation in underwater robots: Biologically inspired swimming snake robots," *IEEE Robotics Automation Magazine*, vol. 23, no. 1, pp. 44–62, March 2016.

[16] E. Kelasidi, P. Liljebäck, K. Y. Pettersen, and J. T. Gravdahl, "Integral line-of-sight guidance for path following control of underwater snake robots: Theory and experiments," *IEEE Transactions on Robotics*, vol. 33, no. 3, pp. 610–628, June 2017.

[17] E. Kelasidi, K. Y. Pettersen, and J. T. Gravdahl, "Modeling of underwater snake robots moving in a vertical plane in 3D," in *2014 IEEE/RSJ International Conference on Intelligent Robots and Systems*, September 2014, pp. 266–273.

[18] E. Kelasidi, K. Y. Pettersen, P. Liljebäck, and J. T. Gravdahl, "Locomotion efficiency of underwater snake robots with thrusters," in *2016 IEEE International Symposium on Safety, Security, and Rescue Robotics (SSRR)*, October 2016, pp. 174–181.

[19] E. Kelasidi, "Modeling, control and energy efficiency of underwater snake robots," Ph.D. dissertation, Norwegian University of Science and Technology, December 2015.

[20] H. K. Khalil, *Nonlinear Systems*, 3rd ed. Prentice Hall, 2002.

[21] W. Khalil, G. Gallot, and F. Boyer, "Dynamic modeling and simulation of a 3-D serial eel-like robot," *IEEE Transactions on Systems, Man, and Cybernetics, Part C (Applications and Reviews)*, vol. 37, no. 6, pp. 1259–1268, November 2007.

[22] A. M. Kohl, E. Kelasidi, A. Mohammadi, M. Maggiore, and K. Y. Pettersen, "Planar maneuvering control of underwater snake robots using virtual holonomic constraints," *Bioinspiration & Biomimetics*, vol. 11, no. 6, 2016.

[23] A. M. Kohl, "Guidance and control of underwater snake robots using planar sinusoidal gaits," Ph.D. dissertation, Norwegian University of Science and Technology, October 2017.

[24] L. Lapierre and B. Jouvencel, "Path following control for an eel-like robot," in *Europe Oceans 2005*, vol. 1, June 2005, pp. 460–465.

[25] T. Lee, "Geometric tracking control of the attitude dynamics of a rigid body on SO(3)," in *Proceedings of the 2011 American Control Conference*, June 2011, pp. 1200–1205.

[26] T. Lee, M. Leok, and N. H. McClamroch, "Geometric tracking control of a quadrotor UAV on SE(3)," in *Proc. 49th IEEE Conference on Decision and Control (CDC)*, December 2010, pp. 5420–5425.

[27] ——, "Stable manifolds of saddle equilibria for pendulum dynamics on S2 and SO(3)," in *2011 50th IEEE Conference on Decision and Control and European Control Conference*, December 2011, pp. 3915–3921.

[28] E. Lefeber, S. J. A. M. van den Eijnden, and H. Nijmeijer, "Almost global tracking control of a quadrotor UAV on SE(3)," in *Proc. IEEE 56th Annual Conference on Decision and Control (CDC)*, December 2017, pp. 1175–1180.

[29] A. M. Lekkas and T. I. Fossen, "A quaternion-based LOS guidance scheme for path following of AUVs," *IFAC Proceedings Volumes*, vol. 46, no. 33, pp. 245 – 250, 2013, 9th IFAC Conference on Control Applications in Marine Systems.

[30] J. Markdahl, J. Hoppe, L. Wang, and X. Hu, “A geodesic feedback law to decouple the full and reduced attitude,” *Systems & Control Letters*, vol. 102, pp. 32 – 41, 2017.

[31] D. Mellinger and V. Kumar, “Minimum snap trajectory generation and control for quadrotors,” in *Proc. 2011 IEEE International Conference on Robotics and Automation*, May 2011, pp. 2520–2525.

[32] S. Moe, W. Caharija, K. Y. Pettersen, and I. Schjølberg, “Path following of underactuated marine underwater vehicles in the presence of unknown ocean currents,” in *Proc. 33rd International Conference on Ocean, Offshore and Arctic Engineering*, San Francisco, USA, June 2014.

[33] C. Paliotta and K. Y. Pettersen, “Geometric path following with ocean current estimation for ASVs and AUVs,” in *2016 American Control Conference (ACC)*, July 2016, pp. 7261–7268.

[34] C. Paliotta, “Control of under-actuated marine vehicles,” Ph.D. dissertation, Norwegian University of Science and Technology, September 2017.

[35] M. Piñeirua, R. Godoy-Diana, and B. Thiria, “Resistive thrust production can be as crucial as added mass mechanisms for inertial undulatory swimmers,” *Phys. Rev. E*, vol. 92, August 2015.

[36] C. M. Pong and D. W. Miller, “Reduced-attitude boresight guidance and control on spacecraft for pointing, tracking and searching,” *Journal of Guidance, Control and Dynamics*, vol. 38, no. 6, pp. 1027–1035, 2015.

[37] M. Ramp and E. Papadopoulos, “Attitude and angular velocity tracking for a rigid body using geometric methods on the two-sphere,” in *2015 European Control Conference (ECC)*, July 2015, pp. 3238–3243.

[38] P. Ridao, M. Carreras, D. Ribas, P. J. Sanz, and G. Oliver, “Intervention AUVs: The next challenge,” *Annual Reviews in Control*, vol. 40, pp. 227 – 241, 2015.

[39] A. Sans-Muntadas, E. Kelasidi, K. Y. Pettersen, and E. Brekke, “Spiral path planning for docking of underactuated vehicles with limited FOV,” in *Proc. 1st IEEE Conference on Control Technology and Applications (CCTA)*, Kohala Coast, Hawaii, August 2017.

[40] A. Sanyal, N. Nordkvist, and M. Chyba, "An almost global tracking control scheme for maneuverable autonomous vehicles and its discretization," *IEEE Transactions on Automatic Control*, vol. 56, no. 2, pp. 457–462, February 2011.

[41] H. Schmidt-Didlaukies, K. Y. Pettersen, and A. J. Sørensen, "Modeling of articulated underwater robots for simulation and control," in *Proc. 2018 IEEE/OES Autonomous Underwater Vehicles (AUV)*, 2018, (Submitted).

[42] J. Sverdrup-Thygeson, E. Kelasidi, K. Y. Pettersen, and J. T. Gravdahl, "A control framework for biologically inspired underwater swimming manipulators equipped with thrusters," in *Proc. 10th IFAC Conference on Control Applications in Marine Systems*, September 2016.

[43] ——, "Modeling of underwater swimming manipulators," in *Proc. 10th IFAC Conference on Control Applications in Marine Systems*, September 2016.

[44] ——, "The underwater swimming manipulator - a bio-inspired AUV," in *2016 IEEE/OES Autonomous Underwater Vehicles (AUV)*, November 2016, pp. 387–395.

[45] ——, "The underwater swimming manipulator - a bioinspired solution for subsea operations," *IEEE Journal of Oceanic Engineering*, vol. 43, no. 2, pp. 402–417, April 2018.

[46] J. Sverdrup-Thygeson, S. Moe, K. Y. Pettersen, and J. T. Gravdahl, "Kinematic singularity avoidance for robot manipulators using set-based manipulability tasks," in *Proc. 1st IEEE Conference on Control Technology and Applications (CCTA)*, Kohala Coast, Hawaii, August 2017, pp. 142–149.

[47] C. A. Woolsey, "Directional control of a slender, underactuated AUV using potential shaping," in *Proc. 45th IEEE Conference on Decision and Control*, December 2006, pp. 6826–6831.

[48] J. Yuh, G. Marani, and D. R. Blidberg, "Applications of marine robotic vehicles," *Intelligent Service Robotics*, vol. 4, no. 4, pp. 221–231, July 2011.